INVESTIGATION OF THE HADRONIC AND RADIATIVE DECAYS OF NEUTRAL D-STAR MESONS PRODUCED AT THE 4.028 GEV ELECTRON-POSITRON RESONANCE

RAY FRANKLIN COWAN

A DISSERTATION
PRESENTED TO THE FACULTY
OF PRINCETON UNIVERSITY
IN CANDIDACY FOR THE DEGREE
OF DOCTOR OF PHILOSOPHY

RECOMMENDED FOR ACCEPTANCE
BY THE DEPARTMENT OF
PHYSICS

JUNE 1987

Abstract

The Crystal Ball detector at the colliding-beam ring SPEAR has been used to study the pionic and radiative decays of the neutral charm meson D^{*0} in e^+e^- annihilations at $\sqrt{s} = 4.028$ GeV. Measurements were made of several D^{*0} parameters. The D^0 mass was found to be $m(D^0) = 1865.3 \pm 1.0 \pm 2.0$ MeV, the $D^{*0} - D^0$ mass difference was found to be $\Delta m = 140.0 \pm 0.5 \pm 1.5$ MeV, and the D^{*0} branching ratio to pions was measured to be $\mathrm{BR}(D^{*0} \to \pi^0 D^0) = 53.1 \pm 3.4 \pm 9.1\%$. Additionally, some information was obtained on charm meson production cross-sections and combined production-and-decay angular distributions.

Acknowledgments

It's 11:58 P.M. on a Saturday night and I've just finished adding the finishing touches to the last equation in the last section of the last (and only) appendix. This is, hopefully, the last late night for a while, at least the last one spent working on this thesis. When I started graduate school I really had no idea how long it could take to finish a Ph.D. in experimental high-energy physics. The time required has frankly been well beyond any expectations I had at the outset by at least two years. However, I am pleased that I still have a strong desire to continue this particular investigation of natural phenomena that constitutes particle physics. The fascination with the phenomena open to our study and partial understanding is still there; indeed, it is stronger than ever before, and I am looking forward to the application of my newly-acquired experience.

I want to take this opportunity to thank some of the people and organizations who have made my studies in physics possible. The number who deserve my appreciation is of such a size that it is difficult to be sure I have included all those who deserve it. I apologize to those whom I have overlooked.

It is with the *deepest* appreciation that I acknowledge the contribution my parents, Jackson R. Cowan and Velma W. Cowan, have made to this work. They have been a constant source of encouragement for me throughout my life and have always been there when I needed them. They have helped in so many ways: through their interest in my work; through financial support; through many long-distance phone calls that brought much comfort; and through their

unselfish love and understanding that no words of mine can express. I believe they are the finest example of what parents should be. This thesis is lovingly dedicated to them.

Also deserving very special mention is my advisor, Donald G. Coyne. He has done an excellent job guiding me through the physics, always ready with suggestions to follow when things came to a standstill. I feel very fortunate to have had someone who took such painstaking efforts to follow every step of the analysis and to let me know whenever it fell short of his expectations. He has spared me many of the pitfalls that a student and advisor may encounter (I know from my contacts with other students), and for this I am very much in his debt. The successful completion of this work is due, in large part, to him.

I want to thank the Princeton Physics Department for providing the chance to experience an excellent graduate education and for the exposure to many persons and ideas I would never have had the opportunity to encounter elsewhere. The department has provided an invaluable, challenging environment and I am grateful for the chance to have benefited from it. In particular, I want to thank Prof. Val Fitch for consenting to be the second reader for this thesis and for his valuable comments and suggestions, and both Prof. John Bakken and Prof. Dan Marlow for serving on the final public oral examination committee. Also, I want to thank Prof. Gerry O'Neill for both his encouragement and for his efforts in establishing the field of colliding-beam physics in the first place.

Others from the Princeton community whom I want to thank include, from both physics and other disciplines, David Anderson, Jon Bagger, Stefan Cordes, Greg Moore, Dennis Nemeschansky, Alan Noell, Karin Rabe, Scot Renn, Chuck Whitmer, Clair Yu, and especially Prof. Kenneth Deffeyes for many intriguing dinner discussions at Stevenson Hall.

It has been an honor to work with the Crystal Ball group, both the SPEAR and the DORIS II collaborations. It is one of the finest experimental groups around. In particular I want to thank Dikran Antreasyan, David Aschman,

Didier Besset, Elliott Bloom, Fatin Bulos, Roy Cabenda, Matteo Cavalli-Sforza, Ron Chestnut, Bob Clare, Susan Cooper, Chad Edwards, Freddy Fridman, John Gaiser, David Gelphman, Gary Godfrey, Bob Hofstadter, Roland Horisberger, Achim Irion, Ken Kees, Stefan Keh, Ian Kirkbride, Wolfgang Koch, Kay Kõnigsmann, Roger Lee, Steve Leffler, Alan Litke, Bill Lockman, Steve Lowe, Bruno Lurz, Dan Marlow, Patty McBride, Wes Metzger, Cathy Newman-Holmes, Bogdan Niczyporuk, Mark Oreglia, Al Osterheld, Rich Partridge, Charlie Peck, Brian Pollock, Frank Porter, Duncan Prindle, Peter Ratoff, Bernie Renger, Chris Rippich, Hartmut Sadrozinski (who started this analysis before me), Dan Scharre, Andreas Schwarz, Tomas Skwarnicki, Karl Strauch, John Tompkins, Klaus Wacker, Wim Walk, Alan Weinstein, and David Williams. I have thoroughly enjoyed my association with such a fine group of physicists.

For secretarial help I want to thank June Belew, the Crystal Ball secretary at SLAC. She was always ready to help at a moment's notice.

I want to thank Thelma Coyle for proofreading all of the text at least once, and some parts several times. She found several very persistent typos.

I want to thank Ralph Nelson of SLAC for many stimulating discussions about radiation transport processes and energy loss phenomena.

I want to thank those persons who encouraged me in following a scientific career. I want to thank Wallace McGill and Charles Murray, my physics and chemistry teachers at Tyner High School, in Chattanooga, Tennessee, for encouraging my interests from the beginning.

I want to thank the Vanderbilt Department of Physics and Astronomy and especially Bob Panvini, Tom Pinkston, Scott Poucher, and Sheldon Stone. I also want to thank Terry Reeves, currently at Vanderbilt, for his friendship and many interesting physics discussions.

As an aside, I want to mention that this document was typeset using the computerized-typography program TEX, written by Donald E. Knuth of Stan-

ford University. I enjoyed typesetting this document using TEX: it has frequently been a nice diversion from physics when the analysis wasn't going so well. More importantly, I have learned a lot about computer algorithms and programming techniques that I probably would have never discovered elsewhere—and this benefit is more important than the fact that the resulting paper is pretty, although I am proud of that too.

The support services rendered by the SLAC Computing Services and the Computation Research Group personnel have been invaluable. Although it is possible to eventually fix most computer bugs by oneself, it is good to have an excellent staff to call on when you need to track down the meaning of an IFY209I error in one's code. I particularly want to thank Mark Barnett, Ginger Brower, Bob Cook, Bill Johnson, Alan Spragens, Bebo White, and Lee Wilcox for their help. I especially want to thank Bob Beach for spending quite some time explaining to me the resources of the Unified Graphics System which was used to make nearly all the illustrations in this paper.

I want to thank W. H. Freeman and Company, Publishers, for their kind permission to reprint Fig. 2.4 on page 25 from the May 1982 issue of SCIENTIFIC AMERICAN.

I want to thank Nina Adelman and the Public Affairs Office of SLAC for the opportunity to introduce many people to the world of particle physics through the SLAC tour program. I learned quite a bit about how non-physicists view basic research programs in general and physics research in particular, as well as accumulating many hours of public-speaking experience. Working with the PAO has been one of the high points of my graduate career.

I want to thank my family and my non-physicist friends for their fellowship and goodwill. I want to thank Jack Wilson for many talks and enjoyable time spent on computer systems; Karen Krieger for her help over the years; Chris and David Tuttle, and Ken and Cathy Yinger for their friendship and prayerful support; Mitch and Donna Bradley, and Christian and Edith Jacobi for their

friendship and lots of discussions about computers; Steve Meyer for his friendship and for the exciting times spent with his four-wheel-drive Cherokee Jeep in the California mountains; and I want to thank all my friends at the Palo Alto Baptist Church, and the Stanford Baptist Student Ministries. Also I want to thank Mark, David, and Tamara Hooper for their hospitality, as I rented a room from them for several years while I was working on this thesis, and for many lively discussions on physics while I lived there.

Finally, I am grateful for having seen a small part of the beauty and charm that the Creator has placed in his creation.

February 7, 1987
Stanford, California

RFC

"The heavens declare his righteousness, and all the people see his glory."

—Psalms 97:6

Table of Contents

List of Tables

List of Illustrations

Chapter 1

Physics of Charm D^* Mesons

1.1 Introduction

1.1.1 *The History of Charm Mesons*

The investigation of the physics of charm mesons has been one of the more successful proving grounds for high-energy physics since the introduction of modern field theories in the 1940s and the construction of sufficiently energetic particle accelerators to confront these theories with experimental results. The possibility that a fourth quark might exist was conjectured from the experimental non-observation of strangeness-changing weak neutral currents: in the early days of the quark model there was no reason to suppose, given the three known u, d, and s quarks, that weak neutral currents should be suppressed with respect to weak charged currents—but nevertheless they were not observed. A fourth massive charm quark (c) would neatly explain this unsettling experimental fact. A four-quark model introduced by Glashow, Iliopoulis, and Maiani[1-4] predicted a natural suppression of weak neutral currents and some completely new physics: narrow, bound $c\bar{c}$ resonant states; the existence of charm mesons; indeed, a whole positronium-like spectroscopy[5] that, as a result of the heavy mass of the new quark, could be studied in terms of non-relativistic potential models.

Charm physics has absorbed much of the effort of the experimentalist as well

as the theoretician: the early predictions of the four-quark scheme were confirmed by the observations of the J/ψ and ψ' in 1974, creating the famous "November Revolution" in high-energy physics.[6–8] The discoveries continued with the D-wave excitation of charmonium, the ψ''; the $3S$-state at 4.03 GeV; the charm- and charm-strange mesons D and D_S; and other structures observed in the ratio R above $E_{\rm cm} = 4.0$ GeV (see Section 1.2.1). Additionally, the charm region has proven to be a good place to examine some types of non-charm physics: studies of the existence and the properties of exotic states such as bound states of three gluons (ggg) and searches for exotic mesons ($q\bar{q}q\bar{q}$) have been performed here.

Investigations in the charm region have promoted constant efforts to improve detector efficiencies and resolutions, and have motivated the study of newer detector technologies such as large-scale CCD* use (yielding position resolutions on the order of a few μm), Čerenkov velocity measurement schemes, and bismuth germanate (BGO) scintillators. The experience gained in the study of charm physics has been invaluable in the design of detectors for the current set of machines under construction or development (SLC, LEP, and the SSC).

1.1.2 *Outline of This Thesis*

The remainder of this chapter presents an outline of this work and a short review of charm physics relevant to the measurements of D and D^* meson properties to be described later. Chapter 2 is a discussion of the experimental apparatus including the accelerator and storage ring, used to generate e^+e^- colliding-beam events, and the detector system, the "Crystal Ball", which was used to record the data. Chapter 3 describes the first part of the data analysis, including the conversion of the original electronics signals to physics information and the selection of colliding-beam events of the type $e^+e^- \rightarrow$ hadrons; in Chapter 4 the

---

* Charge-Coupled Device: a very-large-scale integrated circuit (VLSI) device that integrates the charge arriving in a rectangular array of picture elements, or "pixels", where each pixel can be as small as ~ 2 μm on a side, yielding a spatial resolution $\sigma \sim 5$ μm. The active area of such a device is usually $\gtrsim 1$ cm^2.

description of the analysis of these hadronic events is continued, describing the criteria used to select photon candidates and the generation of inclusive photon and neutral pion energy spectra. Chapter 5 discusses the studies of the D^{*0} decay modes $D^{*0} \to \pi^0 D^0$ and $D^{*0} \to \gamma D^0$ using these inclusive energy spectra, and the results of the measurements are given here. An appendix contains related material on angular distributions and correlations from D^* production and decay.

1.2 Overview of This Analysis

1.2.1 *Physical Processes of Interest*

This study describes the measurement of the $D^{*0} \to \pi^0 D^0$ branching ratio, the D^0 mass, the $D^{*0} - D^0$ mass difference, and presents the information available from angular distributions and correlations in $D^{*0} \to \pi^0 D^0$ decays. All of these measurements are performed with e^+e^- colliding-beam data taken at the $E_{\rm cm}$=4.028 GeV resonance; data samples at $E_{\rm cm}$=3.670 GeV, 3.685 GeV, and 3.772 GeV, respectively, are used to model the non-open charm hadronic backgrounds and for experimental checks. Fig. 1.1 shows the integrated luminosity used at each energy step in this analysis. The amounts of data taken were dictated by limits of available time and competing physics motivations, and were not optimized solely for the goals of this thesis.

Table 1.1 indicates some of the interesting features of the charm region in e^+e^- colliding-beam physics. These features can be seen in the ratio

$$R \equiv \frac{\Gamma(e^+e^- \to \text{hadrons})}{\Gamma(e^+e^- \to \mu^+\mu^-)}. \qquad [1.1]$$

A plot of R as measured by the Crystal Ball experiment is shown in Fig. 1.2;[9] measurements of R by other experiments is shown in Fig. 1.3.

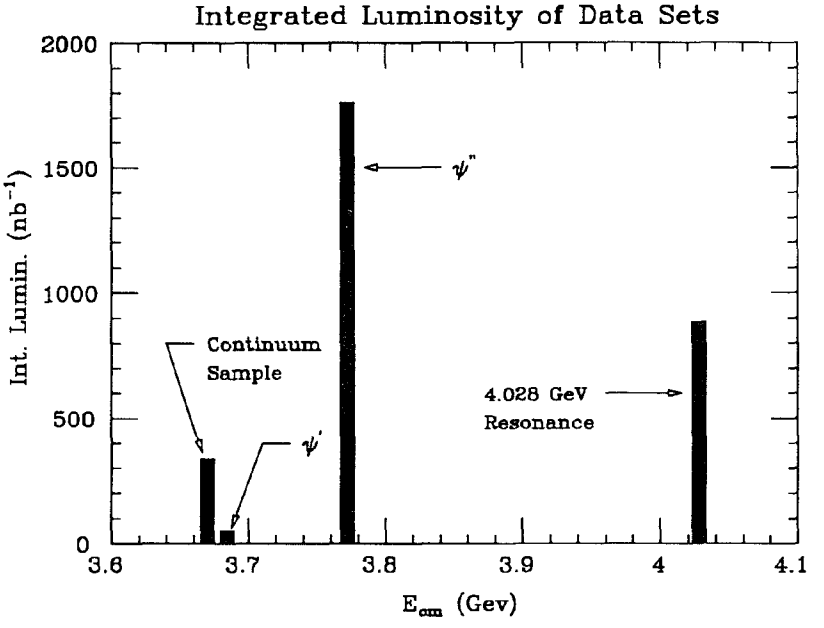

Fig. 1.1 Integrated e^+e^- luminosity of the data sets used in this analysis. These data sets were recorded during 1979–1980.

1.2.2 *The 4.028 GeV Resonance*

The 4.028 GeV resonance, occasionally referred to as the ψ''', or the "$D^*\overline{D}^*$ factory", is the first instance in increasing $E_{\rm cm}$ where significant $D^*\overline{D}^*$ production occurs. The threshold for $D^{*0}\overline{D}^{*0}$ production is $\approx$ 4014 MeV; the D^{*0}'s are produced almost at rest with only some 14 MeV of total kinetic energy. The charge-conjugate mode, $D^{*+}D^{*-}$, has a threshold at 4021 MeV—with only 8 MeV of total kinetic energy.

This value of $\sqrt{s}$ is something of a kinematic curiosity; a $c\bar{c}$ resonance presumed to be $n\,^{2s+1}L_J = 3\,^3S_1$, with its large cross-section, occurring only some 10 MeV above $D^*\overline{D}^*$ threshold, produces $D^*\overline{D}^*$ pairs nearly at rest ($\beta_{D^{*0}} \simeq 0.08, \beta_{D^{*\pm}} \simeq 0.06$). The width of the resonance $\Gamma \approx 50$ MeV overlaps the $D^*\overline{D}^*$ threshold, distorting the resonance and leading to a rapid rise in D^* produc-

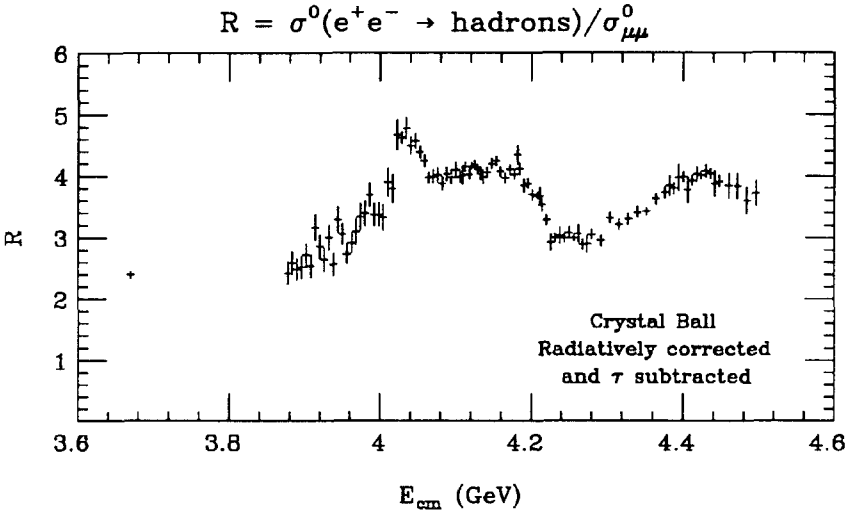

Fig. 1.2 Values of R in the charm region as measured by the Crystal Ball experiment.[9] These values have been corrected for initial state radiation and τ production.

$E_{\rm cm}$ (GeV)	Prominent Features
3.100	$\psi(1S)$ or J/ψ.
3.670	Location of continuum hadron sample. Close to the charm region in energy, but below open-charm threshold.
3.685	$\psi(2S)$ or ψ'.
3.772	$\psi(1D)$ or ψ''. $D\overline{D}$ threshold.
3.870	D^*D threshold.
3.940	$D_S^+D_S^-$ threshold.
4.028	$\psi(3S)$ or ψ'''. $D^*\overline{D}^*$ threshold.
4.170	$D^{**}\overline{D}^*$ threshold. Possible resonance?

Table 1.1 Major structures in the charm region: 3.0 GeV $< E_{\rm cm} <$ 4.5 GeV. Shown are the resonances and thresholds pertinent to this analyis.

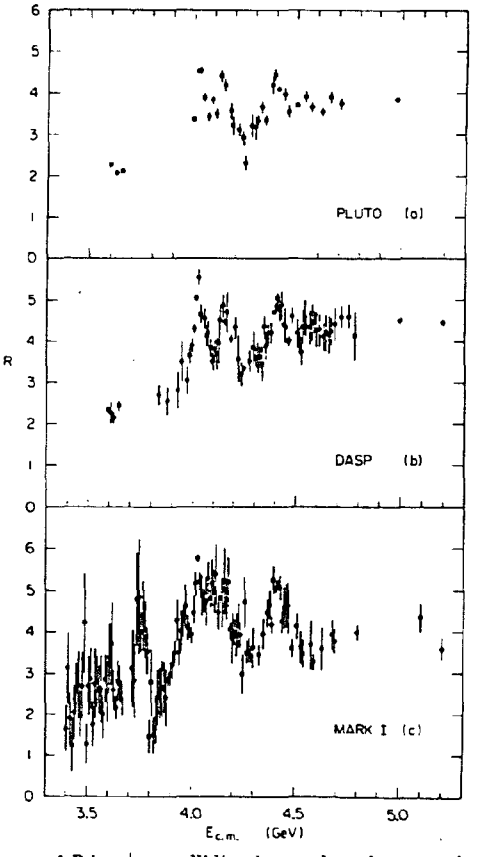

Fig. 1.3 Measurements of R in e^+e^- colliding beams by a few experiments other than the Crystal Ball. These values have been corrected for initial state radiation and τ production.

tion. Furthermore, the small Q-value ($\sim$ 5 MeV) available in the strong decay $D^* \to \pi D$ allows only a small kinetic energy for the pion ($\beta_\pi^{(D^* \text{ rest frame})} \simeq 0.25$); when combined with the small boost of the D^* in the e^+e^- rest frame, the pion provides an efficient experimental tag for detection of the D^*—look for pions nearly at rest. This use of the pion as a tag was anticipated in a fixed target experiment,[10–12] but here is doubly useful because of the large resonant cross-section and the $\pi^0 \to \gamma\gamma$ mode which leaves a distinctive signal in the Crystal

Ball detector.

Angular Distributions

The angular distributions and correlations of the photon and π^0 yield information on the strong interaction matrix elements for D^* production and decay;[14] previous work[15-16] could not observe any non-isotropic effects, so a careful examination is appropriate in this analysis. Using the Crystal Ball detector, an effort can be made to measure the inclusive π^0 angular distributions from D^{*0} decay; even π^0-π^0 angular correlations can be attempted with the existing data, since the low-energy π^0 ($E_{\rm kin} \lesssim 20$ MeV) used as the tag has a distinctive signature: two low-energy photons nearly back-to-back ($\approx 140°$) in angle. However, measurements of the direct photon from D^{*0} decay are not attempted since it is difficult to distinguish these photons from those of other processes in the 120–170 MeV region in the inclusive photon spectrum: the signal-to-background ratio is too weak by a considerable factor, and no distinctive tag is available.

Preliminary attempts for all of these angular measurements were tried but were not entirely successful; either large backgrounds (*e.g.*, in the inclusive π^0 angular distribution from explicitly reconstructed pion four-momenta) or low statistics (*e.g.*, the π^0-π^0 correlation) hamper any significant measurements. The distributions are histogrammed, however, in Chapter 4, but without any fits performed on them. This preliminary work does not rule out the usefulness of the inclusive techniques discussed in Chapter 4 to reduce the backgrounds, but these results are not the major thrust of this thesis and will not be further reported here.

1.2.3 *Crystal Ball Data in the Charm Region*

There are two sets of runs at $E_{\rm cm}$=4.028 GeV which were studied by the Crystal Ball detector. These were recorded in April 1979 and November 1979 (approximately 150 nb^{-1} and 700 nb^{-1}, respectively) with some 25 000 events remaining

after hadron selection (see Chapter 3). Another sample at $E_{\rm cm}$=3.684 GeV (the ψ'), some 50 nb^{-1}, was taken in the same SPEAR running period as the November 1979 data at 4.028 GeV. This allows checks on the calibration and analysis processes by inspecting the energies and linewidths of photons from $\psi' \to \gamma\chi_{0,1,2}$. These energies and linewidths are in agreement with Crystal Ball results from the analysis of 1.7×10^6 ψ' decays.[31] It can be seen from Fig. 1.4 and Table 1.2 that the detector response in the 100–200 MeV photon energy region is acceptable and fairly well understood.

These runs at energies other than 4.028 GeV are very important, as will be seen in Chapter 5, because the branching ratio and mass measurements are extracted from fits to data using Monte Carlo spectra as input. Both energy response and characteristic shapes of inclusive spectra must be modeled sufficiently well by the event simulation algorithms to allow direct comparison with data in the region $50 \lesssim E_\gamma \lesssim 250$ MeV. The real data, taken at increasing energies where new physics manifests itself stepwise, allow the fine-tuning of the simulation programs.

1.3 Previous Measurements of Charm Meson Properties

The D^{*0} mass is measured either directly or by the measurement of the $D^{*0} - D^0$ mass difference, which is then combined with a D^0 mass measurement; measurements have been made both by magnetic detectors in e^+e^- colliding-beams and charm photoproduction experiments using spectrometers. There are several measurements of the D^0 mass extant at present; the weighted average of these (excluding this analysis) is $m(D^0) = 1864.62 \pm 0.59$ MeV.[57] The only measurement of the $D^{*0} - D^0$ mass difference to date independent of this analysis is $m(D^{*0}) - m(D^0) = 142.7 \pm 1.7$ MeV.[18] Previous measurements of the neutral D^{*0} branching ratio to $\pi^0 D^0$ yield a weighted average of $51.5 \pm 7.6\%$.[16,57]

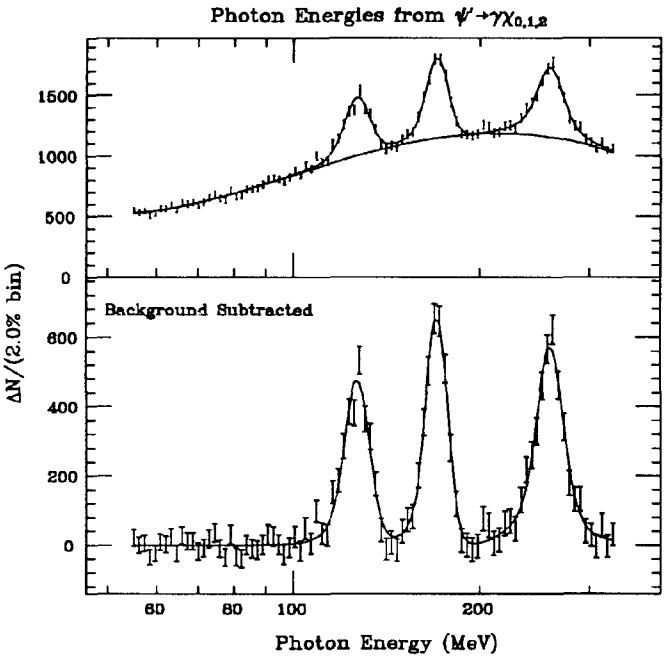

Fig. 1.4 A log-likelihood minimisation fit to the photon energy spectrum from $\psi' \rightarrow \gamma\chi_{0,1,2}$ from data taken in November 1979. The measured energies agree with Crystal Ball results from the analysis of 1.7×10^6 ψ' decays.

Transition	Photon energy (MeV) calculated from November 1979 data	Photon energy (MeV) calculated from 1.7×10^6 ψ' decays
$\psi' \rightarrow \gamma\chi_0$	$258.1 \pm 0.7 \pm 4$	$258.4 \pm 0.4 \pm 4$
$\psi' \rightarrow \gamma\chi_1$	$170.1 \pm 0.5 \pm 4$	$169.6 \pm 0.3 \pm 4$
$\psi' \rightarrow \gamma\chi_2$	$126.1 \pm 0.3 \pm 4$	$126.0 \pm 0.2 \pm 4$

Table 1.2 Measured energies of photons from the process $\psi' \rightarrow \gamma\chi_{0,1,2}$ from data taken at E_{cm}=3.684 GeV in November 1979. The energies are from a log-likelihood minimization fitting the data to resolution- and Doppler-broadened lines with a polynomial background. The first error is statistical, the second is systematic.

1.4 Theory Predictions for Charm Meson Masses and Widths

The small Q-value of the $D^* \to \pi D$ transition makes this decay particularly interesting since it allows the D^* electromagnetic photon decay to compete with a phase-space-limited strong decay—the larger the $D^{*0} - D^0$ mass difference, the greater the D^{*0} width to pions. The study of this decay can yield some indication of the symmetry-breaking effects in an SU(4) scheme.

A non-relativistic calculation by Ono,[13] using harmonic oscillator wavefunctions to describe the $c\bar{u}$ system, provides estimates of the D^{*0} widths:

$$\Gamma(D^{*0} \to \pi^0 D^0) = \frac{1}{3}\frac{k^3}{2\pi}\left(\frac{f_q}{m_\pi}\right)^2 I_u^2(k) \qquad [1.2]$$

and

$$\Gamma(D^{*0} \to \gamma D^0) = \frac{4}{3}k'^3\left[\mu_u I_u(k) + \mu_c I_c(k)\right]^2 \qquad [1.3]$$

where $k(k')$ is the momentum of the pion (photon) in the D^{*0} rest frame; f_q is the strength of the (u,d)-π coupling, determined from $f_q = 3/5\, f_{\pi N}$, where $f_{\pi N}^2/4 = 0.082$; μ_u and μ_c are the magnetic moments of the quarks, assuming gyromagnetic ratios of unity; and I_u, I_c, the overlap integrals, are functions of the u- and c-quark masses. The overlap integrals are nearly one ($\gtrsim 0.99$[20]) for values of $m(D^{*0}) - m(D^0) < 600$ MeV and will be taken as exactly unity here. This yields a prediction for the $D^{*0} \to \pi^0 D^0$ branching ratio

$$\mathrm{BR}(D^{*0} \to \pi^0 D^0) = \frac{\frac{1}{3}\frac{k^3}{2\pi}\left(\frac{f_q}{m_\pi}\right)^2 I_u^2(k)}{\frac{1}{3}\frac{k^3}{2\pi}\left(\frac{f_q}{m_\pi}\right)^2 I_u^2(k) + \frac{4}{3}k'^3\left[\mu_u I_u(k) + \mu_c I_c(k)\right]^2} \qquad [1.4]$$

Using the parameter values above, and setting $I_u = 1$, $I_c = 1$, it is found that

$$\mathrm{BR}(D^{*0} \to \pi^0 D^0) = \left[1 + \frac{1}{62.1}\left(\frac{k'^3}{k^3}\right)\right]^{-1}. \qquad [1.5]$$

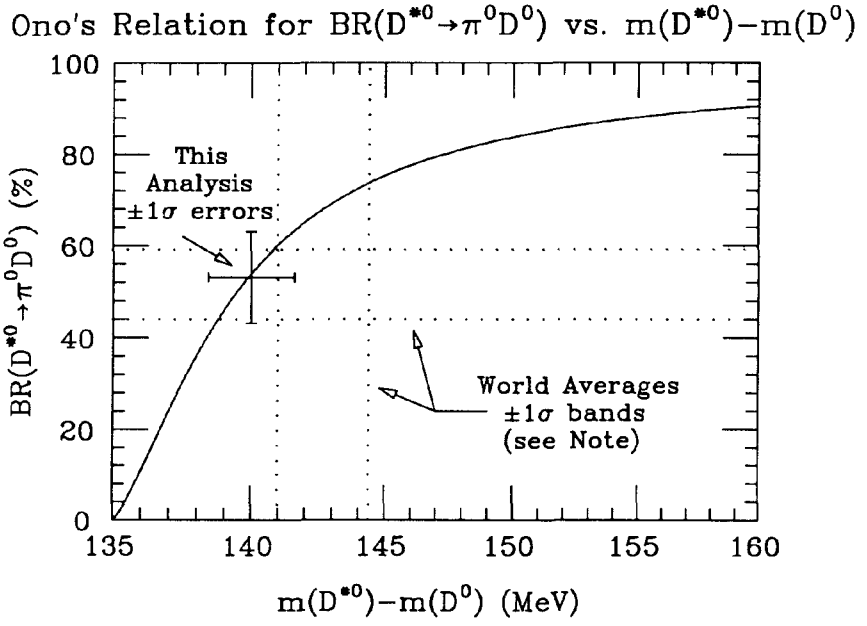

Fig. 1.6 The relation derived by Ono[13] for the branching ratio BR($D^{*0} \to \pi^0 D^0$) as a function of the $D^{*0} - D^0$ mass difference. The point indicates the values found in this analysis with statistical and systematic uncertainties combined in quadrature (see Chapter 5). The bands indicate the world averages from Ref. 57, excluding this analysis. NOTE: The Sadrozinski result[21] contained in the world average for $m(D^{*0}) - m(D^0)$ has been removed from the values in this figure since it is not independent of this analysis.

The relation given by Eq. [1.5] is shown in Fig. 1.6; also indicated is the point found by this analysis (see Chapter 5), and the one-standard deviation bands about the world averages.

Another calculation of D^* decay widths has been given by Thews[22,23] using finite-energy sum rule (FESR) methods. This gives values for the D^{*0} partial decay widths:

$$\Gamma(D^{*0} \to \pi^0 D^0) = 4 \pm 3 \text{ keV} \quad \text{and} \qquad [1.6]$$

$$\Gamma(D^{*0} \to \gamma D^0) = 4 \pm 2 \text{ keV}. \qquad [1.7]$$

Decay	Predicted Branching Ratio	Experimental Branching Ratio
$D^{*+} \to \pi^0 D^+$	30.9 %	34.9 ± 7.0 %
$D^{*+} \to \pi^+ D^0$	67.8 %	48.9 ± 8.3 %
$D^{*+} \to \gamma D^+$	1.8 %	17 ± 11 %
$D^{*0} \to \pi^0 D^0$	70.6 %	51.5 ± 7.6 %
$D^{*0} \to \gamma D^0$	29.4 %	48.5 ± 7.6 %

Table 1.3 Predicted and measured D^* branching ratios. The predicted values are from Ref. 25; experimental values are the world averages, excluding this analysis, from Ref. 57.

Assuming that the theoretical uncertainties associated with these predictions may be interpreted as one-standard-deviation "errors",* the branching ratio is calculated to be

$$\mathrm{BR}(D^{*0} \to \pi^0 D^0) = \frac{\Gamma(D^{*0} \to \pi^0 D^0)}{\Gamma(D^{*0} \to \pi^0 D^0) + \Gamma(D^{*0} \to \gamma D^0)} \qquad [1.8]$$

$$= 0.5 \pm 0.6, \qquad [1.9]$$

a value near the observed result but with errors so large it cannot be used as a test; it is hoped that the measurement of the mass difference given in this analysis will help in constraining this FESR prediction.

In another calculation, Rosner[25] gives a set of branching ratio predictions for D^* decays based upon experimental numbers for the similar K^* decays. These, along with the world averages of experimental results (excluding this analysis), are given in Table 1.3.

---

* This is a reasonable assumption since the errors reflect experimental uncertainty in the $D^{*0} - D^0$ mass difference used in the calculation.

1.4.1 *Uses of the D^{*0} Measurements*

Measurements of D^* properties have applications in several fields of current interest. First, the branching ratios are needed to analyze B meson decays from the Υ region; the Cabibbo-favored $b \rightarrow c$ decay necessitates an accurate knowledge of the D^* decay parameters to understand the decays of the B. An example is the analysis of the decay

$$\begin{array}{l} B^- \rightarrow D^{*0} + \bar{\nu}_e + e^- \\ \qquad\quad \lfloor\!\!\longrightarrow \pi^0 + D^0 \end{array} \qquad [1.10]$$

which is presently under study by the Crystal Ball collaboration. The precise knowledge of $m(D^{*0}) - m(D^0)$ is crucial to the analysis. Second, the recent discovery[19] of a likely candidate for the P-wave excitation in the $c\bar{q}$ system, the $D(2420)$, decaying into πD^* has renewed the demand for an accurate D^* branching ratio measurement. This is partially because the experimental analysis of the $D(2420)$ involves a transition to the D^*, but also because the radiative D^* decay is a useful theoretical calibration point for heavy-meson decay predictions.[25] Given the D^* branching ratios, one can use them to include SU(4) symmetry-breaking effects in calculations of $D(2420)$ properties. Third, experimental values of charged and neutral D^* branching ratios, when combined with SU(4) symmetry arguments, yield rates for radiative D^* decays that are inconsistent with theoretical calculations utilizing SU(4) symmetry-breaking schemes;[24] this inconsistency needs more information to be resolved—it may be that current experimental results are in error as well as the theoretical constraints.

1.4.2 *Charm Cross-Sections*

The coupled-channel charmonium model of Eichten *et al.*[26-27] has been successful in calculating the cross-sections for the various charm processes as a

function of $E_{\rm cm}$. In the analysis of the data for this thesis, cross-section measurements are made (although they are subject to large systematic uncertainties, and are therefore not one of the primary results) and may be compared with the coupled-channel model at $E_{\rm cm} = 4.028$ GeV. Figs. 1.7–1.8 illustrate the behavior of the coupled-channel model cross-sections *vs.* $E_{\rm cm}$. These were calculated using the mass values $m(D^0) = 1865$ MeV, $m(D^{*0}) = 2007$ MeV, $m(D_S) = 1970$ MeV, and $m(D_S^*) = 2070$ MeV.* The sum of the cross-sections is shown in Fig. 1.9.

Comparison of the coupled-channel predictions with the results from this analysis is perhaps not fully justified due to the large systematic uncertainties in the cross-section measurements; however, a brief look is appropriate. Anticipating a later discussion in which the cross-section results of this analysis will be presented (see section 5.5.5), they are previewed in Table 1.4. For convenience, cross-sections will be expressed in units of R. Note that the sum of the measurements is $R_{\rm total}^{\rm (meas)} = 6.01$, somewhat higher than the typical experimental values of R at $E_{\rm cm} = 4.028$ GeV (we will neglect radiative corrections here since they are on the order of $\lesssim 10\%$). In Table 1.4, the predicted values are found; here the sum is $R_{\rm total}^{\rm (coup-chan)} = 4.88$ (a constant value of 2.0 has been added to account for non-charm physics). In order to compare them, both predictions and data are normalized to $R_{\rm total} = 5.0$, as is also given in Table 1.4.

As will be discussed later in Chapter 5, the measurements performed here are not independently sensitive to each possible charm meson production process. Measurements are available only in the combinations listed in the table, because of the similarity of photon and neutral pion spectra that their respective decay products produce, or because of phase space suppression factors. Note also that isospin invariance has been invoked in the measured fits for $D\overline{D}$ and $D^*\overline{D} + D\overline{D}^*$ production.

---

* A computer program supplied to the Crystal Ball collaboration by Eichten was used to produce these figures. The program allowed only slight adjustments to be made in the meson masses without violating its range of applicability.

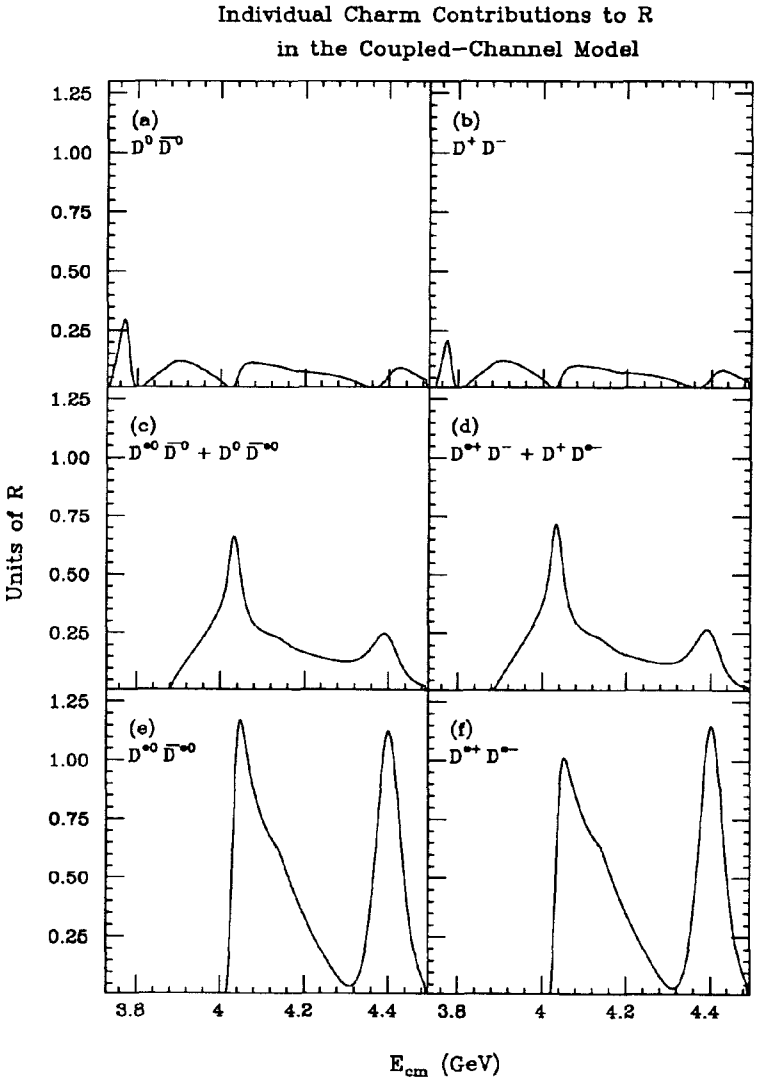

Fig. 1.7 Charm contributions to R using the charm coupled-channel model[26-27] for the six charm non-strange processes. See the discussion in the text for the D, D^*, and D_S masses used.

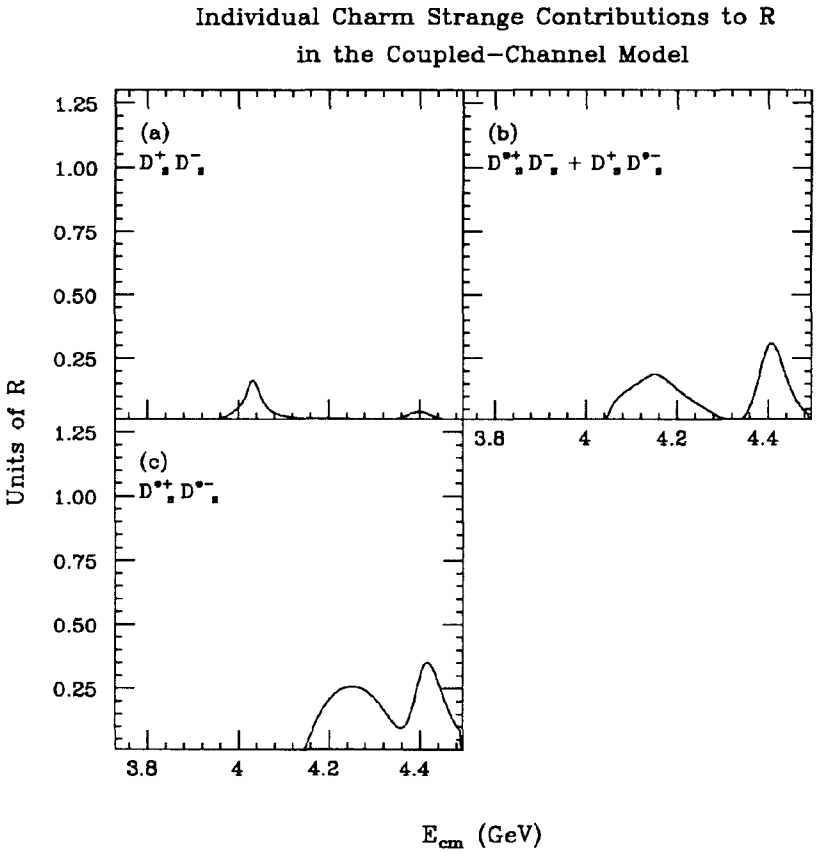

Fig. 1.8 Charm contributions to R using the charm coupled-channel model[26-27] for the three charm-strange processes. See the discussion in the text for the D, D^*, and D_S masses used.

With these caveats, inspection of Table 1.4 shows consistency between the coupled-channel predictions and the observed values in all but one case: $D^{*0}\overline{D}^{*0}$ production. Here there is better than a factor of two difference, with the measured value being smaller. Perhaps it should be noted, however, that viewed as a function of $E_{\rm cm}$, the $D^{*0}\overline{D}^{*0}$ cross-section is rapidly changing in the vicinity of $E_{\rm cm}$=4.028 GeV, and small changes in parameters in the model may possibly make large changes in the cross-section. In summary, no significant discrepancies

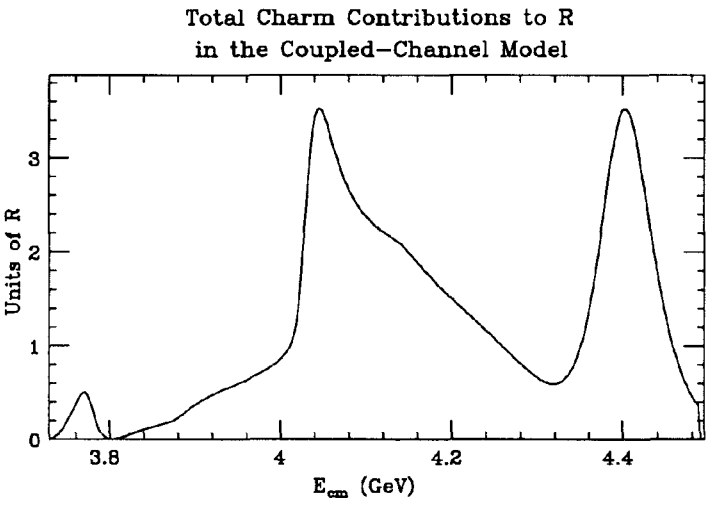

Fig. 1.9 Total charm contributions to R using the charm coupled-channel model.[26–27] See the discussion in the text for the D, D^*, and D_S masses used.

Process	Coupled-channel Model (R)		This Analysis (R)	
	Initial	Scaled	Initial	Scaled
"Continuum-like"	2.69	2.76	4.40	3.66
$D^{*0}\overline{D}^{0}+D^{0}\overline{D}^{*0}$	0.67	0.69	0.64	0.53
$D^{*+}D^{-}+D^{+}D^{*-}$	0.72	0.74	0.64	0.53
$D^{*0}\overline{D}^{*0}$	0.80	0.81	0.33	0.27
Totals	4.88	5.00	6.01	5.00

Table 1.4 Comparison of charm meson production cross-sections from the coupled-channel model and from this analysis. The cross-sections, expressed in units of R, are given, along with the same values normalised to the nominal total value of five. The "continuum-like" entry includes the following: non-open charm and non-charm continuum, $D^{0}\overline{D}^{0}$, $D^{+}D^{-}$, $D^{*+}D^{*-}$, and $D_S^{+}D_S^{-}$ processes (see text).

are noted between the coupled-channel model and the measurements, with the possible exception of $D^{*0}\overline{D}^{*0}$ production.

Chapter 2

Detector Apparatus

2.1 Introduction

The possibility of building a large non-magnetic detector designed specifically for measuring photon energies to a few percent was first seriously discussed during the 1974 PEP Summer Study.[29-31] Work performed by R. Hofstadter and colleagues[32] had shown that thallium-doped sodium iodide, NaI(Tl), was a most promising material for the high-resolution measurement of energy deposited by electromagnetic showers. A proposal for the construction of such a device was approved in the spring of 1975 and the "Crystal Ball", as it had come to be known, was finished in the spring of 1978. The detector recorded the first physics data in the fall of 1978 at the SPEAR e^+e^- storage ring at the Stanford Linear Accelerator Center in Stanford, California.

2.2 The SPEAR Colliding Beam Ring

The SPEAR* facility at SLAC is an electron-positron colliding-beam storage ring with an energy range of 2.4 GeV $< \sqrt{s} <$ 7.4 GeV, where $\sqrt{s}$ is the total

* SPEAR is an acronym for the Stanford Positron Electron Asymmetric Ring.

energy E_{cm} in the center-of-momentum frame.† SPEAR was completed in 1972, and has run in its present configuration since an upgrade in 1974.

2.2.1 *Description of SPEAR*

The layout of SPEAR is shown in Fig. 2.1. The magnet lattice consists of dipole horizontal bending magnets and quadrupole focusing magnets. Single "bunches" of electrons and positrons circle the single beampipe in opposite directions with a period of 780 nsec. The beampipe in the interaction region is made of aluminum, 110 mm in diameter, and is evacuated to $\approx 10^{-9}$ torr. The wall thickness is 65 mils (0.019 radiation lengths) at normal incidence. Four radio-frequency (rf) cavities are used to compensate for energy lost via synchrotron radiation. The two interaction regions, where the beams collide at a 0° crossing angle, are diametrically opposite and are labelled the "East Pit" and the "West Pit" in Fig. 2.1. The Crystal Ball detector was housed in the East Pit from autumn 1977 to autumn 1981.* The SPEAR control and power supply buildings are located near the center of the ring.

Throughout this discussion, the "SPEAR coordinate system" will be used. These coordinates are defined at any given point around the design orbit by

(1) the $+z$-direction is the direction of the positron beam,

(2) the $+x$-direction points toward the center of the ring, and

(3) the $+y$-direction is vertical (opposite to the direction of the magnetic bend field).

---

† E_{cm} is defined by the relation $E_{cm} = 2 \times E_{beam}$, where E_{beam} is the nominal energy of either a positron or an electron in the laboratory system.

* The Crystal Ball detector was moved to the Deutches Elektronen Synchrotron laboratory (DESY), Hamburg, W. Germany, in the spring of 1982 to study Υ physics.

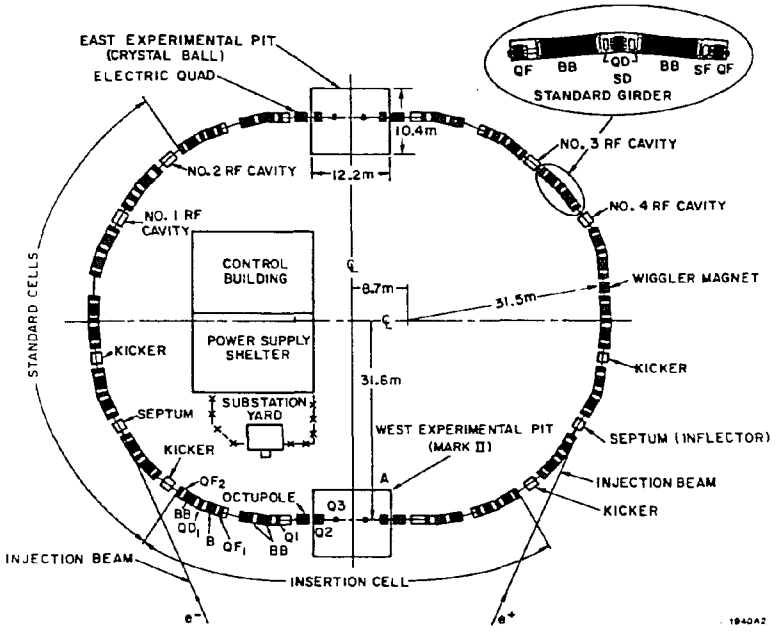

Fig. 2.1 The SPEAR electron-positron colliding-beam storage ring, showing the layout of the e^+e^- injection lines, magnet lattice, control buildings, and experimental areas. The Crystal Ball detector was located in the East Pit from autumn 1978 until autumn 1981.

2.2.2 *SPEAR Operation*

The e^+ and e^- beams originate in the 2-mile long SLAC linear accelerator.[30] Positron injection is done first, followed by electron injection, taking approximately 20 minutes per beam. The injection process is called *filling* the ring, and the useful running time until about half of the initial beam currents are lost is called a *fill*. After acceleration to the desired injection energy (up to a maxi-

mum of $E_{\rm beam} = 2.5$ GeV for SPEAR), the beams are transported through the SLAC beam switchyard, enter their respective injection lines, and are added to the SPEAR beam currents. One bunch of electrons and one bunch of positrons orbit the SPEAR ring in opposite directions with a frequency of 1.28 MHz.

The beams experience betatron and synchrotron oscillations as they orbit the ring. Betatron oscillations occur in the horizontal x-direction, and couple to oscillations in the longitudinal z-direction via lattice imperfections. Vertical oscillations are an order of magnitude less than the betatron oscillations. Compensation for synchrotron radiation causes the bunches to become elongated, with an approximately gaussian distribution.[33] At the interaction points, these gaussian-shaped beams have a $\sigma_x \approx 0.06$ cm and $\sigma_y \approx 0.004$ cm. The longitudinal beam spread is caused by quantum fluctuations in the synchrotron radiation, and is about 2.4 cm at $E_{\rm cm} = 4.3$ GeV. The size of the luminous region is about a factor of $\sqrt{2}$ less than the beam size.

The synchrotron energy loss varies as $\sim E_{\rm beam}^4$ (up to $E_{\rm beam} \lesssim 3.5$ GeV), and is approximately 46 keV/revolution at $E_{\rm beam} = 2.014$ GeV. The rf cavities run at a frequency of 280 $\times$ the revolution frequency. The energy spread, like the beam spread, is limited by quantum fluctuations in the synchrotron radiation; typically, each beam has an energy width of about 1 MeV at the ψ' resonance.

An e^+e^- interaction is called an *event*. The event rate for a particular process, dN/dt, is given by

$$\frac{dN}{dt} = \mathcal{L}\sigma \qquad [2.1]$$

where the cross-section for the process is σ and the machine luminosity is $\mathcal{L}$. A typical luminosity for SPEAR with $E_{\rm cm} > 4$ GeV is $\mathcal{L} \approx 4 \times 10^{30}$ cm^{-2} sec^{-1} at the start of a fill; a fill will typically last four hours, during which the beam currents will drop by a factor of two; at the start of a fill, beam currents are usually 10–15 mA. A long-term average would typically find an integrated luminosity, $\int \mathcal{L}\, dt$, of some 50 nb^{-1}/day at $E_{\rm beam} = 4.03$ GeV.

2.3 The Crystal Ball Detector

The Crystal Ball detector as installed in the East Pit at SPEAR in 1979 is shown in Fig. 2.2. The apparatus consists of a highly segmented array of NaI(Tl) scintillator crystals, charged tracking chambers, and data acquisition electronics. Figs. 2.3 and 2.4 show the arrangement of these devices. The configuration of the Crystal Ball detector as installed at SPEAR has been described at length in several papers;[37,38] here, an overview of the detector design and operation is presented in the next several sections.

2.3.1 *Main NaI(Tl) Hemispheres*

Two NaI(Tl) hemispheres form the central part of the Crystal Ball detector. They are constructed from 672 NaI(Tl) scintillator crystals, each 16 radiation lengths long. See Fig. 2.5. The hemispheres have an energy resolution

$$\frac{\sigma(E)}{E} = \frac{0.026 \pm 0.001}{\sqrt[4]{E}} \quad (E \text{ in GeV}), \qquad [2.2]$$

and an angular resolution, depending also on energy, of 1–2° (higher-energy photons will populate more crystals, yielding more information about the lateral shape of the shower; this allows a more accurate position determination).*

The geometry of the nearly spherical hemispheres is based on that of the icosahedron, as in Fig. 2.6. The icosahedron is a regular geometrical solid with 20 sides, as shown in Fig. 2.6(a). Each side is an equilateral triangle, and is called a *major triangle*. Each major triangle is divided into four smaller equilateral

---

* The energy resolution in Eq. [2.2], $\sigma_0 = 0.026$, is observed in Bhabha events after calibration (see section 2.5 below). The deviation of the functional form of the energy resolution, $\sigma/E \propto 1/\sqrt[4]{E}$, from a square-root law arises in part from shower leakage from the crystals.

The angular resolution quoted here is from Monte Carlo studies. It is consistent with the resolution found in kinematic fits to well-constrained final states; inspection of the distribution of θ- and ϕ-pulls from kinematic fits to data and to Monte Carlo events (performed separately) indicates similar angular errors.[49]

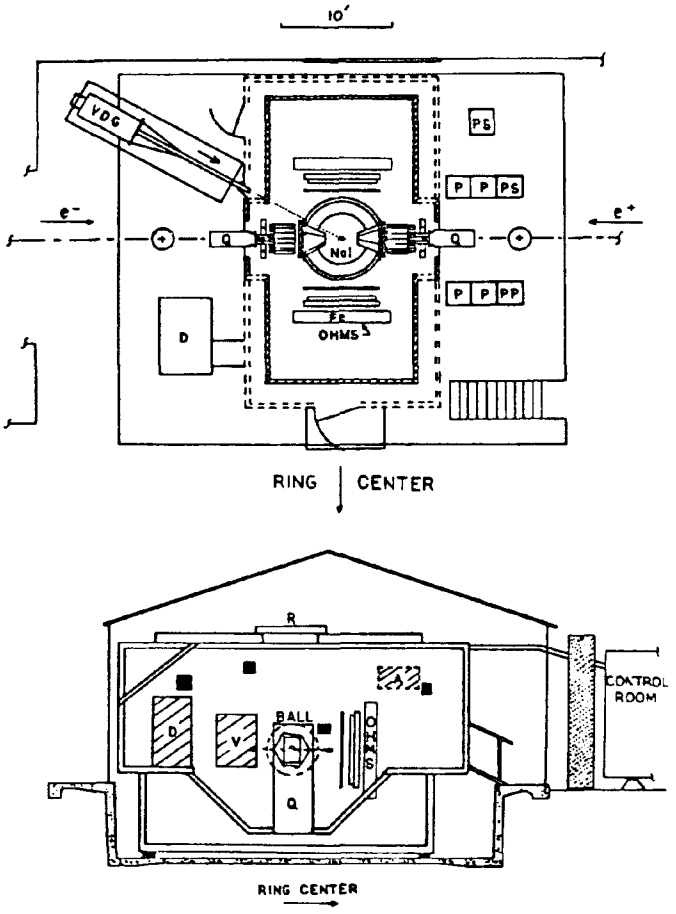

Fig. 2.2 Illustrative drawing of the Crystal Ball detector installation at SPEAR in 1979. The principal components shown in the upper figure are:[37] VDG=Van de Graaff system; D=dehumidifier; PS=power supply for the charged tracking chambers; P=high-voltage pulser, PP=prepulser for the spark chambers; and Q=quadrupole magnet. The outermost environmental enclosure is shown by the double-dashed line. In the lower figure: D=door; V=Van de Graaff proton beam entry port; A=dehumidifier port; Q=quadrupole magnet port; and R=rooftop access port. The shaded material to the left of the control room is concrete for radiation shielding.

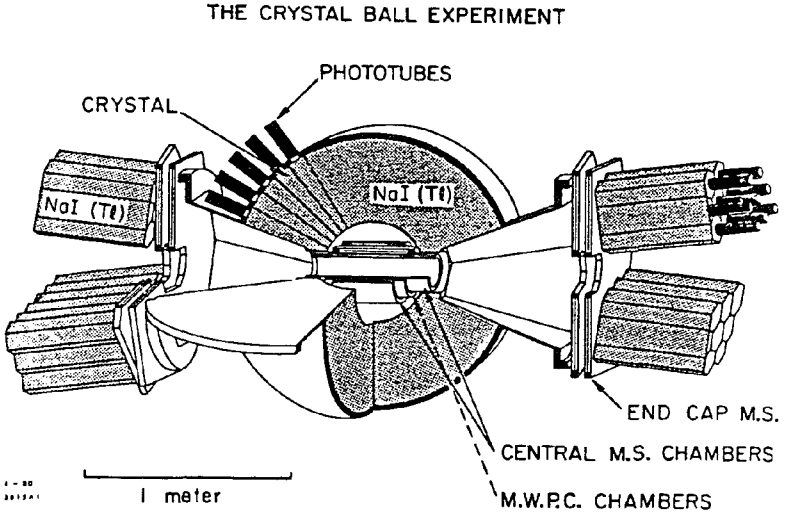

Fig. 2.9 The Crystal Ball experimental apparatus, showing the arrangement of the charged particle tracking chambers, the two hemispheres of NaI(Tl) scintillator crystals, and NaI(Tl) endcap arrays.

triangles†, called *minor triangles*. See Fig. 2.6(b). Each minor triangle is divided into nine triangular modules. Each module in this geometry corresponds to one NaI(Tl) crystal. See Fig. 2.6(c).

The two halves of the ball are hemispherical shells, allowing for placement of the charged tracking chambers inside them. The inner radius of the NaI(Tl) is 10 inches and the outer radius is 26 inches.

† Note that these four minor triangles do not lie in a plane.

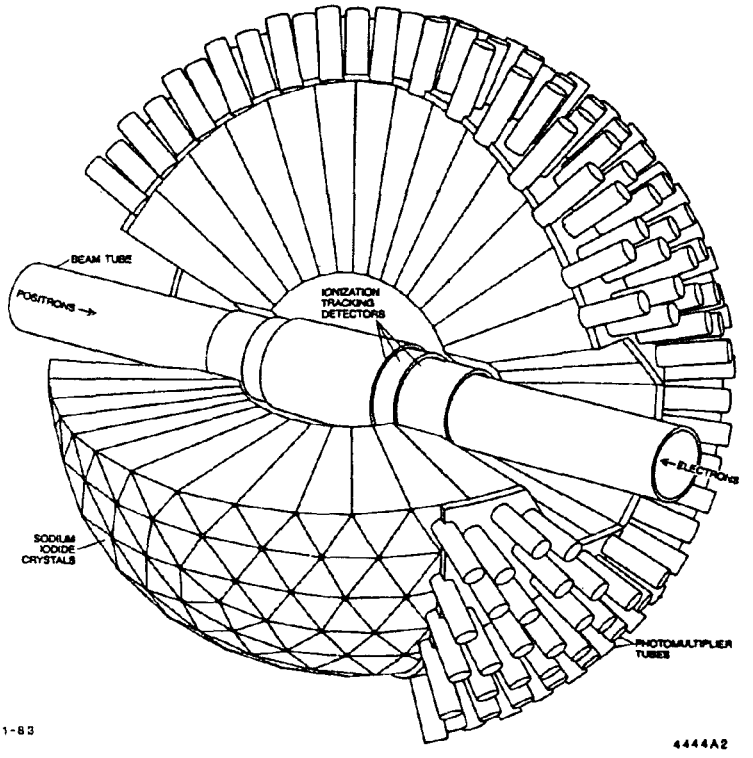

Fig. 2.4 A cut-away drawing of the Crystal Ball central hemispheres showing the beampipe entry and exit tunnels, the charged tracking chambers, and the photomultiplier tubes. [From *Quarkonium*, by Elliott D. Bloom and Gary J. Feldman. Copyright © 1982 SCIENTIFIC AMERICAN, Inc. All rights reserved. Used by permission.]

2.3.2 *Endcap NaI(Tl) Arrays*

The sodium iodide hemispheres of the detector cover 94% of the 4π steradian solid angle. This coverage is supplemented by the addition of four sodium iodide crystal endcap arrays, bringing the total solid angle coverage to 98%.[39] See Fig. 2.3. The endcap arrays are located outside of the hemispheres and are

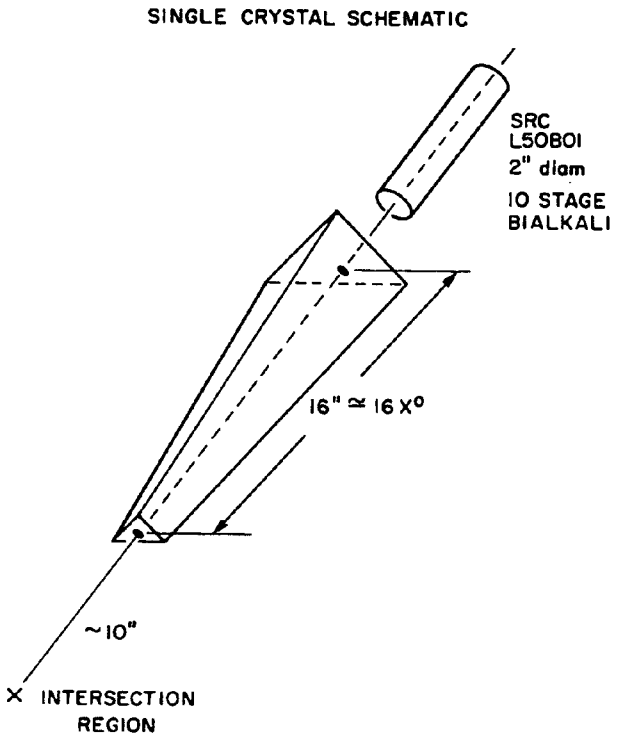

Fig. 2.5 A single NaI(Tl) crystal in the main hemispheres and its phototube. The crystal is 16 radiation lengths long.

tilted at an angle of 7° to the beam. There are 15 crystals in each array with an hexagonal cross-section six inches across from corner to corner. Twelve of the crystals in each array are 20 radiation lengths long; the other three are ten radiation lengths long.* Each crystal is viewed by a phototube attached to the rear window of the steel canister in which it is sealed. In front of each array is a double layer of magnetostrictive spark chambers for charged-particle tracking.

* These crystals were obtained from an earlier apparatus which used these shorter lengths.

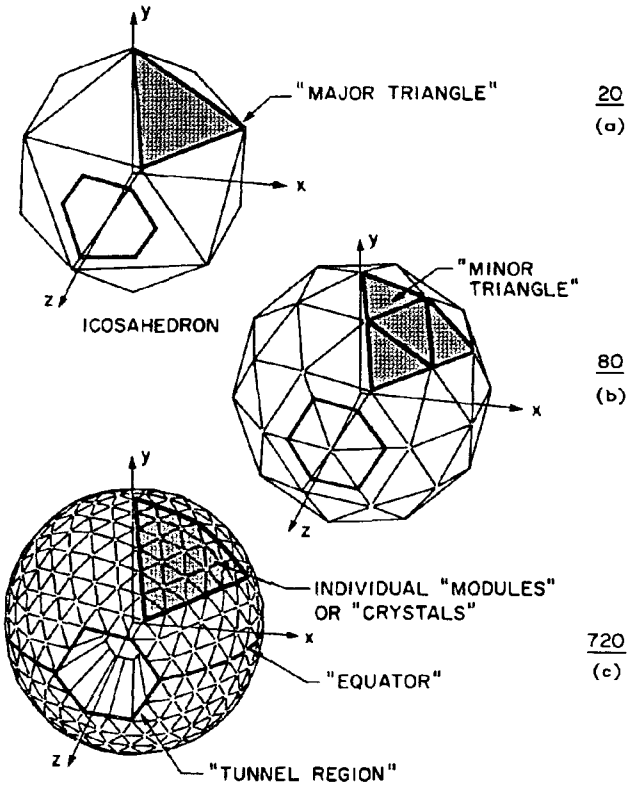

Fig. 2.6 The nearly spherical division of an icosahedron into 720 individual modules is the basis of the Crystal Ball geometry. (a) The twenty-sided icosahedron, illustrating the division into major triangles. (b) The division of each major triangle into four minor triangles. (c) The division of each minor triangle into nine modules, yielding a total of 720 possible module locations. Only 94% of the total 4π steradian solid angle is occupied by the modules, leaving space for the beampipe entry tunnels.

Detector Component	Radial Distance (mm)	Thickness‡ (% rad. length)	Solid Angle (% of 4π)	FWHM Azimuthal Resolution (mrad)	FWHM Polar Resolution (mrad)	Efficiency ϵ (%)
Aluminum Beampipe	59	1.9	100	—	—	—
Magnetostrictive Spark Chamber 1	79	2.0	94	25 ± 5	150 ± 20	70–75
Multiwire Proportional Chamber	100	0.35	83	35 ± 2	75–180	90–98
Magnetostrictive Spark Chamber 2	137	2.0	71	25 ± 5	115 ± 15	70-75
Steel Inner Shell	254	4.3	94	—	—	—

Table 2.1 Magnetostrictive spark and multiwire proportional chamber parameters. Also included are other inner detector components.

2.3.3 *Charged Tracking Chambers*

Enclosed in the 10 inch radius cavity inside the crystal hemispheres is the charged tracking system consisting of three double layers of magnetostrictive spark chambers (called *MSSC*s) and multiwire proportional chambers (called *MWPC*s). There are three double layers of chambers: first, a double layer spark chamber with two spark gaps; next, a double layer multiwire proportional chamber, and last another double layer spark chamber.[38] The various chamber parameters are given in Table 2.1.

Multiwire Proportional Chambers (MWPCs).

The MWPCs are located between the two spark chamber layers. They consist of one double layer of aluminum-coated mylar and wires. See Fig. 2.7(a). There are three cylindrical shells of aluminum-coated mylar with 144 gold-plated tungsten wires 20 μm in diameter in each gap spaced $\approx$ 4.5 mm apart. The solid

‡ At normal incidence.

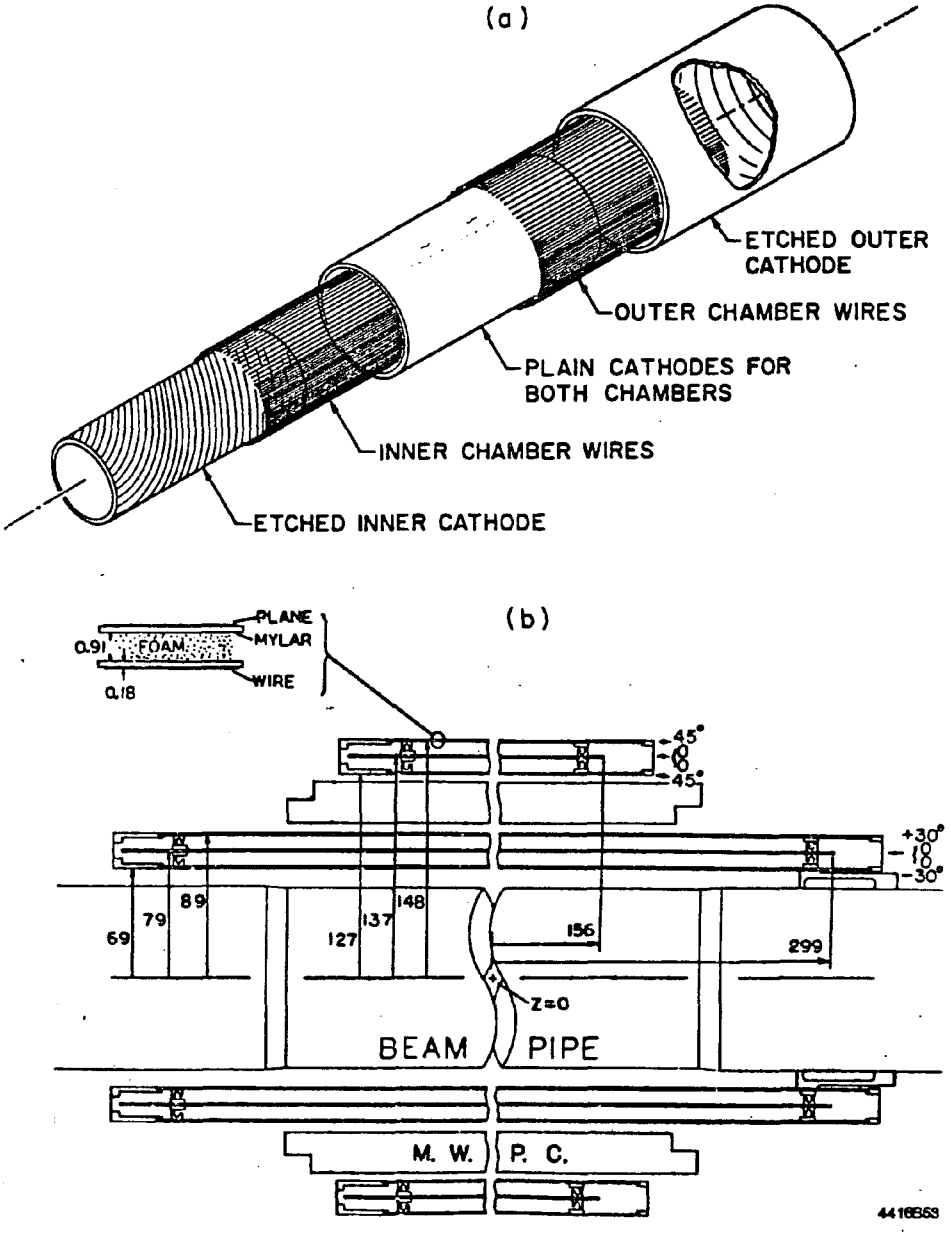

Fig. 2.7 The Crystal Ball charged tracking chambers during 1979. (a) The multiwire proportional chambers. (b) The magnetostrictive spark chambers. Arrows indicate distances from the beam axis in millimeters.

angle coverage is 83%. The inner cathode of the inner layer is etched into strips 7 mm wide on 8 mm center-to-center spacing and inclined at 62°. The outer cathode of the outer layer is etched into strips 7 mm wide on 9 mm center-to-center spacing and inclined at 90°. The other cathode of each chamber is not etched. The cathodes are operated at -1.7 kV and the chambers run in proportional mode. Moving from the inner layer to the outer layer the components are:

1. The inner cylindrical shell of aluminum-coated mylar, consisting of:
   (a) Shield ground plane; and
   (b) High-voltage cathode plane (cross-etched aluminum).
2. Inner gap (90% Ar and 10% CO_2), consisting of:
   (a) First 5 mm gap;
   (b) 144 signal anode wires at high-voltage ground potential; and
   (c) Second 5 mm gap.
3. The middle cylindrical shell of aluminum-coated mylar, consisting of:
   (a) High-voltage cathode plane for first gap; and
   (b) High-voltage cathode plane for second gap.
4. Outer gap (90% Ar and 10% CO_2), consisting of:
   (a) Third 5 mm gap;
   (b) 144 signal anode wires at high-voltage ground potential; and
   (c) Fourth 5 mm gap.
5. The outer cylindrical shell of aluminum-coated mylar, consisting of:
   (a) High-voltage cathode plane (cross-etched aluminum); and
   (b) Shield ground plane.

The MWPCs record the angles of wires with charged hits and the signals from the etched cathode strips. Because the MWPCs have essentially no deadtime, their signals are used by the electronics in conjunction with the crystal/phototube outputs to decide whether or not to record a particular event.

Magnetostrictive Spark Chambers (MSSCs)

The spark chambers are illustrated in Fig. 2.7(b). The inner MSSC covers 94% of the total solid angle and the outer chamber covers 71%. Each MSSC has two spark gaps formed from three concentric cylindrical shells of copper-coated mylar sheets. Each shell is constructed of two mylar sheets (5.0 mil thick) with a

1.5 mil copper coating, and separated by 40 mils of styrofoam, assembled together with epoxy. The construction of each MSSC in order of increasing distance from the beam is:[38]

1. Inner cylindrical shell of copper, mylar, styrofoam, and epoxy, consisting of:
   (a) Shield ground plane (1.5 mil copper); and
   (b) High-voltage return ground plane (1.5 mil cross-etched copper).
2. First spark gap (9 mm, filled with 90% Ne, 10% He gas mixture).
3. Middle cylindrical shell of copper, mylar, styrofoam, and epoxy, consisting of:
   (a) High-voltage plane (1.5 mil straight-etched copper);
   (b) Styrofoam fill material; and
   (c) High-voltage plane (1.5 mil straight-etched copper).
4. Second spark gap (9 mm, filled with 90% Ne, 10% He gas mixture).
5. Outer cylindrical shell of copper, mylar, styrofoam, and epoxy, consisting of:
   (a) High-voltage return ground plane (1.5 mil cross-etched copper); and
   (b) Shield ground plane (1.5 mil copper).

The etched strips were 0.3 mm wide and located on 1.0 mm centers; the cross-etched strips were inclined at 30° for the inner MSSC and at 45° for the outer MSSC, and were etched with opposite helicities to minimize reconstruction combinatorics.

The spark chambers were not used in the decision made by the electronics to record an event since the recovery time was quite long. Instead, when such a decision was made, based on information from the crystals and the MWPCs, the spark chamber high-voltage supply was pulsed to 9.0 kV across the 9 mm gaps, and ionization left by charged particles would initiate the formation of a spark along its trail. The current pulse generated in the etched wires created a mechanical wave in a magnetostrictive wire (called a "pickup wand") wound over the copper strips. The travel time for this acoustic pulse along the wand indicated the point on the chamber circumference where the activated etched strip terminated. After pulsing the spark gaps were cleared of charge by application of a 350 V clearing pulse. A 10 V potential was applied at other times to keep the MSSCs clear of ions.

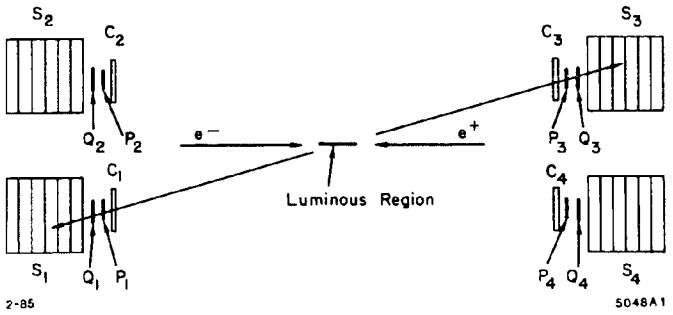

Fig. 2.8 The Crystal Ball small-angle luminosity monitor. Four arms are used to look for Bhabha events at angles near 4° to the beam. C_i, P_i, and Q_i are scintillation counters and the S_i are shower counters ($i = 1, \ldots, 4$).

2.3.4 *Luminosity Monitor*

The Crystal Ball detector includes a small-angle luminosity monitor allowing the measurement of beam luminosity and allowing optimization of beam orbits via position asymmetries of Bhabha events.[42] The luminosity monitor consists of four arms, each containing three scintillation counters and one shower counter. (See Fig. 2.8.) The scintillation counters P_i and C_i in each arm are used to detect Bhabha events; counter Q_i is used for diagnostics. Shower counter S_i makes an energy measurement of the incident electron or positron. The aperture-defining counters P_i are at an angle of 4.25° to the beam and each subtends 4.2×10^{-4} steradians.

A Bhabha event (or $e^+e^- \to \gamma\gamma$ event) is recorded when the counters P_i and S_i in one arm record hits, the counters C_j and S_j in the opposing arm also record hits, and the energy deposited in each shower counter is greater than $E_{\text{beam}}/2$. The counter P_i defines the aperture of the monitor; opposing counter C_j, which is larger in area, allows for beam spread. An off-center beam orbit can be observed by inspecting ratios of counter rates between the different arms. This technique

was used to help eliminate erratic orbits during Crystal Ball running.

The Bhabha scattering cross-section has a very strong angular dependence. Neglecting radiative corrections, in the extreme relativistic limit the lowest-order Bhabha scattering differential cross-section is[43]

$$\left.\frac{\partial\sigma}{\partial\Omega}\right|_{\text{Bhabha}} = \frac{\alpha^2}{8E_{\text{beam}}^2}\left[\frac{1+\cos^4(\theta/2)}{\sin^4(\theta/2)} - \frac{2\cos^4(\theta/2)}{\sin^2(\theta/2)} + \frac{1+\cos^2(\theta)}{2}\right]. \qquad [2.3]$$

This yields a counting rate $1.26\,E_{\text{beam}}^2$ for E_{beam} measured in GeV at a luminosity $\mathcal{L} = 10^{30}$ cm^{-2}sec^{-1}. This is around 0.3 Hz at $E_{\text{cm}} = 4.028$ GeV.

The luminosity $\mathcal{L}$ is calculated by dividing the measured rate dN/dt by the cross-section integrated over the aperture of the luminosity monitor. The cross-section of the monitor is derived using a Monte Carlo simulation program which includes radiative corrections.[44] Because of the symmetric construction about the beam axis, the monitor is insensitive to small displacements of the e^+e^- interaction point. The accuracy of measured luminosities is about $\pm 4\%$. Comparison of these small-angle luminosities with large-angle luminosities calculated using Bhabha events in the detector hemispheres agrees to within 3%.[45]

2.4 Detector Electronics and Trigger System

2.4.1 *Data Acquisition Overview*

The electronic signals generated by the detector can be divided into two classes: (1) signals which are appropriate for use in deciding whether or not to record a particular event, and (2) those which are not. The first class includes the prompt signals from the phototube outputs, and readouts from the MWPCs; the second class includes the MSSCs, which have a long dead time after being read out, and the outputs from other systems such as the luminosity monitor.

Signals from both categories are presented to digitization electronics; however, they are only recorded by the online computer system when a trigger condition has been satisfied (see below). These signals are stored in analog form

in *integrate and hold* capacitors while the trigger logic is deciding if the event should be recorded; if so, the capacitors are isolated via FET switches until they can be individually and serially digitized by a single analog-to-digital converter (ADC). Otherwise, with no trigger condition satisfied, the signals are allowed to drain from the capacitors in time to clear the system for the next possible event. Signals from the first class are also presented to the hardware trigger electronics. Here the phototube outputs are summed in groups of nine by analog circuitry and presented to the trigger system; each group of nine modules corresponds to the nine crystals in a minor triangle (see the description above of Crystal Ball geometry). Thus the trigger logic never inspects the energy in a single crystal, but only the total energy in minor triangles or larger geometric sums.

Two-channel Energy Range

In the integrate-and-hold electronics, each photomultiplier tube output is actually sent to two channels (low- and high-energy). This is done to increase the dynamic range available from the 13-bit ADC that is used to digitize the phototube pulse heights. There are two integrate and hold modules per phototube, one for each energy channel, with the high-energy channel preceded by a resistive divider circuit which attenuates the signal by a factor of 21.

2.4.2 *Trigger Generation*

As mentioned above, the decision to record a particular event, the generation of a trigger, is made in hardware by part of the online electronics, using signals from the photomultiplier tubes and the charged tracking system. For redundancy (to increase the acceptance of the system for hadronic events), there are two independent subsystems in the trigger electronics: one is the *tower* trigger, the other the *fast* trigger.[46] The tower trigger is a TTL* system while the fast trigger

* Transistor-Transistor-Logic

is assembled from individual NIM† logic modules.[47] Both trigger systems form energy sums of the crystals in each group of nine (each minor triangle) for signals from the hemispheres and the multiwire proportional chambers. A charged track trigger is generated if there is a coincidence of hits in both layers of the MWPC.

Trigger Requirements

Triggers were formed in this analysis whenever any of the following conditions occurred:

1. Total observed energy in the hemispheres > 1150 MeV;
2. More than 60 MeV was observed in two diametrically opposite major triangles;
3. Any two major triangles had at least 140 MeV each and a charged track was observed in the MWPC's;
4. The upper hemisphere and the lower hemisphere both had energies of at least 140 MeV and the sum of their energies was > 770 MeV

In these energy sums the tunnel modules are omitted since they tend to be noisy being close to the beampipe entry and exit ports. The total trigger rate was about 3 Hz with $\approx$ 10% deadtime (caused by the spark chamber recovery time of 40 msec).

2.5 Calibration

2.5.1 *Introduction*

The NaI(Tl) crystals and the phototubes are assumed to respond linearly to increasingly higher energies of incident photons and electrons;[35] but nevertheless must be calibrated at regular intervals to compensate for drifts in the system

† Nuclear Instrumentation Module.

response over times of a few days to several years. Three procedures are used to calibrate the crystals and electronics:

1. Using the radioisotope ^{137}Cs;
2. Using a Van de Graaff accelerator, producing 340 keV protons incident on a ^{19}F target; and
3. Using Bhabha scattering events ($e^+e^- \rightarrow e^+e^-$) or $e^+e^- \rightarrow \gamma\gamma$ events.

The ^{137}Cs and the Van de Graaff calibrations are done approximately every two weeks; data for Bhabha calibrations are accumulated continuously during run periods.

2.5.2 *Definition of Calibration Constants*

Recall from above that each photomultiplier tube is read by two channels in the electronics. The low-energy channel covers energies in the range zero to 160 MeV, and the high-channel covers the range zero to 3200 MeV. Assuming a linear response for each channel, each crystal will require four calibration constants to convert the ADC counts to energies. These are

$$\begin{aligned} P_i^{\text{high}} &\equiv \text{high-channel ADC pedestal counts,} \\ P_i^{\text{low}} &\equiv \text{low-channel ADC pedestal counts,} \\ R_i &\equiv \text{ratio constant, and} \\ S_i &\equiv \text{slope constant} \end{aligned} \qquad [2.4]$$

where the index i runs over all crystals. The pedestals are the counts seen in the ADC when zero energy is input to the crystals. The slope constant is the slope of the low-channel linear response curve; it is used to determine the low-channel energy E_i^{low} via the relation

$$E_i^{\text{low}} = S_i \times \left(C_i^{\text{low}} - P_i^{\text{low}} \right) \qquad [2.5]$$

where S_i is the low-channel slope and C_i^{low} is the counts in the ADC for the low-channel of the i^{th} crystal. R_i is the ratio of high-channel to low-channel slopes for crystal i; high-channel energies are calculated from

$$E_i^{\text{high}} = R_i \times S_i \times \left(C_i^{\text{high}} - P_i^{\text{high}}\right) \qquad [2.6]$$

where C_i^{high} is the counts in the ADC for the high-channel of the i^{th} crystal. The means for determining these values will be discussed below. For complete details, see Refs. 48 and 49.

2.5.3 *Pedestal Calibration*

In order to save storage space in the online computer system, the digitized data is compressed before writing it to a raw data tape. This procedure omits the ADC counts from crystals with little ($\leq$ 0.5 MeV) energy deposition. However, every 128^{th} event is written uncompressed; this allows determination of the pedestal values for crystals with zero energy by simple averaging of the counts in each crystal over many events.

2.5.4 *Cesium Calibration*

The first step in calibrating the detector is performed with a 0.1 millicurie cesium radioisotope source placed in the center of the hemispheres. This calibration step uses the reaction

$$\begin{aligned} {}^{137}\text{Cs} &\rightarrow \beta^- + {}^{137}\text{Ba}^* \\ &\qquad\qquad \hookrightarrow {}^{137}\text{Ba} + \gamma(0.66\ \text{MeV}) \end{aligned} \qquad [2.7]$$

to produce a 0.66 MeV gamma ray. Calibration data is recorded until several hundred hits are observed in each crystal. The histogram of the energy response for each module is inspected manually, and the approximate position of the

cesium peak is indicated to the online computer algorithm.* Then the low-channel slopes are adjusted for each crystal to yield the fixed 0.66 MeV energy photon line.

2.5.5 *Van de Graaff Calibration*

The Van de Graaff calibration is used to extend the calibrated range of the detector to the several MeV regime. It uses 6.131 MeV photons which are produced via the reaction:

$$\begin{aligned} {}^{19}\mathrm{F} + \mathrm{p} \rightarrow {}^{20}\mathrm{Ne}^{*} \rightarrow {}^{16}\mathrm{O}^{**}(3^{-}) + \alpha \\ \qquad\qquad\qquad\qquad \Big\lfloor\!\!\longrightarrow {}^{16}\mathrm{O}(0^{+}) + \gamma(6.131\ \mathrm{MeV}). \end{aligned} \qquad [2.8]$$

The protons are produced at 340 keV using a Van de Graaff generator and are incident on a fluorine target. Note that it is the second excited state of ^{16}O that is occupied, and which decays via an E3 (electric octupole) transition, with a half-life of 17 psec. The first excited state of ^{16}O at 6.052 MeV has $J^P = 0^+$, as does the ground state, so the $0 \rightarrow 0$ transition is forbidden (the experimental half-life is 50 psec).[50]

Unlike the cesium calibration, the 6.1 MeV photon generally deposits its energy in more than one crystal, making the energy assignment for calibration purposes difficult. To compensate, the initial values for slopes from the ^{137}Cs calibration are adjusted using an iterative procedure. The energy from the neighboring crystals, along with the energy in the crystal being calibrated are summed, using the current values of the constants. The constants of the central crystal (the one being calibrated) are adjusted so that the summed energy is equal to the 6.131 MeV photon energy. Since this introduces a dependence of each crystal's

---

* Human intervention is necessary here to find the approximate peak position because of the broadness of the peak at these low energies ($\sigma_E(E = 0.66\ \mathrm{MeV}) \approx 0.3$ MeV) and the large background involved.

constants on its neighbors, an iterative procedure is used. Three passes through the calibration procedure are sufficient for convergence of the constants.

2.5.6 *Bhabha Calibration and Position Correction*

The ^{137}Cs and the Van de Graaff calibrations check the detector response only at low energies. In order to get final slope constants, Bhabha events are used.* An iterative procedure similar to that for the Van de Graaff calibration is used, since the showers again occupy several crystals. A three-pass iteration is sufficient.

A final correction is made to compensate for electromagnetic shower leakage from the central crystal (where the particle impacted) into the wrapping material and neighboring crystals. An impact point near a vertex will deposit less energy into the central crystal, and more into its surroundings, than an impact point near the center. This can be observed by inspecting the ratio of the central crystal's energy to the summed energy. By using a correction factor, determined from extensive Monte Carlo study of lateral shower energy spread *vs.* impact point, a correction for this effect can be made.

Results of the three calibration procedures are shown in Fig. 2.9. Note that the Bhabha calibration is not sufficient to bring the peak of the distribution into agreement with the beam energy: the position correction is necessary. The observed FWHM from the figure after position correction of 4.7% × 1.842 GeV yields a resolution of $\sigma_E/E = 0.027/\sqrt[4]{E}$ which is consistent with the quoted resolution of $0.026/\sqrt[4]{E}$ from Eq. 2.2.

The conversion into physics information of the raw ADC counts and calibration constants that have been stored on the raw data tapes is taken up in the next chapter.

---

* Also events of the type $e^+e^- \rightarrow \gamma\gamma$ which leave two electromagnetic showers at the beam energy.

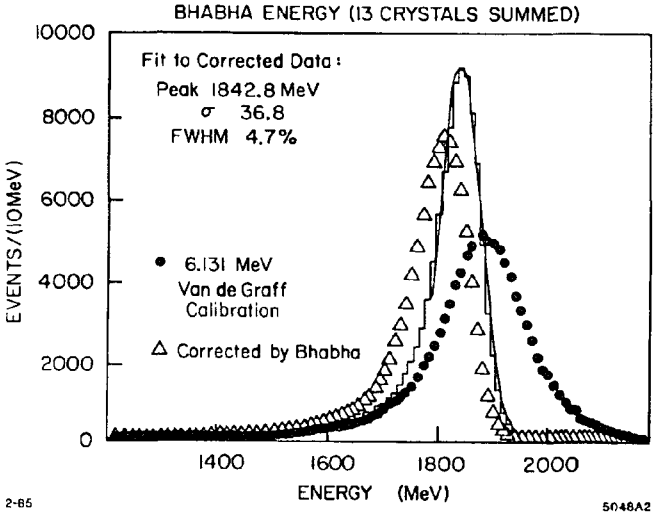

Fig. 2.9 Distribution of energies in Bhabha events at the ψ' resonance (E_{cm} = 3.685 GeV). The two sets of data points are: (•) the energy response using only the preliminary Van de Graaff calibration; and (△) the energy response using the initial Bhabha calibration. The histogram is the final energy response using a refined Bhabha calibration technique which compensates for cases where the particle entered the central crystal near a vertex rather than near the center, thus sharing a large part of its energy with its neighbors. The solid line is a fit to the histogram, using an empirical lineshape function (essentially a Gaussian).

Chapter 3

Initial Data Analysis

3.1 Introduction

This chapter describes the initial stages of the analysis of e^+e^- events at $E_{\rm cm}$ = 4.028 GeV. Properties of the data samples used in the analysis are described; the process of converting raw data obtained from the detector into physics information, *i.e.*, into energies, directions, *etc.*, is explained; and hadron selection is discussed.

Data samples from several running periods are used in this analysis. Calibration of the detector and electronics chain is discussed in Chapter 2, so the description of the raw data processing begins with the 'raw-data-to-physics-numbers', or *production*, process. Then follows a discussion of the hadron selection procedure describing the algorithm used to remove non-hadronic events from the data samples. This includes the removal of cosmic-ray, beam gas, and QED events.

3.2 Description of Data Samples

The D^* physics analysis was performed with data taken at SPEAR during two time periods: April 1979 and November 1979. SPEAR operated at $E_{\rm beam}$ = 2.014 GeV ($E_{\rm cm}$ = 4.028 GeV). To verify that the machine was running on the resonance peak, a scan across the 4.028 GeV region was conducted, running from $E_{\rm beam}$ = 2.011 GeV to 2.017 GeV, followed by extended running at $E_{\rm beam}$ =

2.014 GeV. The total integrated luminosity of the two running periods is 125 nb^{-1} and 759 nb^{-1}, respectively, for a total of 884 nb^{-1} at $E_{beam} = 2.014$ GeV.

Data from other running periods and energies have been used to check the inclusive photon and π^0 energy analysis (described in Chapters 4 and 5). A sample of hadronic events below the ψ' resonance at $E_{cm} = 3.670$ GeV is used to approximate the non-open charm background spectrum at $E_{cm} = 4.028$ GeV. (See Chapter 5.) A sample on the ψ' resonance ($E_{cm} = 3.685$ GeV) is used to investigate the photon energy resolution and detector calibration for photons with energies in the 100 to 200 MeV range. A sample at the ψ'' resonance ($E_{cm} = 3.772$ GeV) is used to check the performance of the inclusive analysis in a region with simpler physics than that at the 4.028 GeV resonance. Only charm meson pairs of the types $D\overline{D}$ are produced at $E_{cm} = 3.772$ GeV; meson pairs of the type $D^*\overline{D} + \overline{D}^*D$ and $D^*\overline{D}^*$ are kinematically forbidden.

3.3 Conversion to Physics Information

3.3.1 *Introduction*

The conversion algorithm that takes raw data written on magnetic tape from the detector, henceforward referred to as 'production', consists of five steps.* These are:

1. The 'Energy' step. The crystal energies are calculated from analog-to-digital convertor (ADC) counts and calibration constants.
2. The 'Connected Region' step. Sets of contiguous crystals with significant energy deposition are searched for and recorded. These sets are called

* After the Crystal Ball detector was moved to DESY in Hamburg, West Germany, hardware for a muon time-of-flight system was added which covers 50% of the upper 2π of the solid angle of the detector. This system allows rejection of about 80% of the cosmic-ray muon background, and requires a sixth step in the production algorithm. This system was not installed during SPEAR running, so it is not described here any further. See Refs. 52, 53, and 54 for details.

connected regions.

3. The 'Bumps' step. For each connected region found in Step 2, local maxima in energy deposition are located and assigned to *tracks* (paths of particles traversing the detector). A preliminary estimate of the energy associated with the track is made.

4. The 'Charged Tracks' step. Tracks are reconstructed from spark and wire chamber information alone, and compared with the tracks found in Step 3, to see if any of those tracks can be assigned a charged hypothesis.

5. The 'ESORT' step. A second, more refined, determination of track energies and directions is made, which is more accurate than that done in Step 3.

For this analysis, all production was done at the SLAC computation center on IBM model 3081K and 3033D computers running the VM/SP operating system. The physics analysis described in the following chapters was done on the same system or on the Princeton/Crystal Ball VAX 11/780 system located at SLAC.

3.3.2 *The 'Energy' Step*

Recall that each crystal in the detector is assigned an energy using the relation

$$E_{\text{crystal}} = \begin{cases} (C_{high} - P_{high}) \times R \times S & \text{if } C_{high} \geq 350 \text{ or } C_{low} \geq 7000 \\ (C_{low} - P_{low}) \times S & \text{otherwise.} \end{cases} \quad [3.1]$$

The calibration constants were described in Chapter 2.

3.3.3 *The 'Connected Region' Step*

The crystals are partitioned into one or more sets by finding groups of contiguous crystals, each with an energy deposition of at least 10 MeV each. Such a set is called a connected region.

3.3.4 *The 'Bumps' or Energy Assignment Step*

Track Search

Each connected region is examined to find local maxima in the spatial distribution of energies. Each crystal which contains such a maximum (called a *bump*) is assumed to contain the point where a particle from the interaction entered the sodium iodide (limitations of this assumption are discussed below). The presumed path of this particle from the e^+e^- interaction to the place where it exits the detector or comes to rest is called a track. The algorithm for locating tracks and assigning energies to the tracks follows below; it was developed by empirical inspection of the energy depositions of Bhabha events.

Energy Assignment Algorithm

1. Mark all crystals in the connected region under consideration as 'free', *i.e.*, as not yet associated with any given bump.*
2. From the set of free (*i.e.*, unmarked) crystals remaining in the connected region, find the crystal in the connected region with the maximum energy deposition and mark this crystal as a *bump module.*
3. Mark the three nearest neighbors of this crystal as associated with this bump module.
4. Define a preliminary energy E_{bump} for this track as the sum of the energies of the bump module and its three neighbors as found above. This is called the 'sum of four' energy, denoted by E_4. See Fig. 3.1. Also define the direction of this track to be given by the direction cosines of the center of the bump module.

---

* Throughout this description the term 'bump' is synonymous with 'track'. The term 'bump module' refers to the crystal which contains the maximum energy deposition of any of the crystals associated with a track in the connected region under study.

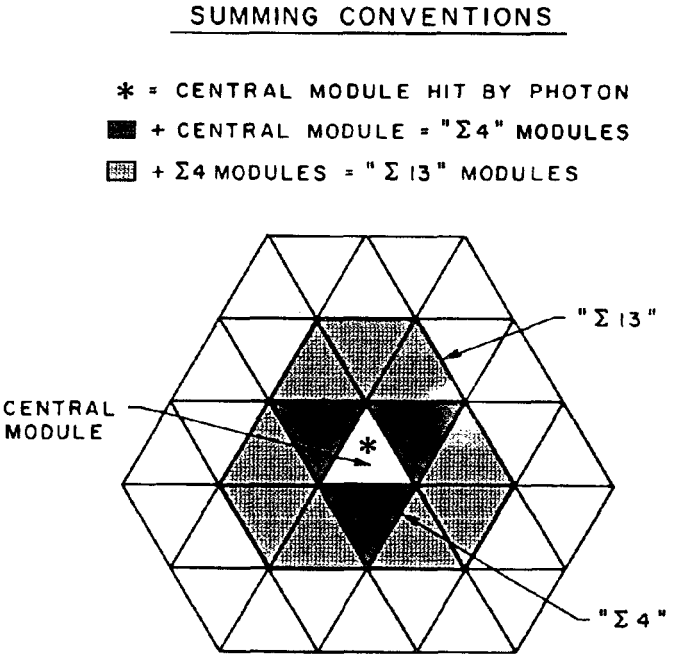

Fig. 3.1 Summing conventions used in forming the geometrical energy sums E_4 and E_{13}. The 13 crystals summed are outlined in the heavier border.

5. Check all remaining unmarked crystals in this connected region, and for each crystal compute the angle θ between the center of the bump module and the center of the crystal under consideration. Mark this crystal as associated with the current track if its energy and the angle θ satisfy the *discriminator function*:

$$\theta \leq 15^\circ, \qquad [3.2]$$

or

$$E_{\text{crystal}} < E_{\text{bump}} \times 0.72e^{-9.4(1-\cos\theta)} \quad \text{and} \quad 15^\circ < \theta < 45^\circ. \qquad [3.3]$$

6. Repeat this process, starting at item 2 above, until all crystals in this connected region have been marked as bump modules or as associated with a track.

Limitations

It is not known beforehand, of course, whether a given shower in the crystals is electromagnetic or hadronic in nature, nor whether it is caused by one isolated particle traversing that region of the detector or by the deposition of two or more overlapping showers. Electromagnetic showers have a fairly predictable lateral energy spread; they are not subject to frequent, large fluctuations in the Crystal Ball detector because of its relatively deep 16 radiation length thickness. On the other hand, hadronic showers tend to be much less predictable, since the detector is slightly less than one nuclear interaction length thick (about 41 cm). Very often fluctuations in hadronic showers will be erroneously identified as tracks in their own right; such mis-identified fluctuations are called *split-offs*. Electromagnetic showers may have split-offs too, but these are less common, and usually only occur for low-energy showers of $\lesssim$ 70 MeV. Due to the fluctuations, it is also possible, especially for hadronic showers, that the crystal containing the impact point may have less energy deposited in it than a neighboring crystal; this of course also degrades the resolution of the detector. The inability to distinguish between hadronic and electromagnetic energy deposition, and the mistaken identification of split-offs, are the limiting factors in the detector's ability to resolve neighboring tracks. The discriminator function (outlined above) is designed to maximize the chance of pairing crystals with tracks in an environment having a typical mix of the two types of showers.

3.3.5 *The 'Charged Tracks' Step*

At this point in the production analysis an attempt is made to construct more tracks from the information in the magnetostrictive spark chambers and

proportional wire chambers, without regard to tracks previously located in the crystals. The chambers are searched for rows of sparks which lie close to straight lines. Each row of sparks is fitted to a straight line hypothesis (recall the Crystal Ball is a non-magnetic detector: there is no curvature) and is identified as the path of a charged particle. These paths are defined as 'Interaction Region' tracks, or *IR tracks*. If at least one IR track is found, a z-vertex* position for the interaction is calculated using an average of the individual z-vertices of each IR track. The x and y coordinates of the vertex are set to zero, since the bunch size is small in these directions compared to the bunch length (see Chapter 2). Figure 3.2 shows the distribution of z-vertex values for the events studied in this analysis. Events with no IR tracks are assigned a z-vertex position of zero.

If an IR track points closely to a previously found track in the crystals, then the two tracks are identified as one. This single track is defined to be charged and the direction cosines as found by the chambers are used as the direction of the track rather than the direction cosines from the crystals.

After locating all possible IR tracks, the tracks found only in the crystals are inspected to see if they may be the trajectories of charged particles which were not found as IR tracks because of inefficiencies in the charged-tracking system. The number of sparks in an angular "tagging window" around the portion of the track traversing the chambers is inspected. If enough sparks are found, this track is defined as 'tagged as charged' rather than 'tracked as charged'. Its direction cosines are calculated from the energy deposition in the crystals, not from chamber information.

The charged tracking algorithm misidentifies tracks because of inefficiencies

---

* The vertex referred to is the primary vertex of the event, *i.e.*, the location of the e^+e^- interaction point expressed in the SPEAR coordinate system near the center of the detector. Events may have more than one vertex; for instance, a K_L^0 that travels several centimeters away from the interaction point and then decays may be found as a second vertex by the production algorithm.

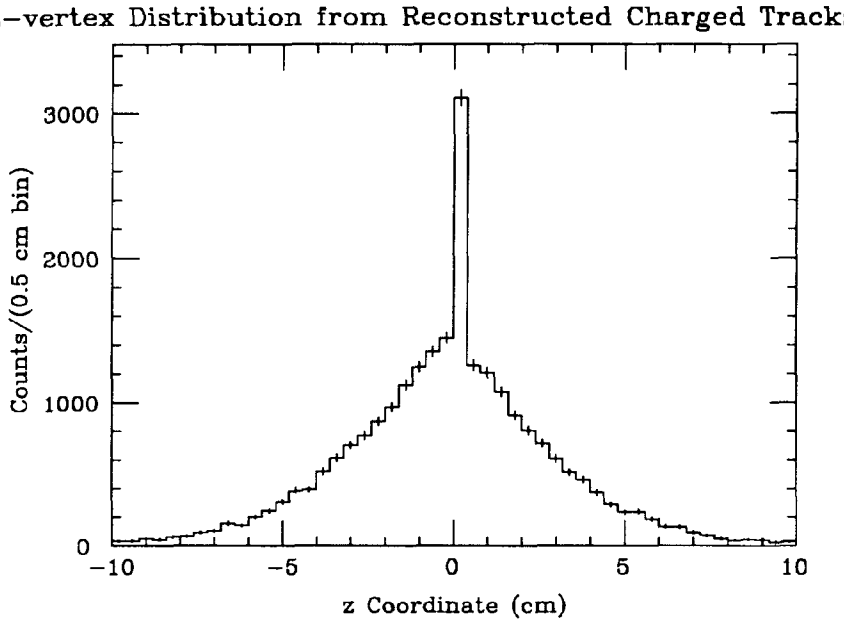

Fig. 3.2 The distribution of z-vertex positions of the 24 681 hadronic events with E_{cm} = 4.028 GeV used in this analysis. Events where no charged tracks were reconstructed are assigned a z-vertex value of zero. This produces the one-bin wide peak at zero.

in the system. An IR track is sometimes found in the chambers which does not point to an energy shower in the crystals; this usually indicates that an incorrect z-vertex has been constructed causing errors in the calculation of direction cosines of the charged tracks. Such IR tracks are assigned zero energy. These zero-energy IR tracks are an indication of *undertagging* (when a charged track in the crystals is identified as neutral rather than charged).

The opposite problem of *overtagging* can occur when extra sparks from noise or strange particle decays create secondary vertices. Incorrect combinatorics in matching sparks can also result in overtagging.

Undertagging is readily observed in the energy spectrum of tracks identified as neutrals before more restrictive cuts are applied (see Chapter 4). Minimum-

ionizing charged particles have a most probable energy loss at a particular value determined by the detector's geometry and composition. For the Crystal Ball, the most probable energy loss for a minimum-ionizing particle entering the crystals at normal incidence is

$$\begin{aligned} E_{\text{Min-I}} &= \overline{\Delta E} \times \rho_{\text{NaI}} \times t \\ &= 197 \text{ MeV}. \end{aligned} \qquad [3.4]$$

where $\overline{\Delta E}$ is the energy loss per g/cm^2 for minimum ionizing protons and pions, ρ_{NaI} is the density of sodium-iodide, and t is the length of a crystal. The values

$$\begin{aligned} \overline{\Delta E} &= 1.32 \ \frac{\text{MeV}}{\text{g/cm}^2}, \\ \rho_{\text{NaI}} &= 3.67 \text{ g/cm}^3, \text{ and} \\ t &= 40.6 \text{ cm (16 in)} \end{aligned}$$

have been used.[57] In Fig. 3.3, an obvious peak is indeed observed near this energy.

3.3.6 *The 'ESORT' Step*

Two energy assignments and a more refined calculation of direction cosines for each track is made in this step.[51] Two energies are calculated to replace the sum of four energy, E_4, which has been used up to this point. The first is the 'sum of 13' energy, denoted E_{13}, which is the sum of the crystal energies of the bump module and its twelve neighbors (unless the bump module lies adjacent to a vertex of the icosahedral geometry of the detector, in which case there are only 11 neighboring crystals). See Fig. 3.1. This energy sum generally has a double-counting of some crystal energies for tracks which lie near each other in angles. The second energy sum E_{sort} attempts to allocate energy in a single crystal between two or more nearby tracks using pre-determined shower distribution functions. These shower functions are generated using the electromagnetic

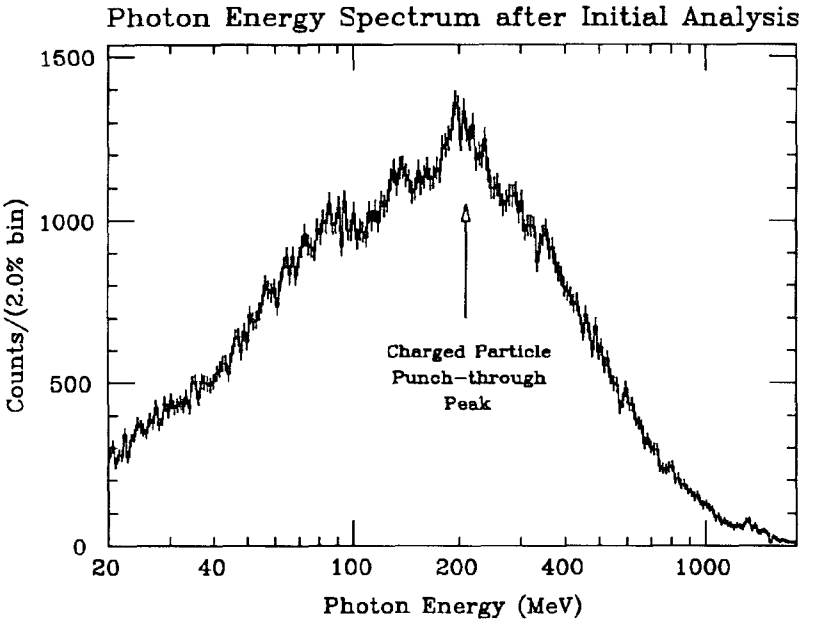

Fig. 3.3 The track energy distribution of tracks tagged as "neutral" after hadron selection, showing an obvious charged-particle punch-through peak. The position of the peak is near 197 MeV, the calculated value of the most probable energy loss for a minimum-ionizing particle in 16 inches of sodium-iodide.

shower Monte Carlo program EGS.* [58–59]

The direction cosines for each neutral track are recalculated during the ESORT step. The bump module is divided into 16 submodules of triangular cross-section and each submodule is considered in succession. For each module the observed energy distribution is compared to a pre-determined energy distribution for an electromagnetically showering particle of the same energy, using the center of the submodule as the entry point. The submodule yielding the best agreement with the predicted distribution is determined, and the direction cosines of its center are used as the direction cosines of the track.

---

* An acronym for the Electron-Gamma Shower code.

3.4 Hadron Selection

3.4.1 *Event Classification*

In the $E_{\rm cm}$ = 4.028 GeV energy range at SPEAR, only some 2%* of all recorded events are assumed to proceed through $e^+e^- \rightarrow q\bar{q} \rightarrow$ hadrons, where q is a member of the quark family: $q = u$, d, s, or c. Most other events are one of the following: beam gas, cosmic-ray, or QED events. Beam gas events occur when an electron or positron in the beam interacts with a residual gas molecule left in the beampipe after its volume has been evacuated. Such events are characterized by an asymmetry in the energy deposition in the detector. Cosmic-ray events occur when naturally-occurring background radiation enters the detector from outside the detector's volume and triggers the electronics. These events are often muons produced in the upper atmosphere. There are several categories of QED events. These are all results of electromagnetic interactions between the electron and positron. Events of the type $e^+e^- \rightarrow e^+e^-$ are called Bhabhas and are useful in calibrating the energy response of the detector (see Chapter 2); other QED events include radiative Bhabhas ($e^+e^- \rightarrow \gamma e^+e^-$), and events of the type $e^+e^- \rightarrow \gamma\gamma(\gamma)$. Two-photon events occur when $e^+e^- \rightarrow \gamma\gamma e^+e^-$ with the $\gamma\gamma \rightarrow$ a ($J = 0$ or 2, $C = +$) state. There are contributions from $e^+e^- \rightarrow \mu^+\mu^-$ and from tau lepton events, where $e^+e^- \rightarrow \tau^+\tau^-$. These latter events are somewhat difficult to remove since the branching fraction $\tau \rightarrow$ hadrons is large: nearly 67%.[57] These non-hadronic events are generally characterized by either large momentum asymmetries, *e.g.*, beam gas and cosmic rays, or by low multiplicities (QED events except for hadronic τ decays).

* About 3% of the input events will pass the hadron selection cuts but roughly 1/3 of these are residual contamination from non-hadronic events, especially beam gas.

3.4.2 *Hadron Selection Cuts*

The cuts used to eliminate the non-hadronic background are discussed below: first there is a brief listing of the cuts and a summary of their effects; a more specific discussion of each with figures follows. For more details, see Ref. 55.

Brief List of Cuts

1. Showering QED cut. Removes events with few tracks and large energy depositions.
2. Multiplicity cut. Removes low-multiplicity events; intended to catch QED events that pass the cut above.
3. Low $p^2_{T_z}$ cut. Removes beam gas events.
4. Low $p^2_{T_{\rm jet}}$ cut. Removes cosmic-ray events and QED events of the type $e^+e^- \to \mu^+\mu^-$.
5. Forward-backward asymmetry cut. Removes residual beam gas still remaining after the previous cuts.

Table 3.1 shows the percentages of events remaining after each cut for a portion of the data at $E_{\rm cm} = 4.028$ GeV. The hadron selection efficiency for true hadronic events is around 98%. This has been investigated using a constant matrix element[60] Monte Carlo event generator with the Crystal Ball detector simulation algorithm. From a sample of 12 500 generated events of the type $e^+e^- \to D^{*0}\overline{D}^{*0}$, followed by $D^{*0} \to \pi^0 D^0$ or $D^{*0} \to \gamma D^0$ using a branching ratio ${\rm BR}(D^{*0} \to \pi^0 D^0) = 55\%$, it is found that 12 429 events pass the selection criteria. Thus the efficiency for $D^{*0}\overline{D}^{*0}$ and the charge conjugate events is $99.4 \pm 0.1^{+0.6}_{-2.0}\%$ (first error is statistical, second is systematic). Selection efficiencies for $e^+e^- \to (D^{*0}\overline{D}^0 + D^0\overline{D}^{*0})$ and $e^+e^- \to D^0\overline{D}^0$ and charge conjugates are about 1% smaller because of the slightly lower multiplicities.[56] A nominal value for the hadron selection efficiency for all D-meson events is

$$\epsilon_{\rm hadron} = 98 \pm 2\%. \qquad [3.5]$$

Hadron Selection Performance on Triggers from Colliding-Beam and Monte Carlo Data				
	Colliding-Beam Data		Monte Carlo Data	
Cut Performed	Triggers Left	%	Triggers Left	%
Before Selection	769 957	100.0	13 975	100.0
QED	439 433	57.1	13 971	100.0
Multiplicity	53 562	7.0	13 963	99.9
Transverse z-axiz Momentum	26 841	3.5	13 887	99.4
Transverse Jet-axis Momentum	25 353	3.3	13 880	99.3
Forward-Backward Asymmetry	23 906	3.1	13 788	98.7

Table 3.1 Percentages of triggers remaining after hadron selection. The effects of the cuts are illustrated using (1) triggers from colliding-beam data at $E_{\rm cm}$ = 4.028 GeV, and (2) events generated by Monte Carlo of the type $e^+e^- \rightarrow (D^{*0}\overline{D}^0 + D^0\overline{D}^{*0})$. As seen, the hadronic cuts are $\gtrsim$ 98% efficient for hadronic events.

3.4.3 *The Showering QED Cut*

This first cut is intended to remove QED events with a large observed energy fraction f_E and few tracks in the detector such as (radiative) Bhabha events. The observed energy fraction is

$$f_E = \sum_{\substack{\text{over} \\ \text{crystals}}} \frac{E_i}{E_{\rm cm}} \qquad [3.6]$$

where E_i is the energy measured in crystal i. Define $N_{\rm cr}$ to be the number of connected regions found in the event, $N_{\rm tracks}$ to be the number of tracks found, and order the tracks from 1 to $N_{\rm tracks}$ in order of decreasing energy

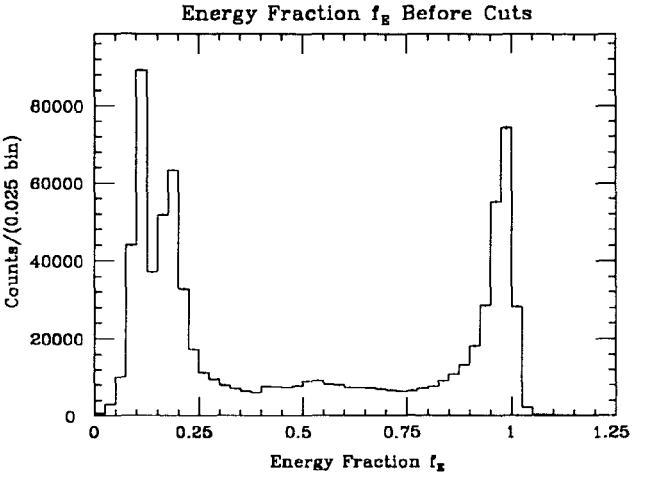

Fig. 3.4 The distribution of energy fraction f_E for all events before hadron selection. The energy fraction f_E for an event is the ratio of the total energy observed in the detector and the total energy available, $E_{\rm cm}$. The enhancement at $f_E < 0.25$ is largely due to beam gas and two-photon physics with low transverse momentum to the beam direction; the double-peak structure is an artifact of the trigger thresholds. The large enhancement at $f_E > 0.75$ is from QED events that deposit most of the available energy in electromagnetic showers.

$E_1^{\rm track}, E_2^{\rm track}, \ldots, E_{N_{\rm tracks}}^{\rm track}$. Then this event is rejected if

$$N_{\rm tracks} > 2 \quad \text{and} \quad \frac{E_2^{\rm track}}{E_{\rm beam}} > 0.5, \qquad [3.7]$$

or if

$$N_{\rm cr} < 4 \quad \text{and} \quad \frac{E_1^{\rm track}}{E_{\rm beam}} > 0.75. \qquad [3.8]$$

This cut, in combination with the low multiplicity cut described next, is estimated to remove $\gtrsim 99\%$ of all showering QED events. The effects of the hadronic cuts can be seen in the changes of the neutral energy fraction distribution as they are applied in sequence. The distribution of f_E before any hadronic cuts is shown in Fig. 3.4; the spectrum after application of first QED cut is shown in Fig. 3.5. Note the removal of the peak at large f_E—Bhabha events typically deposit most of the available energy in the detector.

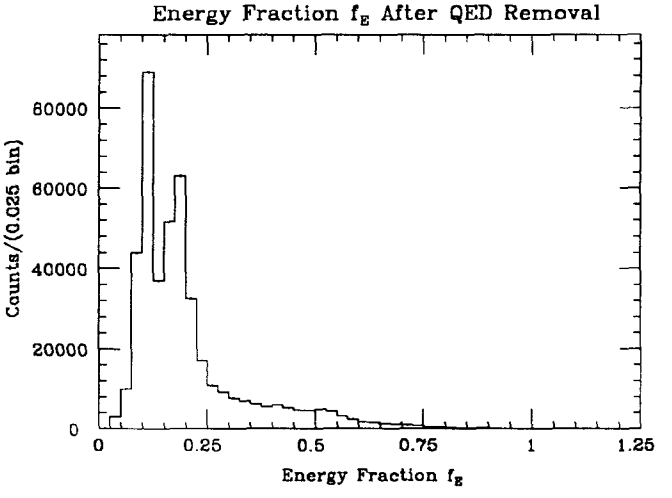

Fig. 3.5 The distribution of energy fraction f_E after the first attempt at removing QED events. Events with large energy fractions and low multiplicities have been removed.

3.4.4 *Low Multiplicity Cut*

This is a secondary QED cut designed to remove QED events with one radiated photon observed in the detector. The event is removed if $N_{\rm cr} < 3$ or if there are no charged tracks found and $f_E < 0.35$. The effect is shown in Fig. 3.6.

3.4.5 *Low $p_{T_z}^2$ Cut*

This cut is designed to reject beam gas events which are usually highly non-isotropic in energy deposition in the detector. Define a vector asymmetry measurement $\mathbf{A}_{\rm sym}$ by

$$\mathbf{A}_{\rm sym} \equiv \frac{\sum\limits_{\substack{\text{over}\\ \text{crystals}}} \mathbf{E}_i}{\sum\limits_{\substack{\text{over}\\ \text{crystals}}} E_i}, \qquad [3.9]$$

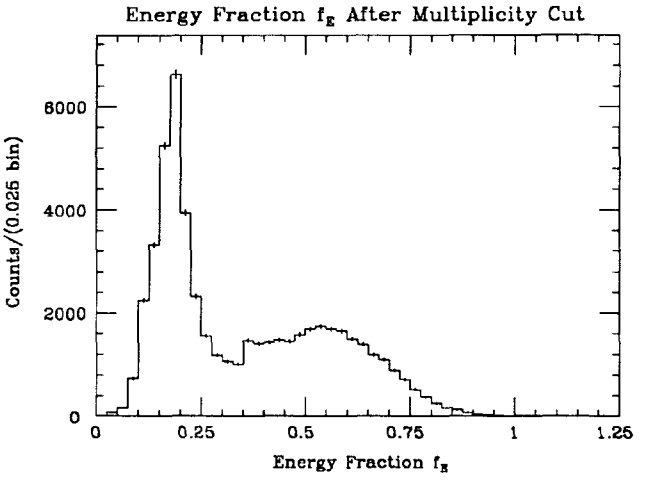

Fig. 3.6 The distribution of energy fraction f_E after the second QED cut. Low multiplicity events or neutral events with low energy fraction have been subtracted.

where $\mathbf{E}_i \equiv E_i\,\hat{\mathbf{n}}_i$, $\hat{\mathbf{n}}_i$ being a unit vector pointing from the origin to the centroid of crystal i, and $p_{T_z}^2$ the transverse momentum to the z-axis defined by

$$p_{T_z}^2 \equiv \sum_{\substack{\text{over}\\ \text{crystals}}} p_{T_z}^2(i) \qquad [3.10]$$

where $p_{T_z}(i) = |(\mathbf{E}_i \times \hat{\mathbf{z}}) \times \hat{\mathbf{z}}|$. Then all events are removed which satisfy

$$|\mathbf{A}_{\rm sym}| > c_1(f_E) \times \left(\log(p_{T_z}^2) - c_2(E_{\rm cm})\right). \qquad [3.11]$$

Parameter c_1 is an offset variable and is a function of f_E, and parameter c_2 varies with $E_{\rm cm}$. See Fig. 3.7. This cut, in combination with the forward-backward asymmetry cut described below, removes $\approx 92\%$ of the beam gas contamination; about 10% of the triggers passing all cuts will be residual beam gas.

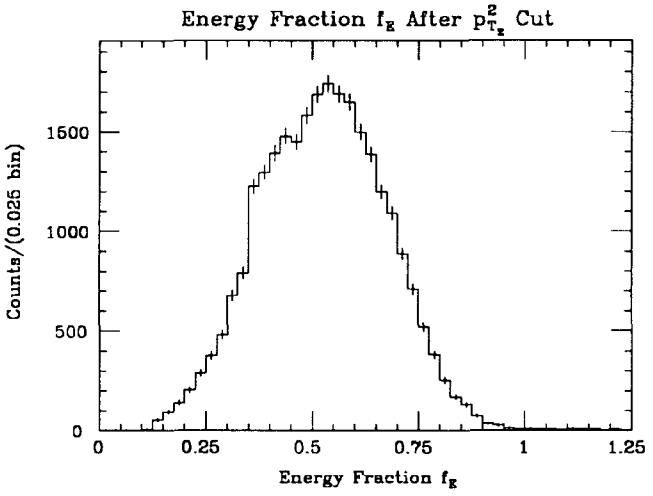

Fig. 3.7 The distribution of energy fraction f_E after beam gas removal. Events where a large asymmetry in energy deposition exists compared to the total $p^2_{T_z}$ have been removed.

3.4.6 *Low* $p^2_{T_{\rm jet}}$ *Cut*

Here events are removed which have a single jet-like structure in energy deposition in the detector such as cosmic rays and $e^+e^- \rightarrow \mu^+\mu^-$. Events are removed if

$$|\mathbf{A}_{\rm sym}| > c_3 \times \left(\log(p^2_{T_{\rm jet}}) - c_4\right), \qquad [3.12]$$

where c_3 and c_4 are constants and the momentum transverse to the jet axis is defined as

$$p^2_{T_{\rm jet}} \equiv \sum_{\substack{\rm over \\ \rm crystals}} \left[\mathbf{E}_i^2 - \left(\mathbf{E}_i \cdot \hat{\mathbf{n}}_{\rm jet}\right)^2\right]. \qquad [3.13]$$

The quantity $\hat{\mathbf{n}}_{\rm jet}$ is the unit vector along the jet axis. See Fig. 3.8. This "jet-axis" cut removes about 93% of the cosmic ray and $e^+e^- \rightarrow \mu^+\mu^-$ backgrounds.

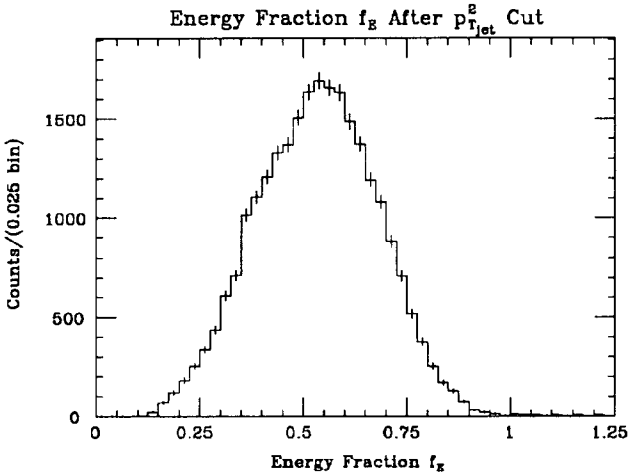

Fig. 3.8 The distribution of energy fraction f_E after cosmic-ray removal. Events with an obvious jet-like structure have been subtracted. Such a structure is common for cosmic-ray events.

3.4.7 *Forward-Backward Asymmetry Cut*

This last cut is intended to remove residual beam gas left after the above cuts. Define a scalar asymmetry measurement by

$$A_{\rm FB} \equiv \frac{|E_{+z} - E_{-z}|}{\sum\limits_{\substack{\text{over}\\ \text{crystals}}} E_i} \qquad [3.14]$$

where E_{+z} is the sum of the energies of all crystals with a positive z-coordinate, and E_{-z} is the sum of the energies of all crystals with a negative z-coordinate. Events with $A_{\rm FB} > 0.8$ are removed. The final f_E spectrum is shown in Fig. 3.9; note that in comparison to Fig. 3.4, only the region around $f_E = 1/2$ remains.

3.4.8 *Hadron Selection Performance*

The hadron selection cuts have been based upon studies done with separated-beam running. The result of these cuts, as was seen in Table 3.1, is to remove

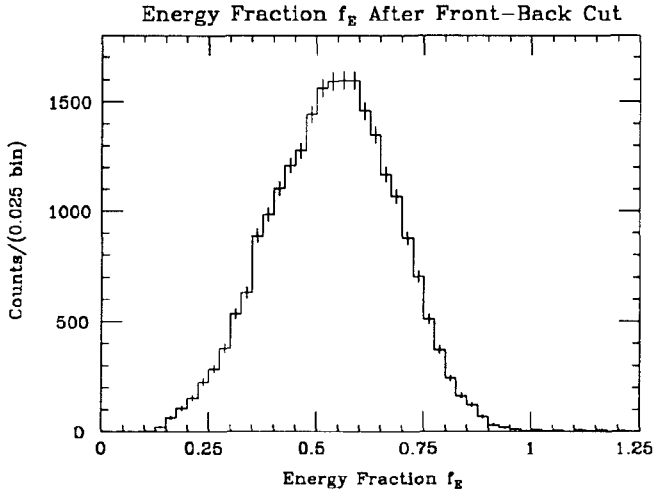

Fig. 3.9 The distribution of energy fraction f_E after the secondary beam gas cut. Events in this sample have passed all hadron selection criteria.

nearly 97% of the original triggers. Of the remaining 3%, it has been estimated from separated-beam running[55] that $\gtrsim$ 90% of the original beam gas contamination has been removed and about 50% of the $e^+e^- \to \tau^+\tau^-$ events are removed. It is estimated that of the events passing all cuts some 3% are two-photon events and about 5% are $\tau^+\tau^-$ events.

Chapter 4

Inclusive Measurement of D^{*0} Spectra

4.1 Introduction

This chapter discusses the determination of inclusive spectra at $E_{\rm cm} = 3.670$, 3.772, and 4.028 GeV. In particular the process of finding the inclusive photon and π^0 energy spectra and angular distributions for D^* production and decay is described. The method for selecting photons after production of the data and two methods of extracting π^0 spectra are discussed. These spectra then serve as the data from which the desired physical parameters can be constrained, as discussed in Chapter 5.

4.2 Inclusive Analysis: Photon Energy Spectra

4.2.1 *Description of Final Analysis Criteria*

A more refined selection of photon candidates than that provided by the production analysis is necessary before generating inclusive energy spectra for measurement of branching ratios and masses. The known sources of imprecision must be reduced: in particular, tracks with poor energy resolution and charged particles which are mistakenly counted as neutral. To this end, the reconstructed tracks obtained from the production analysis for events having passed the hadron

Photon Selection Criteria	
Parameter	Requirement
Particle type as identified by production algorithm	Photon
$\lvert\cos(\theta_{\text{track-beam}})\rvert$	≤ 0.920
Shower lateral energy spread	$0.485 < E_1/E_4 < 0.975$ $0.750 < E_4/E_{13} < 0.995$

Table 4.1 Criteria used to select neutral showering tracks (photons) after production analysis. Tracks passing these cuts are used in generating photon and π^0 inclusive spectra.

selection are inspected. Three further criteria are checked for each track before inclusion in the analysis as a photon:

1. The track has been determined to be neutral by the standard production algorithm (as discussed in Chapter 3).
2. The angle between the track and the beam (z-axis) is greater than 23°.
3. A showering-particle pattern cut on the lateral energy spread of the electromagnetic shower is imposed. This improves discrimination against tracks produced by minimum-ionizing charged particles, improves rejection of low-energy split-offs from higher-energy showers, and rejection of showers produced by hadronic interactions.

These photon selection criteria are summarized in Table 4.1. The need for Cut 1 is obvious; the best determination of the relative probability that a track is charged is done during the production analysis. Cut 2, the angle-to-the-beam requirement, avoids problems with the poorer energy resolution and track reconstruction when a photon encounters the tunnel modules or the endcap modules. Cut 3 is most important in eliminating charged particle punch-through; it is

discussed at length in the next section.

4.2.2 *Lateral Energy Spread Pattern Cuts*

The values used in the pattern cuts were selected by comparing distributions of ratios of the geometrical energy sums E_1, E_4, and E_{13}* of neutral (with $8 \pm 3\%$ charged contamination) and IR track† charged tracks (with $\lesssim 5\%$ neutral contamination) using data at E_{cm}=4.028 GeV. See Figs. 4.1 and 4.2. The values for the cut parameters were chosen to minimize acceptance of charged tracks but without serious loss in photon efficiency; this set of cuts is considered "soft", *i.e.*, less restrictive, compared to other Crystal Ball analyses.

The inclusive photon energy spectra before and after each cut are shown in Fig. 4.3(a–d) (plot (d) is also shown in Fig. 4.4 on a larger scale). In particular note that the minimum-ionizing charged particle peak near 200 MeV has been removed by the pattern cuts; 200 MeV is the characteristic energy loss for a minimum-ionizing particle in 16 inches of sodium iodide.* Photons passing all cuts are used to reconstruct the π^0 energy spectrum and angular distributions as well. This will be discussed further in later sections.

---

* E_1 is the energy in the central module of the shower; E_4 and E_{13} were defined in Chapter 3.

† IR track: A charged track found in the spark chambers projecting from the interaction region; see Chapter 3.

* The most probable energy loss for minimum-ionizing protons and pions in 16 inches of sodium iodide is:[57]

$$\begin{aligned} \Delta E_{\text{Min-I}} &= \overline{\Delta E} \times \rho \times l \\ &= \frac{1.32 \text{ MeV}}{\text{g-cm}^2} \times \frac{3.67 \text{ g}}{\text{cm}^3} \times 41 \text{ cm} \\ &= 199 \text{ MeV}. \end{aligned} \qquad [4.1]$$

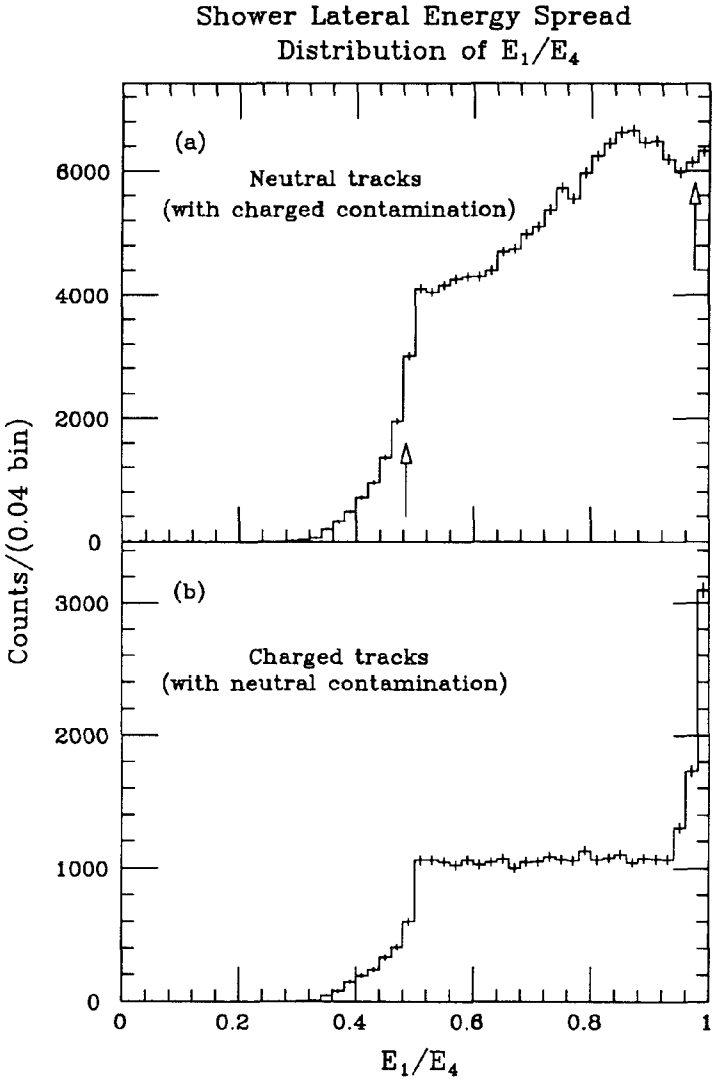

Fig. 4.1 Distribution of E_1/E_4, one measure of the lateral energy spread of a shower. (a) The distribution for tracks determined to be neutral by the production algorithm, including misidentified charged track contamination. (b) The distribution for tracks determined to be charged by the production algorithm, including contamination from misidentified neutral tracks. The arrows on (a) indicate the upper and lower limits allowed for tracks used as photons. The discontinuity at $E_1/E_4 = 0.5$ is an artifact of the definition of the geometric energy sums for showers populating two crystals only.

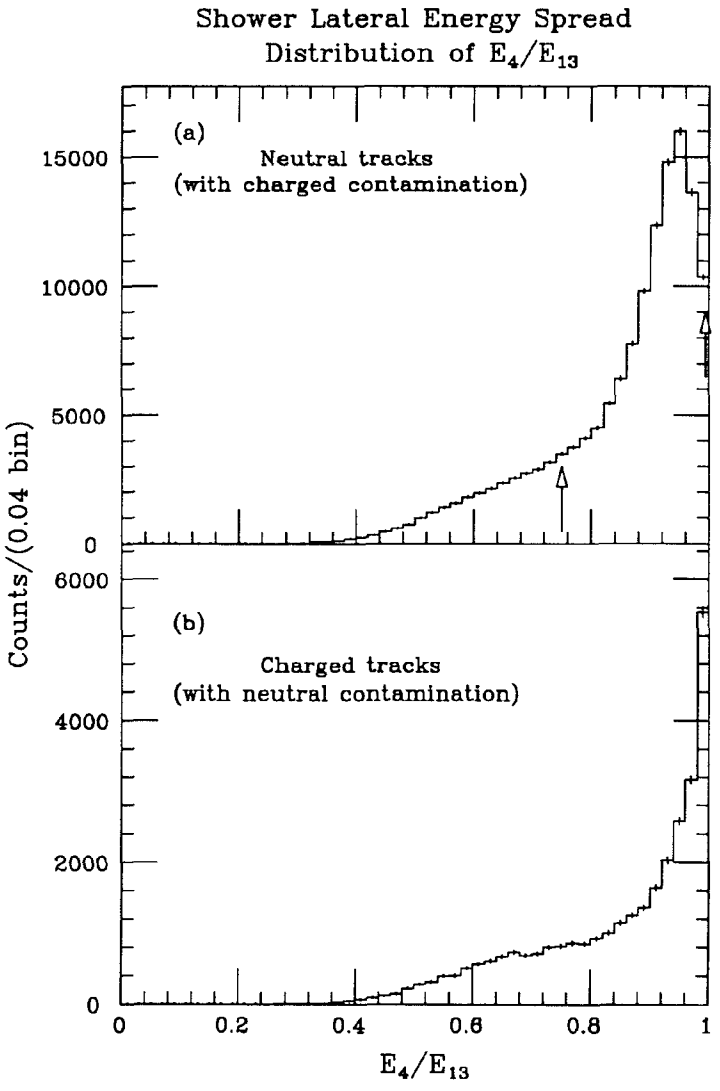

Fig. 4.2 Distribution of E_4/E_{13}, one measure of the lateral energy spread of a shower. (a) The distribution for tracks determined to be neutral by the production algorithm, including misidentified charged track contamination. (b) The distribution for tracks determined to be charged by the production algorithm, including contamination from misidentifed neutral tracks. The arrows on (a) indicate the upper and lower limits allowed for tracks used as photons.

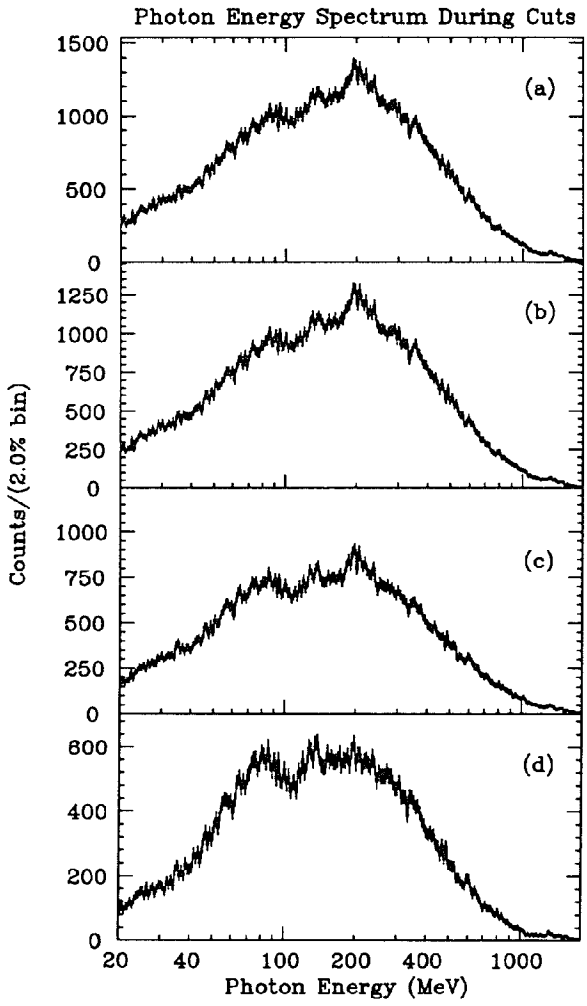

Fig. 4.3 The energy spectrum of tracks observed at E_{cm}=4.028 GeV before, during, and after photon selection cuts. (a) Energies of all tracks found by the production algorithm. (b) Energies after removing tracks determined to be charged by the production algorithm. (c) Energies after removing tracks contained within a cone of half-angle 23° about either the e^+ or e^- beam direction. (d) Energies after removal of tracks failing the lateral energy spread pattern cuts. In particular this has removed the prominent minimum-ionising charged-particle peak near 200 MeV. Spectrum (d) is also shown in Fig. 4.4.

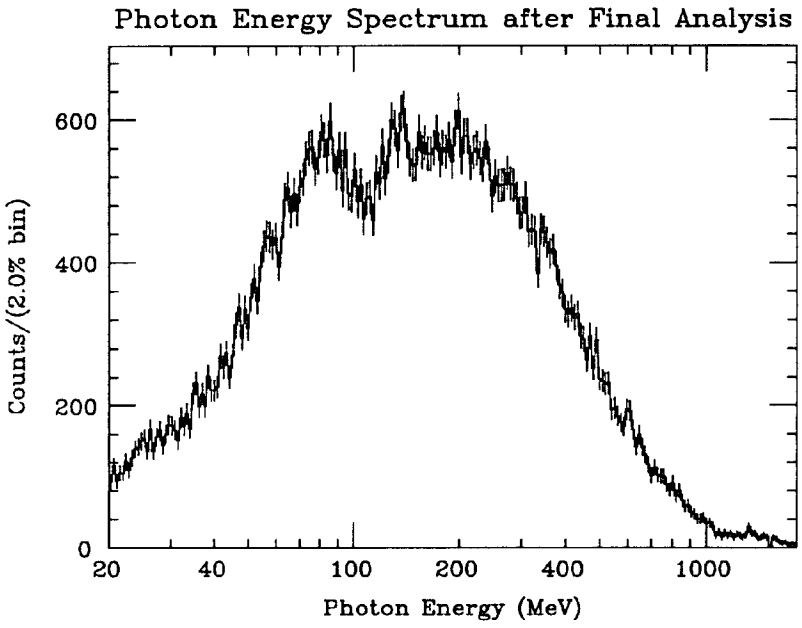

Fig. 4.4 The inclusive photon energy spectrum at E_{cm}=4.028 GeV after all analysis cuts. This spectrum is used in the measurements of the D^0 mass, the branching ratio $BR(D^{*0} \rightarrow \pi^0 D^0)$ and the mass difference $m(D^{*0}) - m(D^0)$.

4.2.3 *Photon Reconstruction Efficiencies*

Individual photon reconstruction efficiencies are not needed explicitly in this analysis; the method used to fit the inclusive spectra using sums of histograms (described in Chapter 5) has efficiency corrections included implicitly. However, for completeness and to make it possible to estimate numbers of events expected in the signal regions, explicit photon efficiencies are discussed here.

Hadronic data was "created" by using *actual* ψ'' hadron-selected events which were merged with one or more Monte Carlo photons. The ψ'' was chosen to simulate the hadronic environment containing the decay products from one or two D^*'s: the $D\overline{D}$ pair plus n photons. These merged events were then re-run through the production analysis. Efficiencies were calculated from the number of

Monte Carlo photons found after event reconstruction and the (known) number of photons generated.

Efficiencies were studied as a function of photon multiplicity: the detector simulation algorithm was used to generate crystal energy distributions for events containing 1, 2, 3, or 4 photons. The number of photons was chosen to simulate the extra photon multiplicity of $D^*\overline{D} + D\overline{D}^*$ or $D^*\overline{D}^*$ events with respect to $D\overline{D}$ events. All photons were generated isotropically over the 4π solid angle at 100 MeV; 100 MeV was chosen as an average energy of photons from the D^{*0}'s two decay modes.* The number of photons reconstructed after both production analysis and after final photon selection was recorded. Efficiencies were calculated for empty events (events as generated by the Monte Carlo containing only the photons) and for hadronic-environment events (where the photons were merged into the ψ'' hadronic data mentioned above).

A photon was considered to have been reconstructed when a match between its generated four-vector and a reconstructed track occurred. A match was found when:

$$\begin{aligned} \cos\theta_{[\text{generated}-\text{measured}]} &\geq 0.98 \quad \text{and} \\ |E_{\text{measured}} - E_{\text{generated}}|/E_{\text{generated}} &\leq 0.20\,. \end{aligned} \qquad [4.2]$$

Results are summarized in Table 4.2. As seen in the table, final photon reconstruction efficiencies are $\approx 50\%$ for hadronic events containing charm meson decays. This implies that the efficiency (to be discussed later) for detecting and reconstructing π^0's will be on the order of 25%.

---

* The efficiency for photons at energies near 140 MeV will be slightly higher by $\approx 5\%$, while efficiencies for lower energy photons near 70 MeV will be slightly lower by $\approx 5\%$ (absolute). These small effects do not affect the conclusions of this section.

Event Type	Number of Photons Added per Event	Efficiency After Production Analysis (%)	Efficiency After All Cuts (%)
Empty	1	85.9 ± 0.7	74.3 ± 0.6
	2	84.5 ± 0.7	73.8 ± 0.6
	3	82.9 ± 0.5	72.1 ± 0.5
	4	81.4 ± 0.5	70.8 ± 0.4
Hadronic	1	61.9 ± 0.6	53.6 ± 0.5
	2	60.8 ± 0.6	53.2 ± 0.5
	3	59.5 ± 0.5	52.2 ± 0.4
	4	58.2 ± 0.4	50.9 ± 0.4

Table 4.2 Reconstruction efficiencies for 100 MeV photons in empty and hadronic events as a function of multiplicity. Efficiencies are in percent (%); errors are statistical only; systematic errors are estimated to be $\lesssim 10\%$. See text for details.

4.3 Inclusive Analysis: π^0 Energy Spectra

4.3.1 *Introduction*

The 98.8% branching ratio of the pion decay mode $\pi^0 \to \gamma\gamma$ provides an excellent means for the Crystal Ball detector to track neutral pions in an efficient manner. Two methods are possible: (1) exclusive reconstruction of the π^0 by reconstructing its four-momentum from the measured four-momenta of its daughter photons; or (2) inclusive analysis of photon-photon invariant mass spectra which yields the number of π^0's above the background from "wrong combinatorics". As an example, method (1) (exclusive) is useful in extracting the distribution of $\cos\theta_{\pi^0\pi^0}$, the angular correlation between the two slow π^0's in $D^{*0}\overline{D}^{*0}$ decay (where both D^*'s have decayed via the pion mode), since both four-vectors must be available to reconstruct the angle between them. Method (2) (inclusive) is better suited to measurement of π^0 energy spectra and the inclusive angular dis-

tribution of slow π^0's from D^{*0} decay, which do not require explicit selection of two or more π^0's simultaneously. Because method (2) does not have this constraint, it has a higher efficiency for finding π^0's and considerably less background contamination as will be seen below. In both inclusive and exclusive methods, the photons used are required to pass cuts identical to the ones described above in the inclusive photon selection.

4.3.2 *Exclusive Reconstruction of π^0's.*

Description of the Method

For exclusive reconstruction each pairing of photons is fit to a π^0 mass hypothesis by calculating the invariant mass $m_{\gamma\gamma}$ of the photon pair and from it a χ^2-distributed variable (to be called simply χ^2 for the rest of this section) from the π^0 rest mass and mass resolution of the detector.[61] All pairs with a $\chi^2 < 7.0$ and subject to the constraint that no photon is used more than once are used to determine which set of pairs has the maximum confidence level greater than 0.1%; this set of pairs is then used for the exclusive analysis. A fit is done for each selected pair which constrains its invariant mass to exactly the observed π^0 rest mass,* adjusting the four-momenta of the two photons as needed (in both energy and angles). The sum of these corrected four-momenta is used as the π^0's four-momentum.

The π^0 energy spectrum calculated in this fashion is shown in Fig. 4.5 for the data from $E_{\rm cm} = 4.028$ GeV; a similar energy spectrum for the Monte Carlo process $D^{*0}\overline{D}^{*0} \rightarrow \pi^0\pi^0 D^0\overline{D}^0$ is shown in Fig. 4.6; distributions of $\cos\theta_{\pi^0\pi^0}$ computed from π^0's with total energy less than 148 MeV are shown in Figs. 4.7

* This is the π^0 rest mass as measured with the Crystal Ball detector; as will be seen shortly, the mean of the $m_{\gamma\gamma}$ distribution is slightly lower than the accepted value of the π^0 rest mass, caused by leakage from the crystals. The value used in this analysis is 134.2 MeV for data from the detector; 135.2 MeV is used for Monte Carlo simulations.

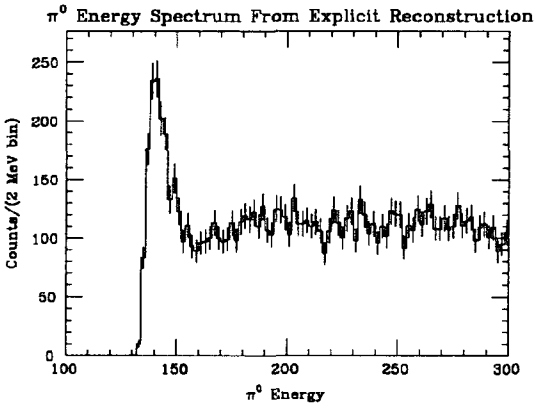

Fig. 4.5 The π^0 energy distribution produced by exclusive reconstruction of π^0's in data at $E_{\rm cm} = 4.028$ GeV. A constraint requiring the adjustment of individual photon four-momenta to fit exactly the observed π^0 rest mass has been applied. A large fraction of the plot is background contamination from incorrect combinations of photons (cf. Fig. 4.28, which is relatively background-free.).

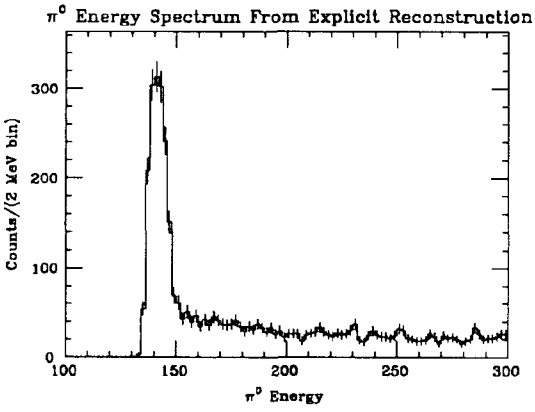

Fig. 4.6 The π^0 energy distribution produced by exclusive reconstruction of π^0's from a Monte Carlo simulation of $D^{*0}\overline{D}^{*0} \to \pi^0\pi^0 D^0\overline{D}^0$ at $E_{\rm cm} = 4.028$ GeV. A constraint requiring the adjustment of individual photon four-momenta to exactly fit the observed π^0 rest mass has been applied. The background from wrong combinatorics is much reduced with respect to Fig. 4.5, since the detector simulation does not produce as many split-off showers as observed in data.

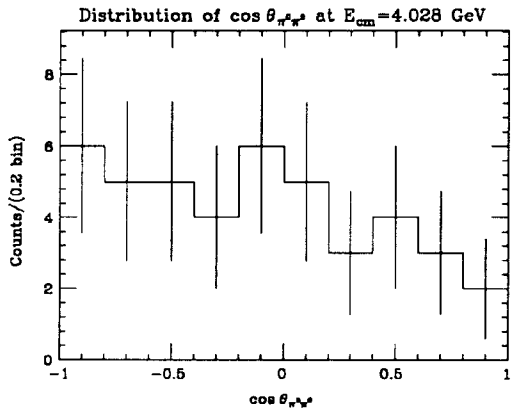

Fig. 4.7 Distribution of the angular correlation $\cos\theta_{\pi^0\pi^0}$ produced from exclusive reconstruction of π^0's from data at $E_{\rm cm}$ = 4.028 GeV. For an event to enter this figure, it must contain at least two reconstructed pions, each with total energy less than 148 MeV, so that the angle between them may be reconstructed. Background contamination from sources other than $e^+e^- \rightarrow D^{*0}\overline{D}^{*0}$ is estimated from Monte Carlo studies to be less than 10% of the total counts.

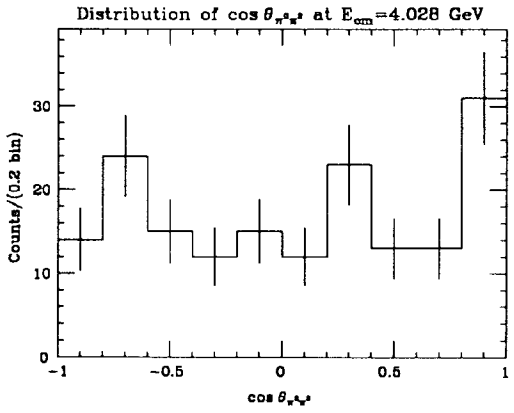

Fig. 4.8 Distribution of the angular correlation $\cos\theta_{\pi^0\pi^0}$ produced from exclusive reconstruction of π^0's from a Monte Carlo of $D^{*0}\overline{D}^{*0} \rightarrow \pi^0\pi^0 D^0\overline{D}^0$ at $E_{\rm cm}$ = 4.028 GeV. For an event to enter this figure, it must contain at least two reconstructed pions each with total energy less than 148 MeV. This distribution was produced by the analysis of 4000 events generated with $z = -1/6$ (see Appendix A).

Exclusive π^0 Reconstruction Efficiencies for $E_{\pi^0} = 140$ MeV (%)		
Number of π^0's Added per Event	Added to Empty Events	Added to ψ'' Hadronic Events
1	41.3 ± 0.5	16.6 ± 0.3
2	35.9 ± 0.3	14.1 ± 0.2

Table 4.3 Exclusive detection efficiencies for one or two π^0's merged in empty and hadronic events. All π^0's were generated isotropically at 140 MeV. Efficiencies are in percent (%); the errors listed are statistical only. Systematic errors are $\approx$ 10%.

and 4.8 for the same data and Monte Carlo samples respectively. These illustrate the strong effect D^{*0} production has on these distributions.

Disadvantages of Exclusive π^0 Reconstruction

As will be seen in the next section, the π^0 spectra computed in this fashion contain a significant fraction of wrong combinatorics; this is due in large part to mistaken identification as photons of low-energy electromagnetic and hadronic shower split-offs, as discussed in Chapter 3. This remains true even for stringent constraints on the maximum allowed χ^2/pair and total confidence level of the reconstruction fit; the inclusive method to be discussed in the next section is relatively background-free and has a much higher efficiency than the exclusive method, when the exclusive method is used with the stringent cuts. As seen in Table 4.3, efficiencies for detecting one or two low-energy pions in charm meson events is less than 20%.* However, the inclusive method does have the disadvantage of being unable to reconstruct the exclusive four-momentum for an individual pion which makes it unsuitable for measurement of the distribution of the correlation angle $\cos\theta_{\pi^0\pi^0}$ or any quantity which requires more than one

* A pion is reconstructed when a match between its generated four-vector and a reconstructed track is found, as in the case of photons; the criteria used are $\cos\theta_{\text{generated-measured}} \geq 0.98$ and $|E_{\text{measured}} - E_{\text{generated}}|/E_{\text{generated}} \leq 0.50$.

four-vector in its calculation.

4.3.3 *Statistical Determination of Inclusive π^0 Spectra*

Discussion of the Method

The statistical, or inclusive, subtraction method used to reduce "wrong combinatorics" background in the determination of inclusive π^0 spectra was first developed in another Crystal Ball analysis searching for the charm strange mesons D_S^+ and D_S^{*+} [55] and has been extended slightly in this analysis. It provides a relatively efficient means for subtracting the wrong combinatorics from $m_{\gamma\gamma}$ invariant mass plots at the expense of no longer reconstructing the individual pion four-momenta. Fortunately, finding the physical parameters to be evaluated in this experiment does not require the latter ability.

The idea is to form all pairings of photons passing the selection cuts outlined above in the photon analysis and to accumulate the invariant mass and some other quantity of interest in a two-dimensional histogram; the other quantity may be the total energy of the pair, its total three-momentum, some angle based on the four-momentum sum, *etc.* All pairings are accumulated in this histogram without regard to multiple use of any photon. Histograms of the π^0 kinetic energy $T_{\pi^0} \equiv E_{\gamma\gamma} - m_{\gamma\gamma}$ *vs.* $m_{\gamma\gamma}$ [*] are shown in Figs. 4.9 and 4.10 for data taken at $E_{\rm cm} = 4.028$ GeV and (as an example) for the Monte Carlo process $D^{*0}\overline{D}^{*0} \rightarrow \pi^0\pi^0 D^0\overline{D}^0$ respectively. This accumulation technique necessarily includes a substantial number of "wrong combinatorics" pairs which are removed by a two-dimensional background subtraction.

The π^0 spectrum in the quantity of interest is extracted by a two-step pro-

---

* The kinetic energy T_{π^0} is used instead of the total energy E_{π^0} to eliminate boundary effects in the histogram. If E_{π^0} were plotted instead, there would be an exact cutoff along the line $E_{\pi^0} = m_{\gamma\gamma}$ at 45° to both axes, making the interpretation of the fit results more difficult. Histogramming T_{π^0} is equivalent to histogramming the magnitude of the three-momentum, $|\mathbf{p}_{\pi^0}|$.

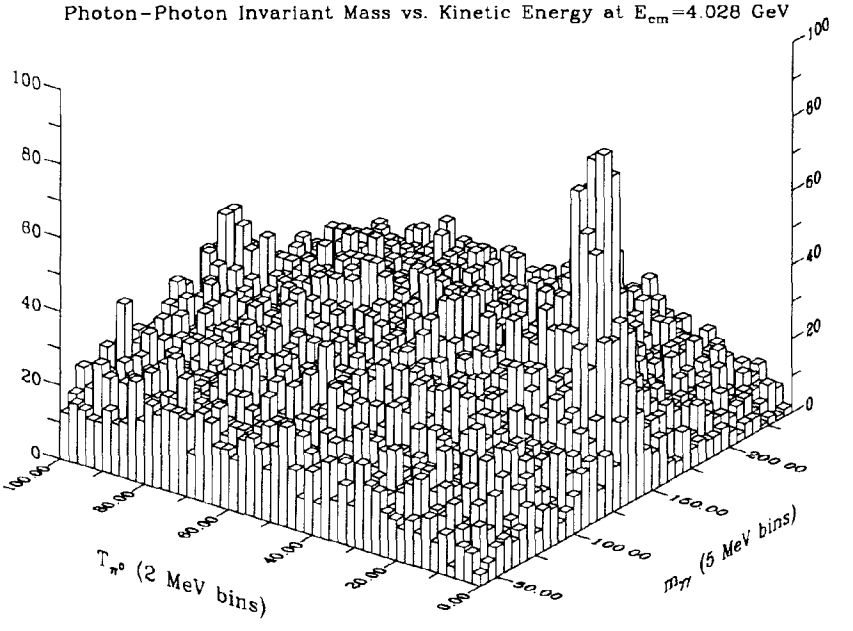

Fig. 4.9 **The two-dimensional histogram formed by accumulating the quantities $m_{\gamma\gamma}$ and $T_{\pi^0} = E_{\gamma\gamma} - m_{\gamma\gamma}$ for data taken at $E_{\rm cm}$ = 4.028 GeV. The large peak at low T_{π^0} near $m_{\gamma\gamma}$ = 135 MeV is from D^* decay.**

cedure: (1) a parameterization of the background combinatoric shape is made using the sideband regions away from the π^0 mass; and (2) the background shape is extrapolated into the π^0 mass region and the excess above the background is determined as a function of the quantity of interest.

This background subtraction is accomplished by performing a log-likelihood minimization modeling the distribution as a sum of two types of functions: (1) a two-dimensional "sheet", representing the smoothly varying combinatoric background; and (2) a set of π^0 mass resolution functions, representing the amplitude of the π^0 signal as a function of π^0 energy. The first function is constructed from a tensor product of polynomials and one-dimensional histograms providing a two-

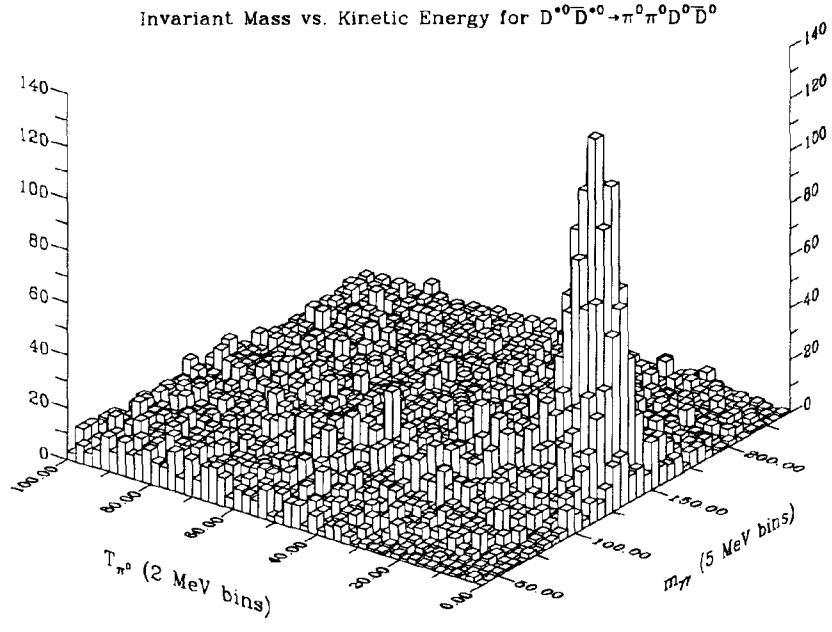

Fig. 4.10 The two-dimensional histogram formed by accumulating the quantities $m_{\gamma\gamma}$ and $T_{\pi^0} = E_{\gamma\gamma} - m_{\gamma\gamma}$ for the Monte Carlo process $D^{*0}\overline{D}^{*0} \to \pi^0\pi^0 D^0\overline{D}^0$ at $E_{\rm cm}$ = 4.028 GeV. The large peak at low T_{π^0} near $m_{\gamma\gamma}$ = 135 MeV is from D^{*0} decay.

dimensional "background sheet" defined for each bin (x, y) in the histogram.* The second function is a sum of π^0 mass resolution lineshapes, one for each row at fixed y, *i.e.*, for each "slice" parallel to the x axis. Each lineshape function, a strong function of E_{π^0}, is predetermined as discussed below except for its amplitude; this amplitude is determined in the global fit to the two-dimensional histogram. In this fashion a single amplitude is obtained from the two-dimensional fit for each bin in y, the quantity of interest for which it is desired to obtain an inclusive spectrum; the background function has been used to remove the wrong combinatorics background. The major concern with the method is of course

* The coordinates (x, y) indicate the center of a bin; x lies along the $m_{\gamma\gamma}$ axis and y along the other axis.

systematic problems in the background subtraction; it is indeed possible to over-subtract and start removing "good" π^0's from the inclusive distribution by using a "too-flexible" background function. This effect is minimized by performing the background sideband fit first and by reasonable choice of polynomial orders and one-dimensional histograms to use in constructing the background function.

The Two-dimensional Background Function

The background function is of the form

$$b(x,y) = \sum_{i=1}^{I}\sum_{j=1}^{J} \alpha_{ij}\, P_i(\hat{x})P_j(\hat{y}) + \sum_{k=1}^{K}\sum_{l=1}^{L} \beta_{kl}\, P_k(\hat{x})h_l(y)\,, \qquad [4.3]$$

where (x,y) are the coordinates of the center of a given bin in the two-dimensional histogram; $P_m(\hat{z})$ is the value of the Chebyshev polynomial of order l evaluated at $\hat{z}$; $\hat{z}$ is the normalized value of z scaled to the domain of the polynomials $[-1,+1]$; and $h_n(y)$ is a smoothed histogram used to model features of the data not easily simulated by the polynomial sum, such as the rapid rise in counts for increasing T_{π^0} above threshold. The background function used in this analysis has $I = 4$, $J = 3$, $K = 1$, and $L = 1$. The histogram $h_1(y)$ is displayed in Fig. 4.11; it is the smoothed projection of the entire two-dimensional histogram onto the y-axis.* It was anticipated that the projection of the distribution onto the y-axis might be systematically different between the Monte Carlo and the data because of poor simulation of hadronic split-off showers; thus different background histograms were used for the data and Monte Carlo samples. In practice it happened that the projections were actually quite similar and this procedure was not really necessary.

Fits to the sidebands for the first 14 slices of 2 MeV width in T_{π^0} are shown in Figs. 4.12–4.14. It is to be emphasized that the fit is two-dimensional in nature

* The smoothing algorithm fits a 4^{th}-order sum of Legendre polynomials to the histogram. Smoothing is necessary to prevent statistical fluctuations in the histogram from influencing the χ^2 calculation in the two-dimensional fit.

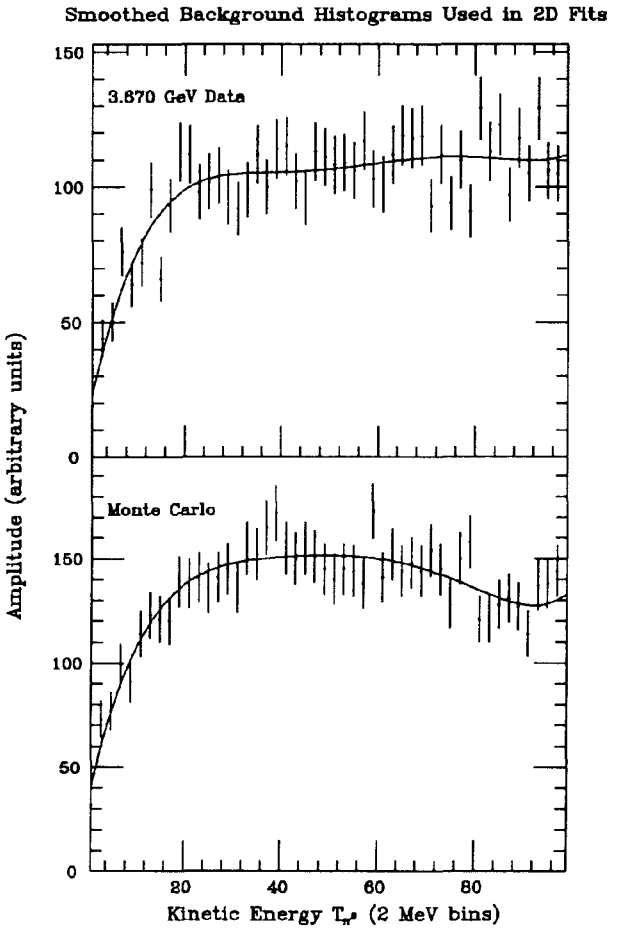

Fig. 4.11 The original projection and the smoothed histogram used in calculation of the background sheet function for extraction of T_{π^0} kinetic energy spectra. This is the projection of a two-dimensional histogram onto the kinetic energy (y) axis. Two versions are used; it was anticipated that the data and Monte Carlo could have systematically different projections from the presence of hadronic split-off showers in the data that are not simulated well in the Monte Carlo. However, inspection of these figures indicates there is no significant difference. The data version is from $E_{\rm cm} = 3.670$ GeV; the Monte Carlo version is from a simulation of the process $e^+e^- \rightarrow D^0\overline{D}^0$ at $E_{\rm cm} = 4.028$ GeV. Only this process is considered; the energy threshold effects that this models are not affected by the addition of π^0's from D^* decay.

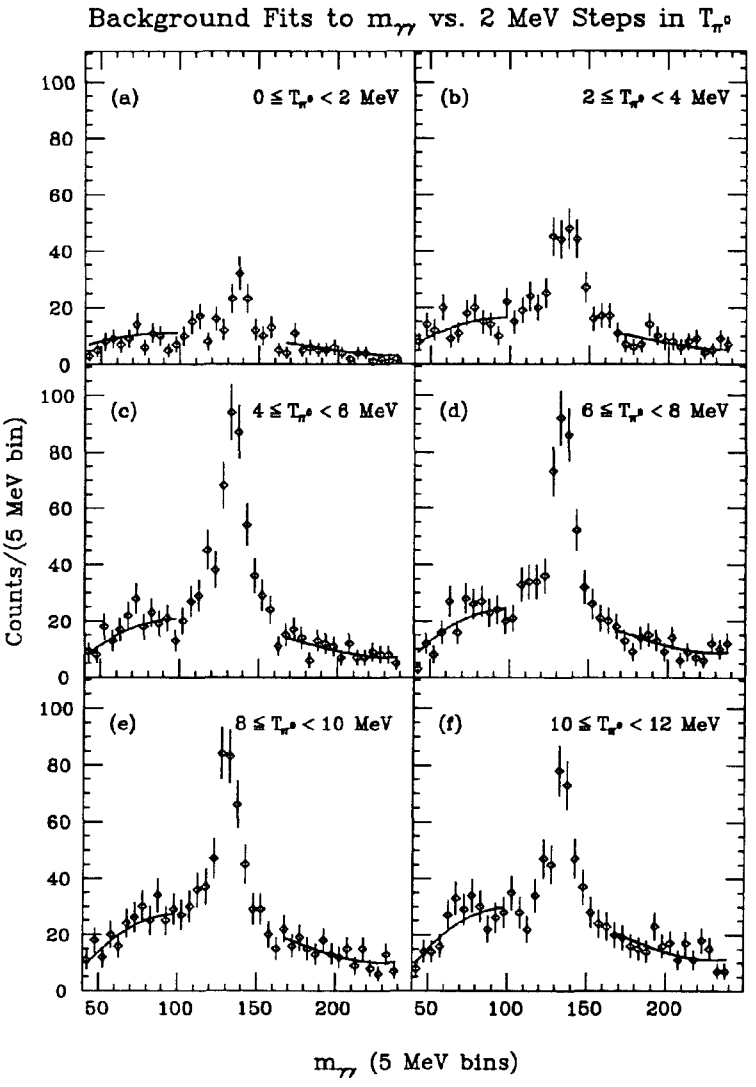

Fig. 4.12 Background sheet sideband fits to the $m_{\gamma\gamma}$ *vs.* T_{π^0} histogram in data taken at $E_{\rm cm} = 4.028$ GeV for values of T_{π^0} from 0 to 12 MeV. The fits are two-dimensional in nature; the sheets are continuous not only in $m_{\gamma\gamma}$ but also from slice to slice.

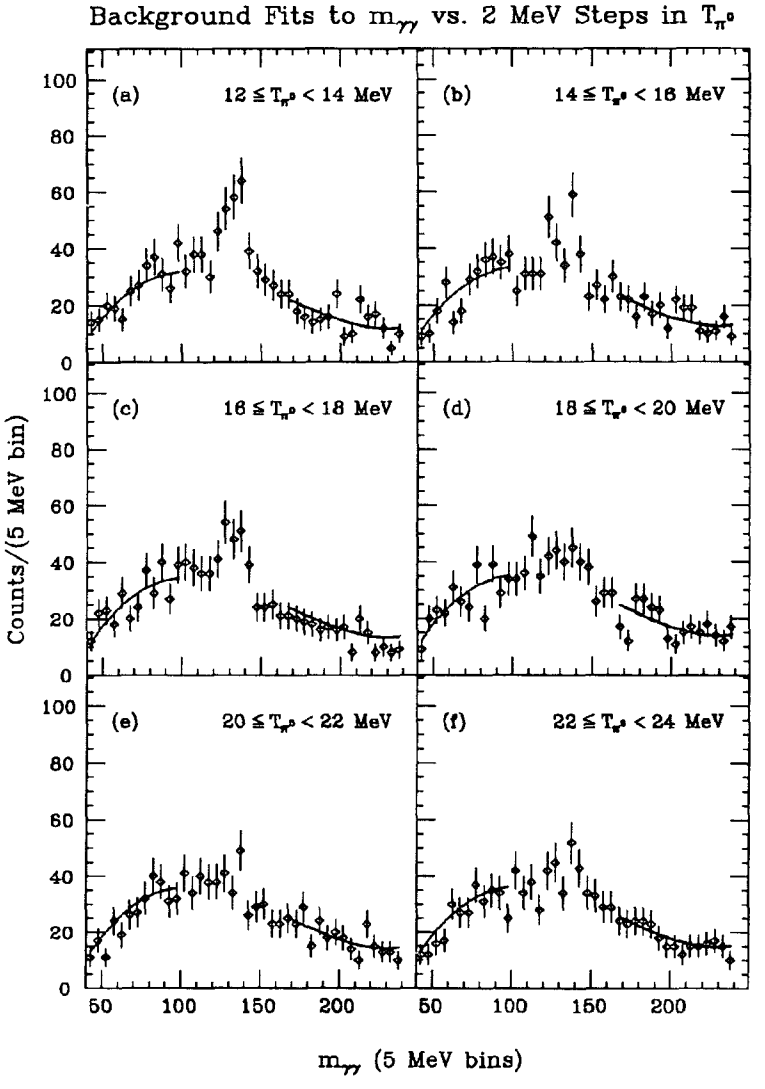

Fig. 4.18 Background sheet sideband fits to the $m_{\gamma\gamma}$ *vs.* T_{π^0} histogram in data taken at $E_{\rm cm}$ = 4.028 GeV for values of T_{π^0} from 12 to 24 MeV. The fits are two-dimensional in nature; the sheets are continuous not only in $m_{\gamma\gamma}$ but also from slice to slice.

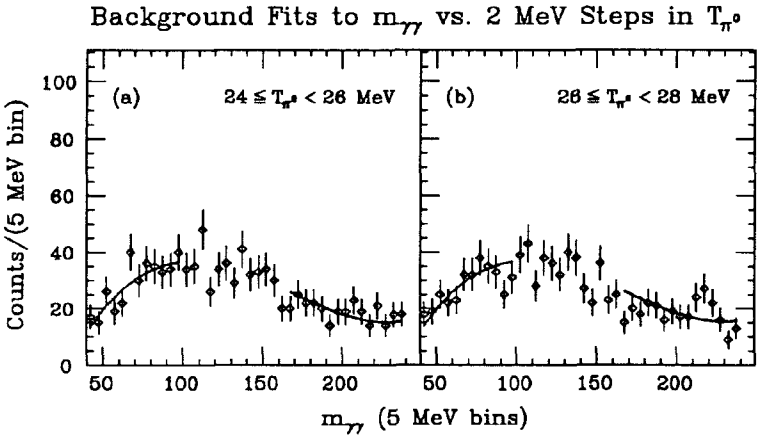

Fig. 4.14 Background sheet sideband fits to the $m_{\gamma\gamma}$ *vs.* T_{π^0} histogram in data taken at $E_{\rm cm} = 4.028$ GeV for values of T_{π^0} from 24 to 28 MeV. The fits are two-dimensional in nature; the sheets are continuous not only in $m_{\gamma\gamma}$ but also from slice to slice.

with continuity in T_{π^0}; the slices have been plotted separately for ease of viewing in these figures. The background sheet determined in this fashion is shown in Fig. 4.15 and its extrapolation under the peak region in Fig. 4.16. All these fits have confidence levels greater than 10%.

Determination of π^0 Mass Resolution Parameters

In order to fit the above-background components of the two-dimensional histogram, the π^0 mass resolution lineshape parameters must be determined. The π^0 lineshape function introduced at this point is an empirical combination of a Gaussian distribution with a mean μ and width σ, with a power-law tail on the low-mass side joined to the Gaussian continuously and with a continuous first derivative at a mass value $m' \equiv \mu - \alpha\sigma$, where α is the *join parameter*; the exponent in the tail is p. These parameters μ, σ, α, and p must be determined bearing in mind that they may vary with increasing π^0 energy; indeed, as the π^0 energy increases, the two decay photons will eventually be merged in the detector rest frame into a single shower by the Lorentz boost and can no longer be separated

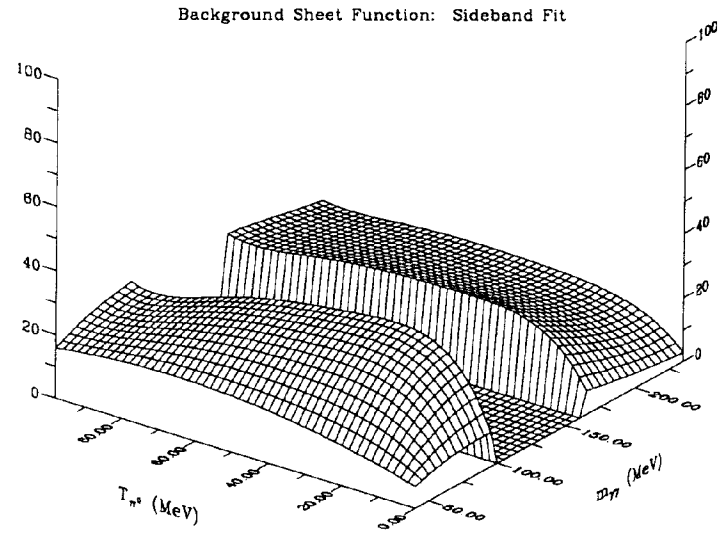

Fig. 4.15 **Background sheet function determined by sideband fit to data at $E_{\rm cm}$ = 4.028 GeV.**

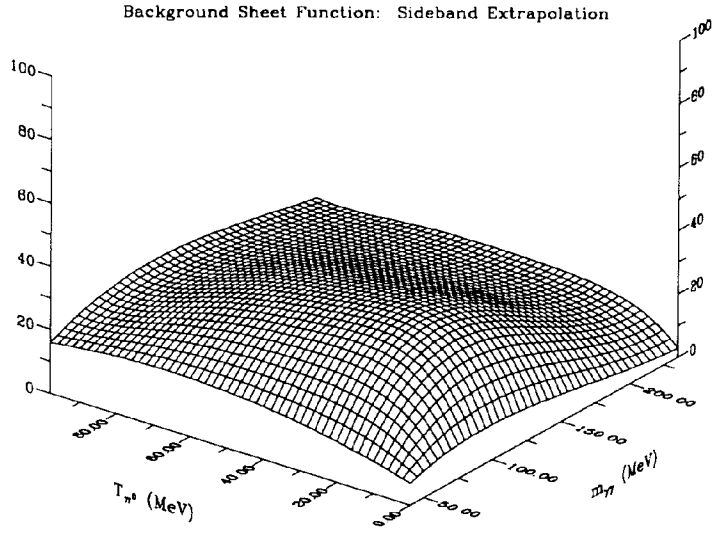

Fig. 4.16 **Extrapolation under the π^0 mass region of the background sheet function determined by sideband fit to data at $E_{\rm cm}$ = 4.028 GeV.**

into two distinct photons. This will not concern us in this analysis, since we only look at π^0's with kinetic energy less than 100 MeV; but even here the resolution capability decreases as the kinetic energy increases.[62] The explicit differential form for the empirical lineshape function is

$$\frac{dN}{dm_{\gamma\gamma}} = \begin{cases} \exp\left\{-\frac{(m_{\gamma\gamma}-m_{\pi^0}^{\rm obs})^2}{2\sigma^2}\right\} & \text{if } m_{\gamma\gamma} \geq m_{\pi^0}^{\rm obs} - \alpha\sigma; \\ \left(\frac{\sigma p}{\alpha}\right)^p \exp\left\{-\frac{\alpha^2}{2}\right\} \left(m_{\pi^0}^{\rm obs} + \sigma\left(\frac{p}{\alpha} - \alpha\right) - m_{\gamma\gamma}\right)^{-p} & \text{otherwise.} \end{cases} \quad [4.4]$$

This function is integrated over the bin widths in the fit.

Comparison of Monte Carlo studies with data from the detector have shown that the electromagnetic shower simulation models the lineshape behavior at these low pion energies sufficiently well to allow the extraction of α, p, and σ from Monte Carlo simulations and to allow use of these for data fits as well as for Monte Carlo fits; however, the mean μ is extracted separately from detector data and Monte Carlo simulations. More specifically, the three parameters α, p, and σ are obtained from fits to Monte Carlo pion spectra; these values are then used in fixing the lineshape function (except for amplitude) in fits performed on *both* Monte Carlo spectra and spectra from detector data. However, the fourth parameter, the mean μ, is derived separately for Monte Carlo data and detector data. For Monte Carlo fits, the mean $\mu_{\rm MC}$ is derived from high-statistics Monte Carlo spectra as a function of T_{π^0} and then held at these fixed values for fits performed on lower-statistics spectra for the several Monte Carlo processes considered in this analysis. Similarly, for fits to spectra from the detector, the mean $\mu_{\rm data}$ is derived from the available data at 4.028 GeV as a function of T_{π^0} and then held at these fixed values for fits performed on all spectra from the detector in this analysis. The detector simulation algorithm does not model the leakage into the crystal wrappings sufficiently well to use the Monte Carlo mean in the data fits.

The lineshape parameters are found as a function of π^0 kinetic energy by

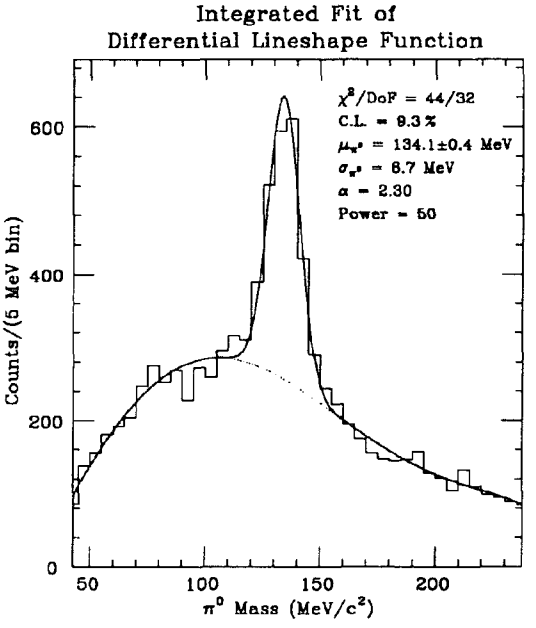

Fig. 4.17 A polynomial-plus-lineshape fit to the π^0 mass spectrum for π^0 kinetic energies up to 20 MeV. Data shown are from $E_{\rm cm}$ = 4.028 GeV.

taking a two-dimensional histogram of $m_{\gamma\gamma}$ *vs.* T_{π^0} and forming five projections* onto the invariant mass axis for values of T_{π^0} in 20 MeV steps, *i.e.*, $0 \leq T_{\pi^0} <$ 20 MeV, ..., $80 \leq T_{\pi^0} < 100$ MeV. Each projection is fitted with a polynomial background and a π^0 mass lineshape; a typical fit to data at $E_{\rm cm}$ = 4.028 GeV for the 0–20 MeV projection is shown in Fig. 4.17. For each parameter (except the power p, which is fixed at $p = 50$ since the fits are insensitive to p over a wide range—the other parameters can be adjusted to compensate) a first- or second-order polynomial is fitted to the measured values *vs.* T_{π^0}; the interpolated value is calculated from this fit for each slice in T_{π^0} in the two-dimensional peak fits. The interpolations are shown in Figs. 4.18–4.21.

* These projections are made in 20 MeV steps to ensure that each has sufficient statistics to allow accurate determination of the lineshape parameters.

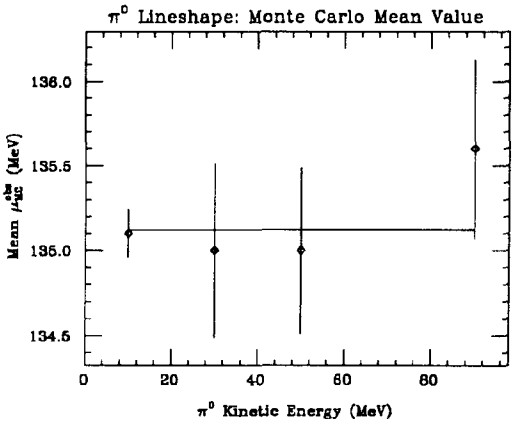

Fig. 4.18 The four measured values for the Monte Carlo mean of the π^0 lineshape function and interpolating curve. The curve is determined by a log-likelihood minimization to a constant function. The constant value $\mu_{MC}^{obs} = 135.2$ MeV determined in this way is used in all lineshape fits to Monte Carlo π^0 mass spectra.

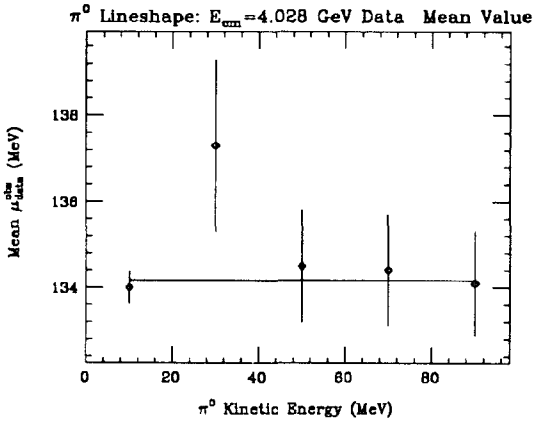

Fig. 4.19 The five measured values for the mean of the π^0 lineshape function and the interpolating curve for data taken at $E_{cm} = 4.028$ GeV. The curve is determined by a log-likelihood minimization to a constant function. The constant value $\mu_{data}^{obs} = 134.2$ MeV determined in this way is used in all lineshape fits to colliding-beam data π^0 mass spectra.

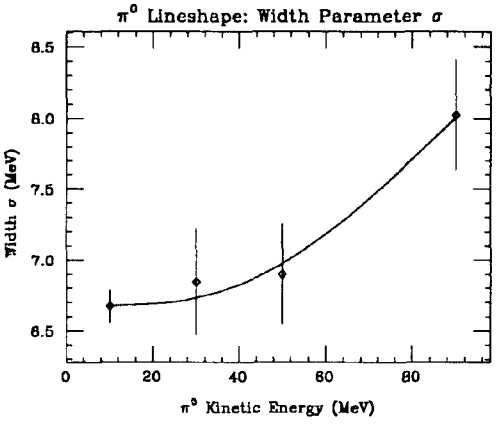

Fig. 4.20 The four measured values of the Monte Carlo width parameter for the π^0 lineshape function and interpolating curve. The curve is determined by a log-likelihood minimization to a quadratic polynomial. This curve is used in interpolating the width parameter as a function of T_{π^0} in all lineshape fits to π^0 mass spectra.

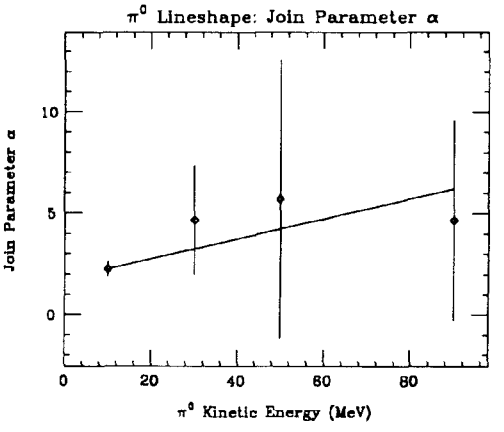

Fig. 4.21 The four measured values of the Monte Carlo join parameter α for the π^0 lineshape function and interpolating curve. The curve is determined by a log-likelihood minimization to a linear polynomial. This curve is used in interpolating the join parameter as a function of T_{π^0} in all lineshape fits to π^0 mass spectra.

Results of Peak Fits

A pion energy spectrum was computed using the inclusive method for *every* data set and Monte Carlo simulation of D and D^* processes used in this analysis. As an illustration, the results of the peak fits for the first 14 slices* of 2 MeV width for data at $E_{\rm cm} = 4.028$ GeV are shown in Figs. 4.22–4.24. Fig. 4.25 shows the full two-dimensional fit function of the extrapolated background sheet summed with the peak lineshape functions; and Fig. 4.26 shows the background-subtracted distribution. The fitted residual signal is shown in Fig. 4.27. The inclusive π^0 kinetic energy histogram extracted from this is shown in Fig. 4.28. The signature for copious D^* production, a rapid increase in pion production for increasing kinetic energy, followed by a similar sharp decline, is seen in these figures.

The use of these pion energy spectra, and the associated photon spectra described earlier, in measurement of D^* properties is the subject of the next chapter.

---

* Displayed as examples of the most interesting region; all fits—for the data and for all Monte Carlo processes, for all D^0 and Δm mass combinations under study—exist.

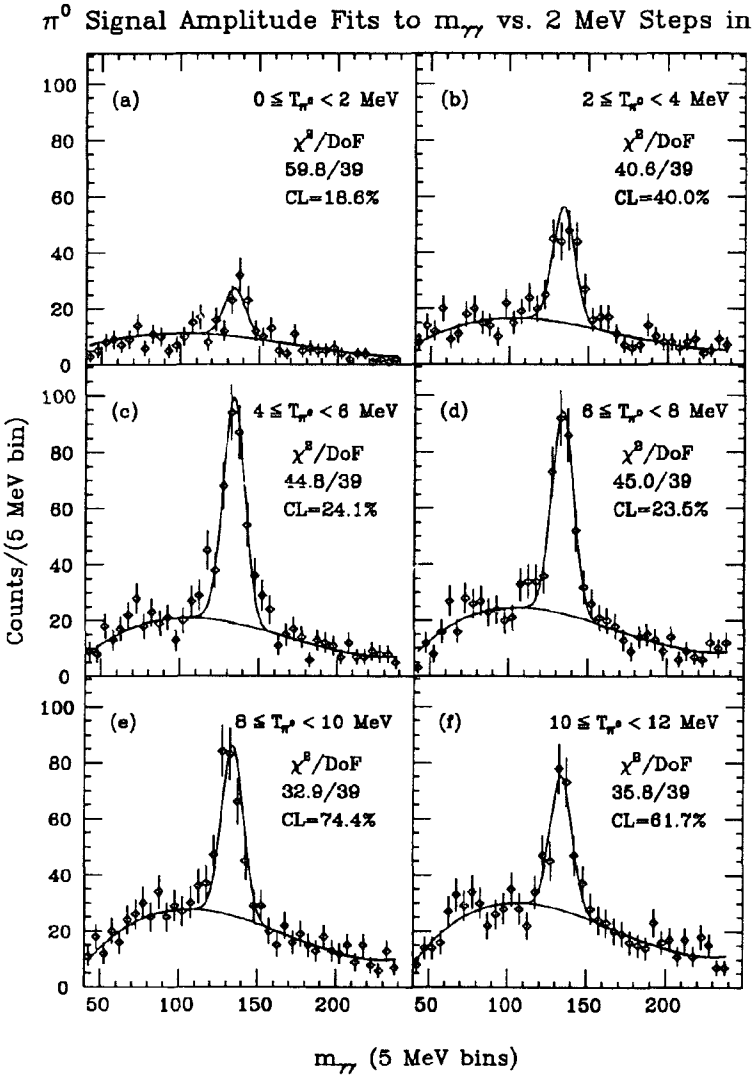

Fig. 4.22 Pion lineshape fits to the slices in T_{π^0} for the backgrounds determined in Fig. 4.12. The background as found earlier is fixed and interpolated under the π^0 mass region. Each slice is an independent fit.

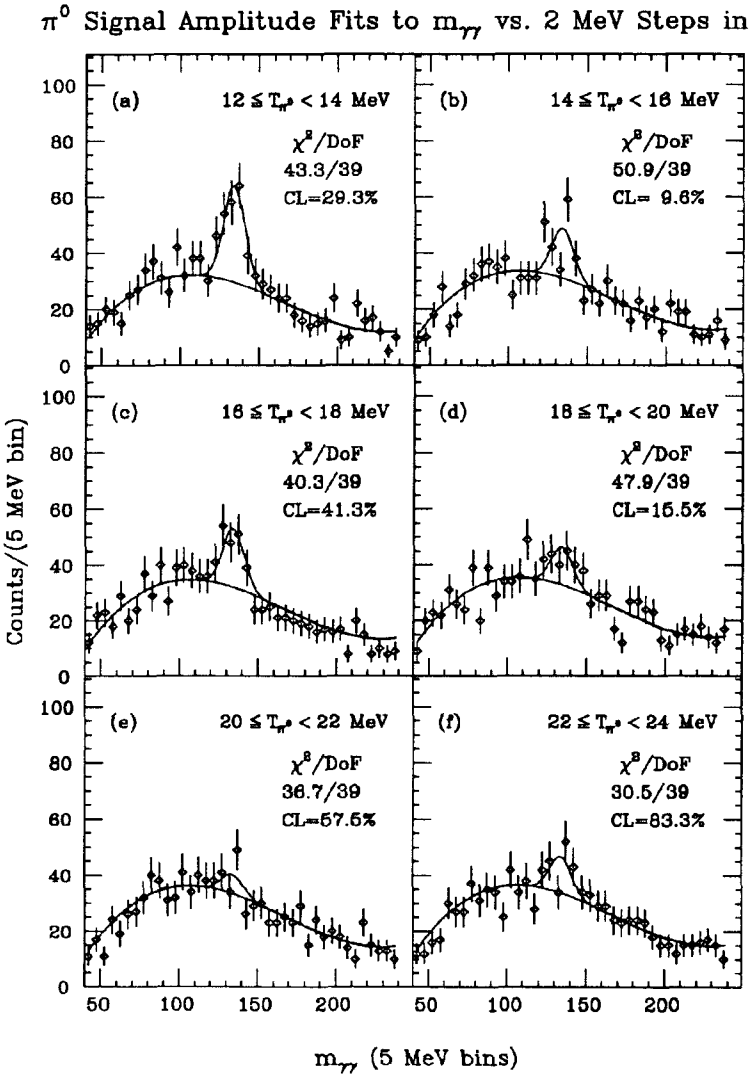

Fig. 4.23 Pion lineshape fits to the slices in T_{π^0} for the backgrounds determined in Fig. 4.13. The background as found earlier is fixed and interpolated under the π^0 mass region. Each slice is an independent fit.

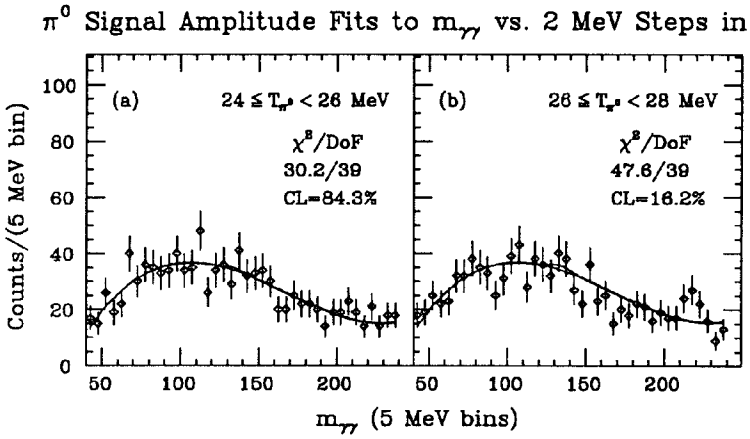

Fig. 4.24 Pion lineshape fits to the slices in T_{π^0} for the backgrounds determined in Fig. 4.14. The background as found earlier is fixed and interpolated under the π^0 mass region. Each slice is an independent fit.

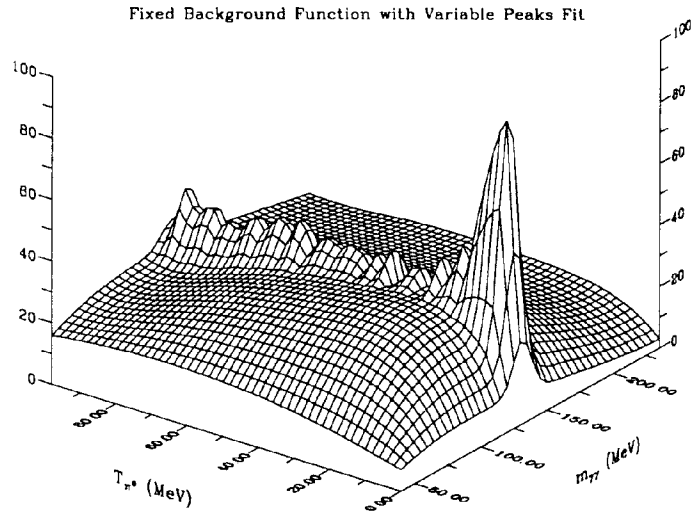

Fig. 4.25 The extrapolated background-plus-peaks fit to data at $E_{\rm cm} = 4.028$ GeV.

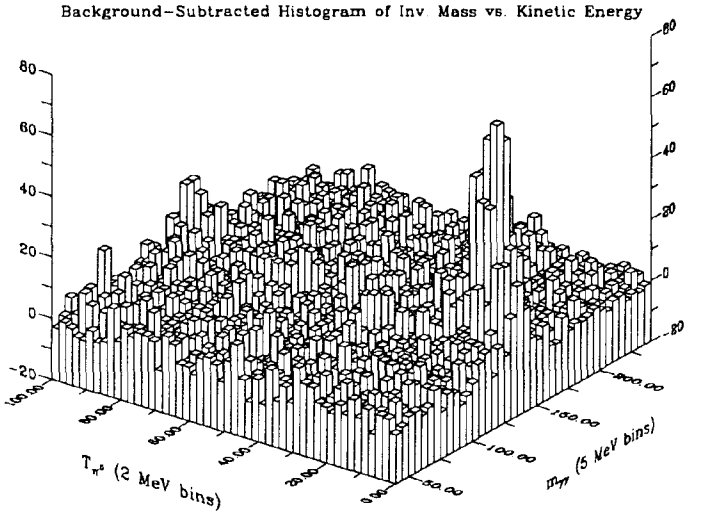

Fig. 4.26 The two-dimensional background-subtracted distribution of data at $E_{\rm cm}$ = 4.028 GeV. The amplitude of a fit to each slice is plotted as a histogram in Fig. 4.28.

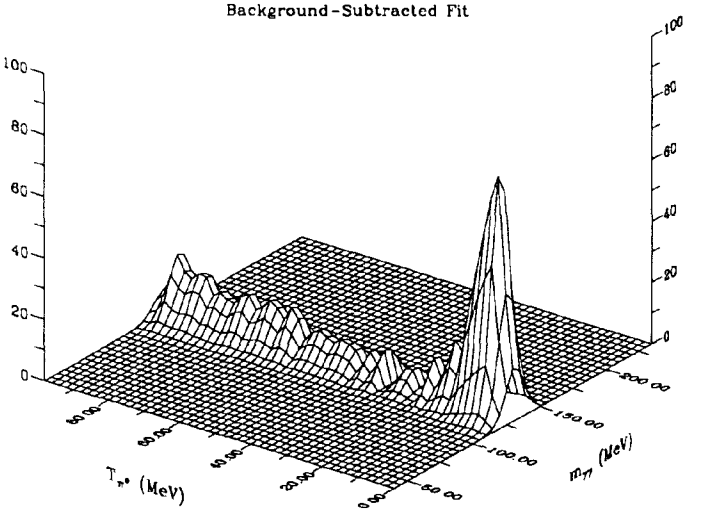

Fig. 4.27 The two-dimensional background-subtracted fit to data at $E_{\rm cm}$ = 4.028 GeV. The amplitude of each slice is plotted as a histogram in Fig. 4.28.

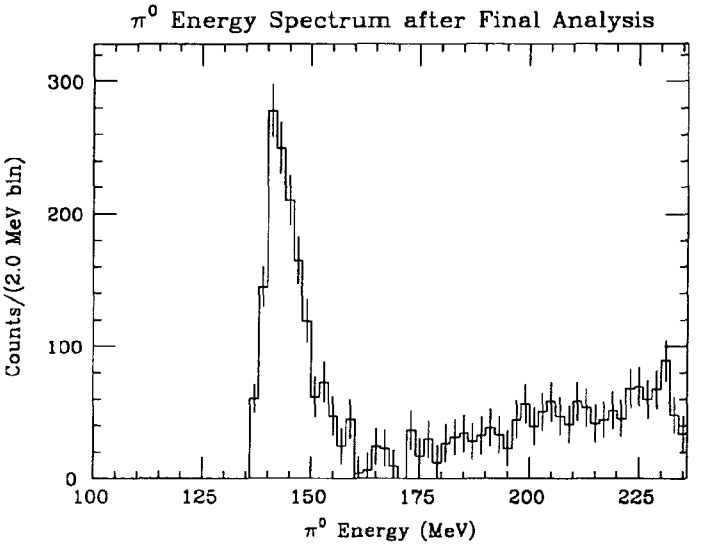

Fig. 4.28 The inclusive π^0 energy spectrum at E_{cm}=4.028 GeV after all analysis cuts. This spectrum is used in the measurements of the D^0 mass, the branching ratio $BR(D^{*0} \rightarrow \pi^0 D^0)$ and the mass difference $m(D^{*0}) - m(D^0)$.

Chapter 5

Determination of D^{*0} Branching Ratio and Masses

5.1 Introduction

Having described the procedures for generating the inclusive photon and π^0 energy spectra in Chapter 4, we will turn our attention to extracting the physical quantities of interest: the $D^{*0} \rightarrow \pi^0 D^0$ branching ratio and the mass difference $m(D^{*0}) - m(D^0)$; for the remainder of this discussion, define

$$\Delta m \equiv m(D^{*0}) - m(D^0). \qquad [5.1]$$

As a check on the correctness of the analysis procedure a measurement is made of the D^0 mass which may be compared to the accepted value, which has been reliably measured by independent experiments.

Since the D^{*0} decays to the D^0 via both photons and π^0's, both photon and π^0 energy spectra are investigated. The branching ratio

$$\mathrm{BR}(D^{*0} \rightarrow \pi^0 D^0) \qquad [5.2]$$

and its complement

$$\mathrm{BR}(D^{*0} \rightarrow \gamma D^0) \equiv 1 - \mathrm{BR}(D^{*0} \rightarrow \pi^0 D^0) \qquad [5.3]$$

are the only branching ratios of interest; there are no other kinematically allowed decay modes for the $D^{*0} \rightarrow X + D^0$ decay—only the photon and the π^0 have masses less than the q value of the process.[63] During measurement of the branching ratio and masses, some information is obtained on the relative production cross-sections at 4.028 GeV for continuum, $D\overline{D}$, $D^*\overline{D} + D\overline{D}^*$, and $D^*\overline{D}^*$ processes including both charged and neutral modes. These cross-section measurements are subject to large systematic errors, however, and are not a primary result of this analysis. Fortunately, these systematics in the cross-sections are largely decoupled from the systematics in the decay parameters.

5.1.1 *Features of the Inclusive Energy Spectra*

The inclusive photon energy spectrum in the 50 to 200 MeV region shows prominent features from the two D^{*0} decay modes. See Fig. 5.1.* Below 100 MeV a Doppler-widened enhancement is observed from the process

$$\begin{array}{l} e^+e^- \rightarrow D^{*0} + X \\ \qquad\quad \hookrightarrow \pi^0 D^0 \\ \qquad\qquad\quad \hookrightarrow \gamma\gamma. \end{array} \qquad [5.4]$$

---

* The abscissa of photon energy spectra is scaled logarithmically in the photon energy to provide an approximately constant resolution width across the plot. This facilitates detection of monochromatic features when scanning the photon energy spectrum by eye. For a linear axis, using the Crystal Ball energy resolution function $\sigma(E)/E = 0.026/\sqrt[4]{E}$ (E in GeV), the width of a monochromatic line would vary with the energy E as $\Delta E = \sigma(E) = 0.026 \times E^{3/4}$. To calculate the apparent resolution in a logarithmic plot, where the abscissa is $x \equiv \ln E$, first define

$$N_{\text{linear}} \equiv \text{counts between } E \text{ and } E + \Delta E = \frac{dN}{dE}\Delta E, \text{ and}$$
$$N_{\log} \equiv \text{counts between } x \text{ and } x + \Delta x = \frac{dN}{dx}\Delta x.$$

Then the apparent resolution is found from equality $N_{\text{linear}} = N_{\log}$, so that

$$\frac{dN}{dE}\Delta E = \frac{dN}{dx}\Delta x = \frac{dN}{dE}\frac{dE}{dx}\Delta x;$$

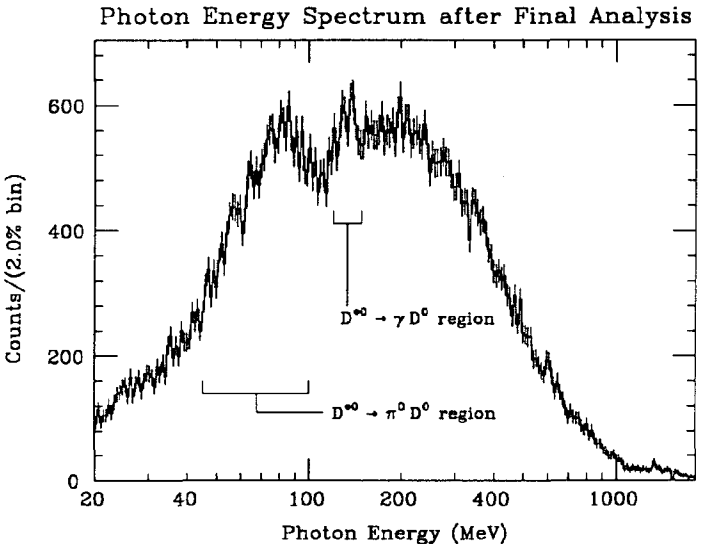

Fig. 5.1 Prominent features in the inclusive photon energy spectrum at $E_{\rm cm}$ = 4.028 GeV. The large enhancement from 50 to 100 MeV is created by photons from the decay $D^{*0} \to \pi^0 D^0$, $\pi^0 \to \gamma\gamma$. The smaller enhancement near 140 MeV is from the decay $D^{*0} \to \gamma D^0$. This spectrum is used in the measurements of the D^0 mass, the branching ratio BR($D^{*0} \to \pi^0 D^0$), and the mass difference Δm.

A smaller but still observable Doppler-widened enhancement is also seen near 140 MeV in the same figure; this is the direct photon from the decay

$$\begin{aligned} e^+e^- &\to D^{*0} + X \\ &\quad\big\lfloor\!\!\longrightarrow \gamma D^0. \end{aligned} \qquad [5.5]$$

Distinctive D^{*0} signals can be seen in the π^0 energy spectrum as well; examination of Fig. 5.2 shows a large enhancement for $E_{\pi^0} \lesssim 160$ MeV from the D^* pion decay mode. The direct photon decay does not contribute directly to this distribution. The slowly rising π^0 background observed here continues to increase

---

using the Jacobian of the transformation $dx/dE = E$, the apparent resolution Δx in the logarithmic plot is $\Delta x = 2.6\% \times E^{1/4}$ which varies much less rapidly across the plot than does the detector resolution ΔE; for $E = 50$ MeV to $E = 500$ MeV, ΔE varies by a factor of 5.6, but Δx varies only by a factor of 1.8.

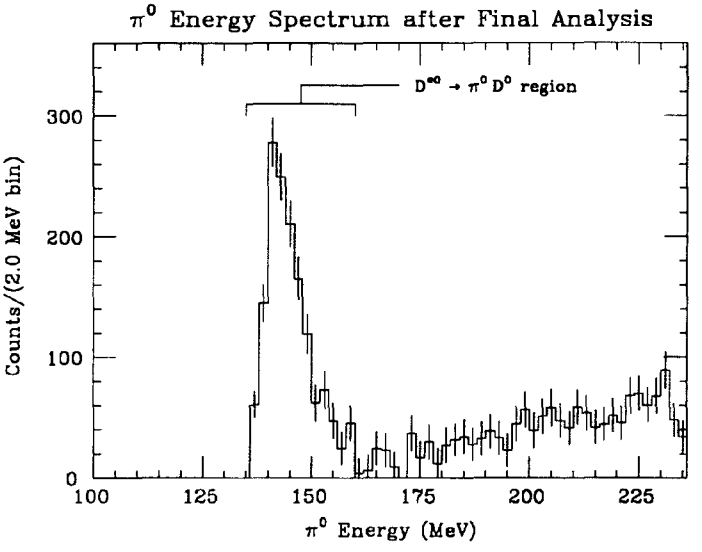

Fig. 5.2 Prominent features in the inclusive π^0 energy spectrum at $E_{cm} = 4.028$ GeV. The prominent peak is produced by the transition $D^{*0} \to \pi^0 D^0$. This spectrum is used in the measurements of the D^0 mass, the branching ratio BR($D^{*0} \to \pi^0 D^0$), and the mass difference Δm.

slowly with increasing pion energy up to some 270 MeV, followed by a similar slow decrease. This "continuum" region is populated by π^0's from many sources, including the prominent D^0 decay mode

$$D^0 \to K^- \pi^+ \pi^0 \qquad [5.6]$$

with a $17.3 \pm 1.7\%$ branching ratio[57] and with kinematic limits for $E_{\pi^0}^{(D^0)}$, the π^0 energy from this D^0 source, from 140 MeV to 1140 MeV.*

5.2 The Measurement Technique for Inclusive Distributions

The intention of this analysis is to extract measurements of the branching ratio, D^0, and D^{*0} masses; the general method used is a log-likelihood mini-

* For D^0's produced in $D^{*0}\overline{D}^0 + D^0\overline{D}^{*0}$ decay at $E_{cm} = 4.028$ GeV.

mization where a hypothesis is compared to the data, a "goodness-of-fit" calculation is made, and the parameters to be determined are varied until a maximum goodness-of-fit is obtained.[72-73] In principle, one could explicitly calculate the distributions for photon and π^0 energies for the ten processes involved (see next section), include the effects of detector resolution, acceptance, and efficiencies analytically and compare this to the data, letting the minimization algorithm select the values for all parameters. However, this "fully analytical" method is prohibitively complicated due to difficulties in parameterization of the energy spectra as a function of Δm, D^0 mass, and an unknown parameter characterizing angular distributions of the emitted photons and pions.

An alternative method is used in its place: a Monte Carlo event generator and detector simulation algorithm are used to generate spectra for the desired processes in discrete steps in D^0 and D^{*0} mass; for each of these mass combinations, a log-likelihood minimization is performed (where the D^{*0} branching ratio and production cross-sections are varied continuously by the minimization algorithm, but not $m(D^0)$ or Δm). The minimization algorithm sums together these Monte Carlo spectra (of both photon and π^0 energies) from the processes under study using a set of varying coefficients. These coefficients are adjusted for best fit to the observed spectra, and the branching ratio and cross-section values are extracted from them. After these fits are performed for several mass combinations, investigation of the goodness-of-fit parameter from each minimization allows a determination of the "best" simultaneous value for Δm and $m(D^0)$. In all of this, the remaining degree of freedom, the angular distribution parameter, is held fixed at the theoretically most-accepted value, because the sensitivity of this fitting process to it is minimal. This angular distribution parameter is discussed further in Appendix A.

As an illustration of the sensitivity of this method to the D^{*0} branching ratio, inclusive energy spectra may be produced by summing together the spectra with cross-sections predicted by a typical model.[26-27] When done for several branching

ratio values, this demonstrates the changes in the shapes and amplitudes of the signal regions as a function of the branching ratio. Figs. 5.3 and 5.4 show the spectra generated using typical cross-sections and for values of $\mathrm{BR}(D^{*0} \to \pi^0 D^0)$ of 30, 50, 70, and 90%; even by eye it can be seen upon comparison with Figs. 5.1 and 5.2 that the branching ratio must be in the range 50–70%, with $\approx 60\%$ very likely.

5.3 The Processes to be Studied

The processes which must be taken from data or parameterized by the Monte Carlo simulation in order to extract the measurements of D^{*0} parameters are discussed here. These processes include

1. Continuum (QED and non-charm (u, d, s) hadron physics).
2. Initial-state radiation.
3. $e^+e^- \to D^0\overline{D}^0$.
4. $e^+e^- \to D^{*0}\overline{D}^0 + D^0\overline{D}^{*0}$.
5. $e^+e^- \to D^{*0}\overline{D}^{*0}$.
6. $e^+e^- \to D^+D^-$.
7. $e^+e^- \to D^{*+}D^- + D^{*-}D^+$.
8. $e^+e^- \to D^{*+}D^{*-}$.
9. $e^+e^- \to D_S^+D_S^-$.

These processes are discussed individually below. As an illustration, plots of the typical photon and π^0 energy distributions for the different processes are shown in Figs. 5.5–5.9 for the mass combination point $m(D^0) = 1862.7$ MeV, $\Delta m = 140.5$ MeV.

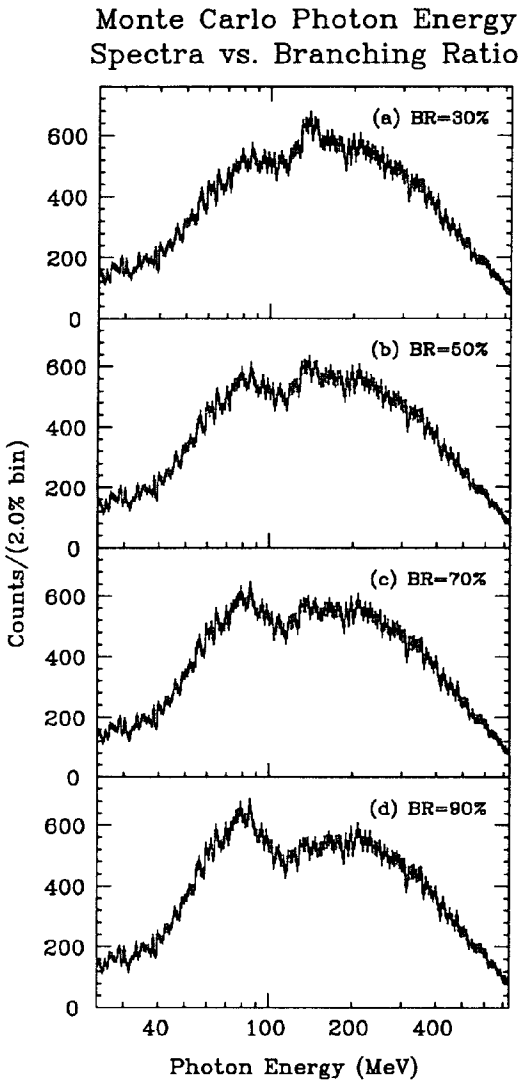

Fig. 5.3 Photon energy spectra constructed by adding Monte Carlo spectra for the processes contributing at E_{cm}=4.028 GeV. The cross-sections used in the addition are those found by the summation fit at the minimum χ^2 mass combination (see Section 5.5) and are the same for all four spectra. The BR($D^{*0} \rightarrow \pi^0 D^0$) branching ratio is varied for each figure. In the appropriate figure, the branching ratio is: (a) 30%; (b) 50%; (c) 70%; and (d) 90%.

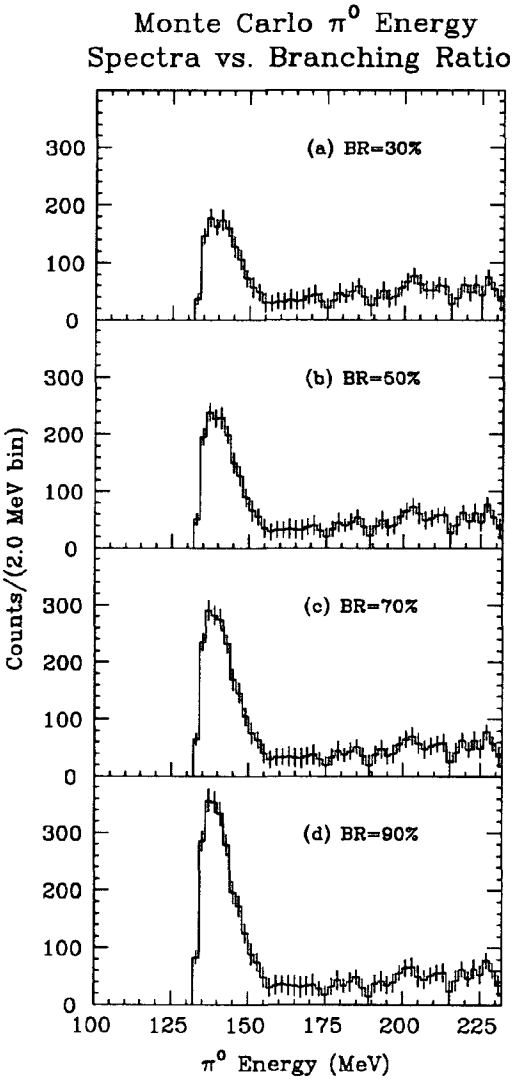

Fig. 5.4 Neutral pion energy spectra constructed by adding Monte Carlo spectra for the processes contributing at E_{cm}=4.028 GeV. The cross-sections used in the addition are those found by the summation fit at the minimum χ^2 mass combination (see Section 5.5) and are the same for all spectra. The BR($D^{*0} \rightarrow \pi^0 D^0$) branching ratio is varied for each figure. In the appropriate figure, the branching ratio is: (a) 30%; (b) 50%; (c) 70%; and (d) 90%.

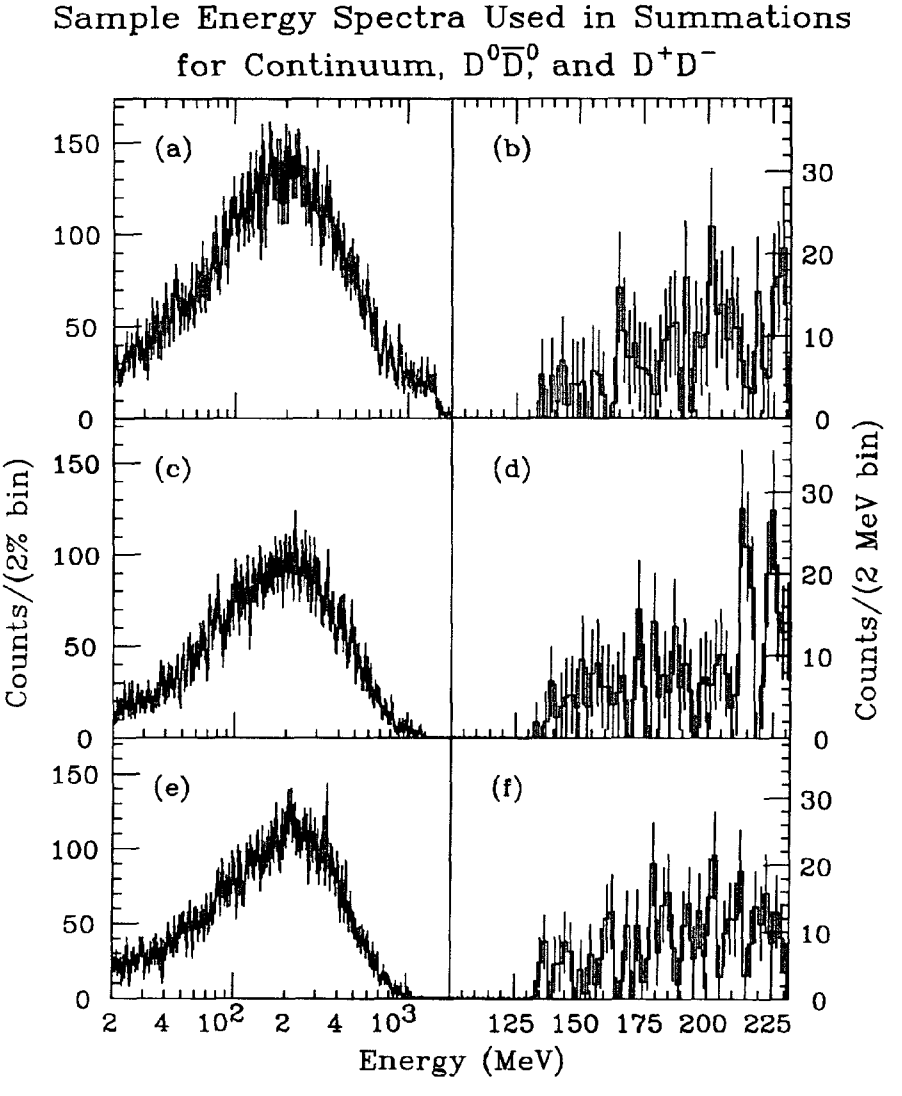

Fig. 5.5 Typical energy distributions for continuum, $D^0\overline{D}^0$, and D^+D^- processes used in the summation at one of 13 mass combinations. (a),(b) Photon and π^0 signals from continuum data at E_{cm} = 3.670 GeV. (c),(d) Photon and π^0 signals from the Monte Carlo simulation of $D^0\overline{D}^0$ production at E_{cm} = 4.028 GeV. (e),(f) Photon and π^0 signals from the Monte Carlo simulation of D^+D^- production at E_{cm} = 4.028 GeV. These are used in the global summation fit at $m(D^0)$ = 1862.7 MeV, and Δm = 140.5 MeV. These are for one of thirteen fits at various mass combinations.

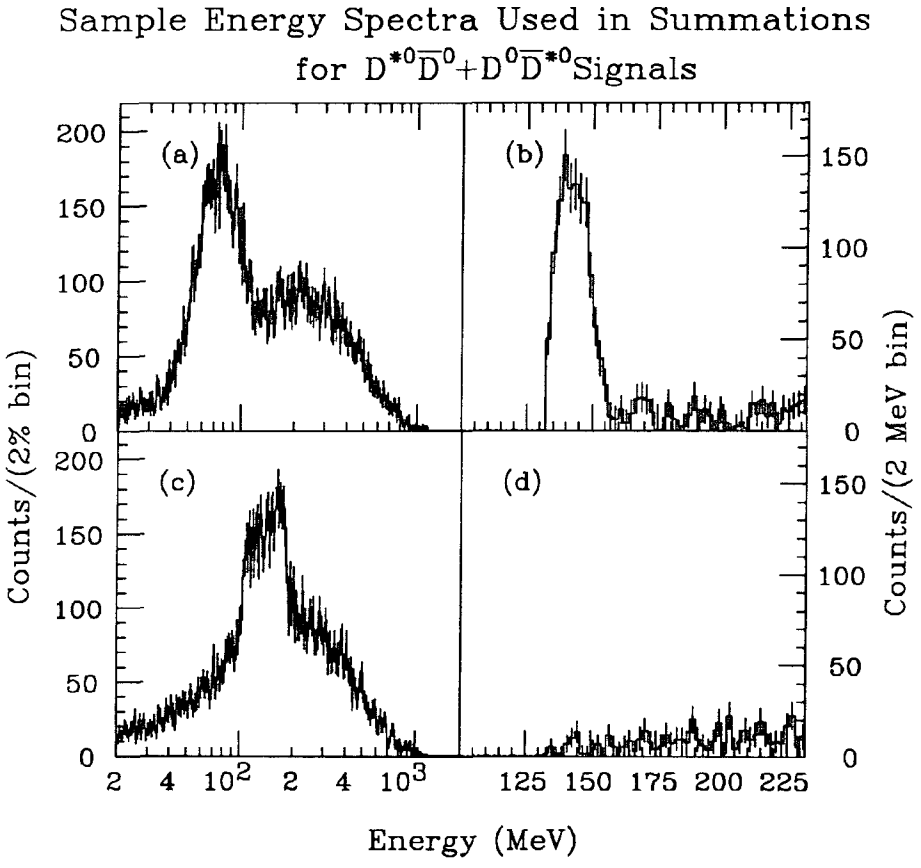

Fig. 5.6 Typical energy distributions for $D^{*0}\overline{D}^0 + D^0\overline{D}^{*0}$ processes used in the summation at one of 13 mass combinations. (a),(b) Photon and π^0 signals from the Monte Carlo simulation of $D^{*0}\overline{D}^0$ + c.c. $\rightarrow \pi^0 D^0\overline{D}^0$ production. (c),(d) Photon and π^0 signals from the Monte Carlo simulation of $D^{*0}\overline{D}^0$ + c.c. $\rightarrow \gamma D^0\overline{D}^0$ production. These are used in the global summation fit at $m(D^0)$ = 1862.7 MeV, and Δm = 140.5 MeV. These are for one of thirteen fits at various mass combinations.

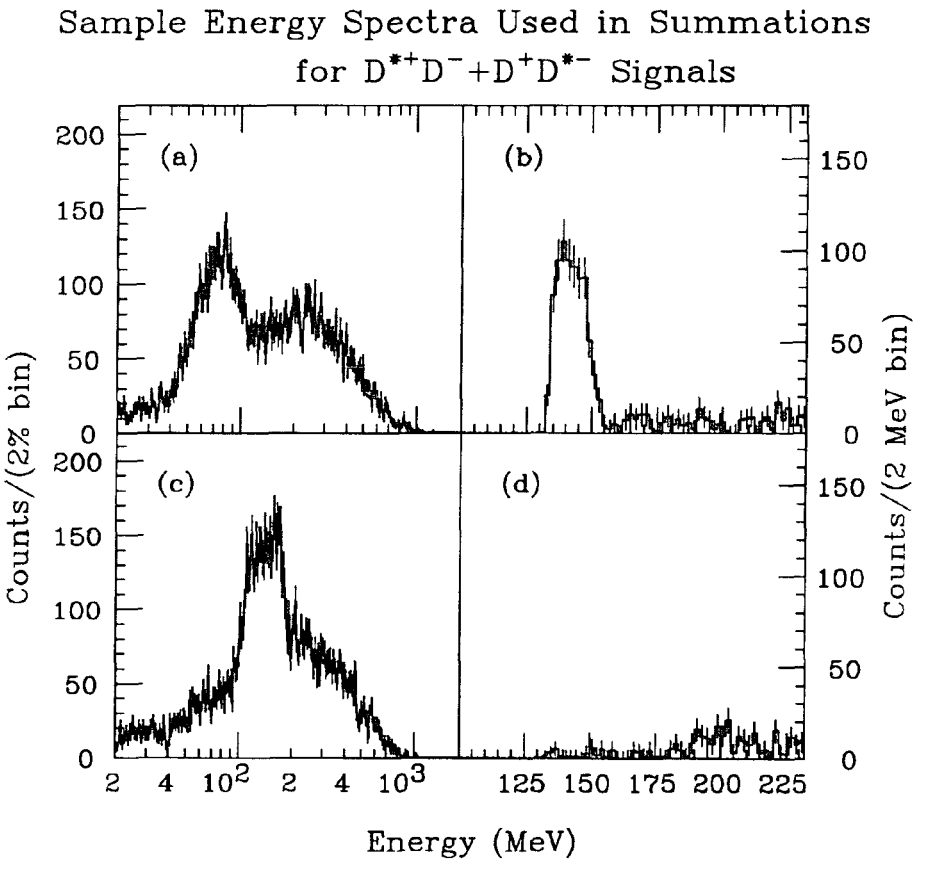

Fig. 5.7 Typical energy distributions for $D^{*+}D^- + D^+D^{*-}$ processes used in the summation at one of 13 mass combinations. (a),(b) Photon and π^0 signals from the Monte Carlo simulation of $D^{*+}D^-$ + c.c. $\rightarrow (\pi D)D^-$ production. (c),(d) Photon and π^0 signals from the Monte Carlo simulation of $D^{*+}D^-$ + c.c. $\rightarrow \gamma D^+D^-$ production. These are used in the global summation fit at $m(D^0) = 1862.7$ MeV, and $\Delta m = 140.5$ MeV. These are for one of thirteen fits at various mass combinations.

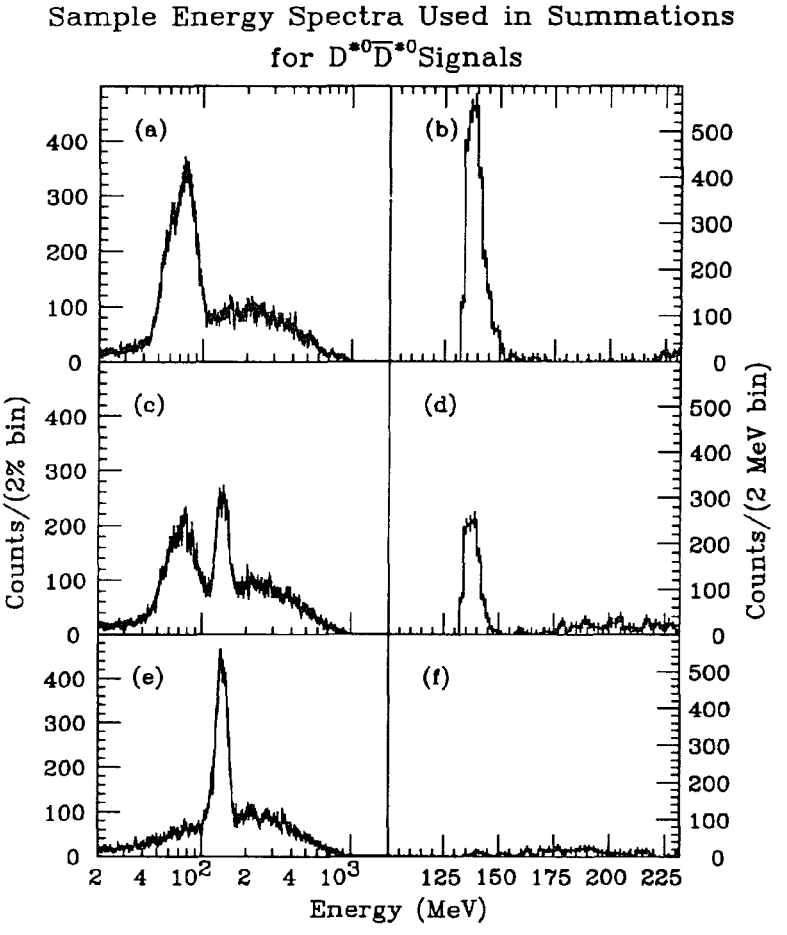

Fig. 5.3 Typical energy distributions for $D^{*0}\overline{D}^{*0}$ production and decay processes used in the summation at one of 13 mass combinations. (a),(b) Photon and π^0 signals from the Monte Carlo simulation of $D^{*0}\overline{D}^{*0} \rightarrow \pi^0\pi^0 D^0\overline{D}^0$ production. (c),(d) Photon and π^0 signals from the Monte Carlo simulation of $D^{*0}\overline{D}^{*0} \rightarrow \pi^0\gamma D^0\overline{D}^0$ production. (e),(f) Photon and π^0 signals from the Monte Carlo simulation of $D^{*0}\overline{D}^{*0} \rightarrow \gamma\gamma D^0\overline{D}^0$ production. These are used in the global summation fit at $m(D^0) = 1862.7$ MeV, and $\Delta m = 140.5$ MeV. These are for one of thirteen fits at various mass combinations.

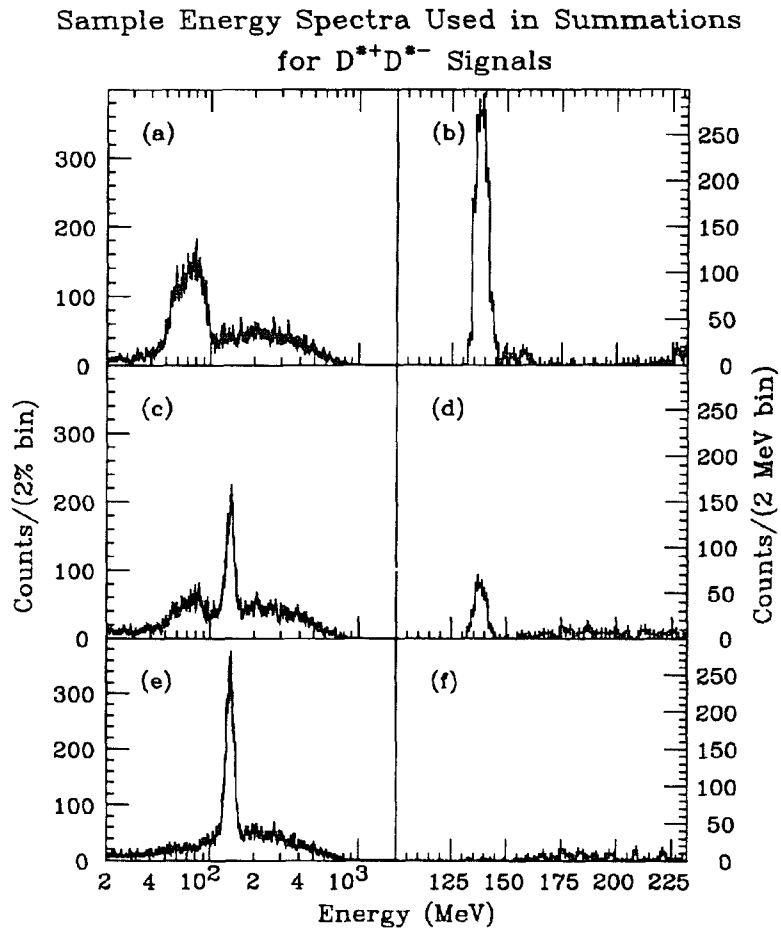

Fig. 5.9 Typical energy distributions generated for $D^{*+}D^{*-}$ production and decay processes. (a),(b) Photon and π^0 signals from the Monte Carlo simulation of $D^{*+}D^{*-} \rightarrow \pi\pi D\overline{D}$ production. (c),(d) Photon and π^0 signals from the Monte Carlo simulation of $D^{*+}D^{*-} \rightarrow \pi\gamma D\overline{D}$ production. (e),(f) Photon and π^0 signals from the Monte Carlo simulation of $D^{*+}D^{*-} \rightarrow \gamma\gamma D^{+}D^{-}$ production. These are used in systematic error calculations for the global summation fits.

5.3.1 *Continuum Physics*

The continuum physics classification includes non-charm hadronic and QED physics (the latter category only includes QED events which have deluded the hadron selector). Processes contributing via initial-state radiation are considered separately. This is the first example of the type of process that produces photon and pion spectra containing no distinctive "D^{*}" features, *i.e.*, no enhancements from the photon or pion transition. Photon spectra in this category can be characterized by a slowly rising distribution from 20 MeV up to $\approx$ 200 MeV, followed by a slow decrease to zero above 1 GeV. Similarly, neutral pion spectra show a slow rise above threshold at $E_{\pi^0} = 135$ MeV, increasing up to pion energies of $\approx$ 300 MeV, again followed by a slow decrease to zero near 800 MeV.

Process (1) distributions are obtained from data taken at $E_{\rm cm} = 3.670$ GeV. The assumption is made that the shape of the continuum spectra obtained at 3.670 GeV can be used directly at 4.028 GeV; this is necessary because the 3.670 GeV sample is the one closest in energy which does not have contributions from charm meson production or ψ' physics. No other data sample is available, and and it was decided that the data sample would better represent the continuum spectrum than one of the standard Monte Carlo simulations for $e^+e^- \rightarrow$hadrons such as the Lund string model.[65]

The lack of distinctive features in these continuum spectra, and the spectra described below which are similar to them, make it difficult to meaningfully allocate separate contributions to the cross-section from each such process. Thus only the total sum of such processes is determined in the fits to be described. In the following, the designation "continuum-like" will be used to describe featureless spectra of this nature.

5.3.2 *Processes Contributing via Initial-State Radiation*

It is well known that the electron or positron, or both, may radiate one or more photons before the annihilation interaction occurs. This is called initial-

state radiation, and must be considered as a possible contributor to the inclusive spectra studied here. In principle, the radiated photon(s) can reduce the available kinetic energy in the electron-positron center-of-mass frame to any value greater than zero. Two cases come to mind: (1) the C.M. energy of the e^+e^- pair does not lie close to a resonance, producing non-charm physics events, or (2) the pair has an appropriate energy for production of one of the narrow charm resonances.

Initial-State Radiation to Non-Resonant States

Class (1) events producing hadrons are not much different from standard continuum production of hadrons, except that the C.M. frame is boosted with respect to the lab. Also, the cross-section is very small. These events produce inclusive distributions similar to the continuum and are implicitly included in that class in the fits to be discussed. These will not be considered here any further.

Initial-State Radiation to Narrow Resonances

A significant number of class (2) initial-state radiation events can be expected at $E_{\rm cm} = 4.028$ GeV producing one of the narrow $c\bar{c}$ resonances. To calculate the cross-section for such events, let $\sigma_0^i(W)$ denote the cross-section, with no radiative corrections, for the process $e^+e^- \rightarrow \gamma X_i$ (where X_i represents some particular final state) at $E_{\rm cm} = W$. Neglecting the energy width of the beams (a very good approximation for SPEAR), the radiatively corrected cross-section, including hard- and soft-photon effects, for this process is[66]

$$\sigma^i(W) = \varepsilon\,\sigma_0^{\rm A}(W) + t\int_0^E \frac{dk}{k}\left[\left(\frac{k}{E}\right)^t - \frac{k}{E} + \frac{k^2}{2E^2}\right]\sigma_0^i\left(\sqrt{W^2 - 2Wk}\right)\,, \quad [5.7]$$

where

$$t = \frac{2\alpha}{\pi}\left(2\ln\left(\frac{W}{m_e}\right) - 1\right)\,, \quad [5.8]$$

$$\varepsilon = \frac{2\alpha}{\pi}\left(\frac{\pi^2}{6} - \frac{17}{36}\right) + \frac{13}{12}t\,, \qquad [5.9]$$

$$E = \frac{W}{2}\,, \qquad [5.10]$$

and m_e is the electron mass (k, the emitted photon energy, is integrated over). Using Eq. [5.7], the number of events expected for the data sample at $E_{\rm cm} = 4.028$ GeV from each of the three narrow charm resonances can be calculated as

$$N_i = L\sigma^i(W) = LA_i t\left(\frac{1}{E - \frac{M_i^2}{4E}}\right)\left[\left(1 - \frac{M_i^2}{4E^2}\right)^t - \frac{1}{2} + \frac{M_i^4}{32E^4}\right] \qquad [5.11]$$

where L is the total integrated luminosity at this value of $E_{\rm cm}$ (884 ± 44 nb^{-1}), and the "pure", *i.e.*, before radiative effects are included, cross-section for production of a charm resonance has been approximated by $\sigma_0^i(W) = A_i\delta(W - M_i)$; M_i is the mass of the resonance and A_i is its energy-integrated hadronic width. Treating the J/ψ and ψ' as narrow is well-justified; treating the ψ'' in this fashion is more questionable but is sufficient for the purposes here. For a Breit-Wigner lineshape, A_i is given by

$$A_i = \frac{6\pi^2}{M^2}\frac{\Gamma_{ee}^i\Gamma_{\rm had}^i}{\Gamma_{\rm tot}^i} \qquad [5.12]$$

$$= \frac{6\pi^2}{M^2}\Gamma_{ee}^i {\rm BR}(\psi_i \to {\rm hadrons}) \qquad [5.13]$$

where Γ_{ee}^i, $\Gamma_{\rm had}^i$, and $\Gamma_{\rm tot}^i$ are the electronic, hadronic, and total widths of resonance i, respectively.

The results for the three resonances J/ψ, ψ', and ψ'' are given in Table 5.1. Several hundred events to both the J/ψ and the ψ' are predicted. For the J/ψ, only "continuum-like" inclusive spectra is produced. For the ψ', the radiative transitions to the $\chi_{0,1,2}$ states occur,* but the Lorentz boost of the ψ' relative to

* See Fig. 1.4 for a non-Doppler-broadened illustration.

Resonance	Integrated Hadronic Width (nb-MeV)	Number of Radiative Events Expected	Radiative Photon Energy (MeV)
J/ψ	9700 ± 657	497 ± 42	823.5
ψ'	3490 ± 332	534 ± 57	327.5
ψ''	420 ± 242	86 ± 50	249.8

Table 5.1 Numbers of events expected, before efficiency corrections, from initial-state radiation to the charm resonances at $E_{\rm cm} = 4.028$ GeV. Also given are hadronic widths, calculated from values in Ref. 57, and the photon energy for single-photon emission to these states.

the lab, coupled with the branching ratios $\mathrm{BR}(\psi' \to \gamma\chi_i) \lesssim 9\%$ for each state, make the direct photon lines unobservable. Thus both resonances will contribute only featureless spectra and are included in the "continuum-like" sum.

It is possible to directly observe the photon created by the initial-state radiation. The energy expected for these photons is also given in Table 5.1. The efficiency for observing such a photon with energy E_γ is

$$\epsilon(E_\gamma) = \epsilon_{\rm had}\, \epsilon_\gamma\, \epsilon_{\rm geom}\,, \qquad [5.14].$$

where $\epsilon_{\rm had}$ is the efficiency for such an event to pass the hadron selection, and is estimated to be $95 \pm 5\%$; ϵ_γ is the photon detection efficiency, discussed in Section 4.2.3, and is $\approx 70\%$. The final efficiency is $\epsilon_{\rm geom}$, which indicates the convolution of the detector's geometric acceptance with the angular distribution of initial-state radiation;* it has been estimated in other studies[64] to be $\approx 15\%$.

---

* The approximate angular distribution is

$$\frac{d\sigma}{d\Omega} \propto \frac{\sin^2\theta}{\left(1 - \left(\frac{p}{E}\right)^2 \cos^2\theta\right)^2}$$

where $p(E)$ is the momentum(energy) of the electron or positron, and θ is angle to the beam direction of the emitted photon. The distribution is strongly peaked along the beam axis.

Thus the overall detection efficiency for such photons is $\epsilon(E_\gamma) \lesssim 9\%$. Indeed, no narrow structures are seen in Fig. 5.1 at any of the energies listed in the table.

In summary, no distinctive features are expected to be evident in the photon or pion inclusive spectra studied here, and initial-state radiation is expected to contribute only to the continuum-like sum.

5.3.3 *Processes Producing Charm Mesons*

The distributions for processes involving charm mesons are derived from Monte Carlo simulations. The processes involving charm strange mesons will be neglected since the D_S signal is expected to be much smaller than non-strange D-meson production at 4.028 GeV.* Each D^* decays via one of the processes

$$\begin{array}{lll} D^{*+} \to \pi^0 D^+ & & \\ D^{*+} \to \pi^+ D^0 & \text{or} & D^{*0} \to \pi^0 D^0 \\ D^{*+} \to \gamma D^+ & & D^{*0} \to \gamma D^0 \end{array} \qquad [5.15]$$

with $\overline{D}^*$'s decaying via the charge-conjugate mode. (The $D^{*\pm}$ branching ratios used in the Monte Carlo were fixed and are not determined in the present analysis; this is partly because the minimization algorithm has difficulty converging if there are too large a number of variable parameters, and because $\approx$ 50% of the charged $D^{*\pm}$'s will decay to charged pions leaving no characteristic signal in the inclusive energy distributions as neutral pions do, and therefore there is less sensitivity to $D^{*\pm}$ decays.) The values for $D^{*\pm}$ branching ratios were fixed

---

* The coupled-channel model of charm production[26-27] predicts the ratio of e^+e^- production cross-sections to be

$$\frac{\sigma(D_S^+ D_S^-)}{\sigma(D\overline{D}) + \sigma(D^*\overline{D} + D\overline{D}^*) + \sigma(D^*\overline{D}^*)} \approx 0.06\,;$$

additionally, the $D_S^+ D_S^-$ photon and neutral pion energy spectra are essentially indistinguishable from continuum or $D\overline{D}$ spectra. Any small contribution from D_S production will be absorbed in the cross-section sum for "continuum-like" processes.

at the values reported in the 1982 Particle Data Group summary;[71] when the 1984 summary[56] was released, the Monte Carlo processes were *not* rerun to include them because of insufficient availability of computer time. In any case, this change in $D^{*\pm}$ branching ratios† would have a small effect on the final results and is included as part of the systematic errors, in the result of this work.

In order to reduce further the number of free parameters in the minimizations, approximate isospin symmetry is invoked for $D\overline{D}$ and $D^*\overline{D} + D\overline{D}^*$ processes which, at $E_{\rm cm} = 4.028$ GeV, are well above the thresholds for their production. In $D\overline{D}$ production, the u and d quarks, being in the same SU(2) doublet, contribute equally to the matrix element for both charged and neutral modes. The only difference in production cross-sections then arises from the small ($\lesssim 3$ MeV) mass difference between charged and neutral partners; at $E_{\rm cm}$=4.028 GeV, the difference is $< 5\%$ and is not significant for this analysis. Making use of this, the relative amplitudes for $D^0\overline{D}^0$-and D^+D^- are set equal, as are the amplitudes for $D^{*0}\overline{D}^0 + D^0\overline{D}^{*0}$ and $D^{*+}D^- + D^+D^{*-}$. Additionally, the $D^{*+}D^{*-}$ component is neglected at $E_{\rm cm} = 4.028$ GeV; as mentioned above, the charged D^* leaves no characteristic signal when decaying via charged pions; also, since the charged D^*'s are more massive than the neutrals, there is a phase space suppression of their production near threshold with respect to the neutrals by the factor $(|\mathbf{p}_{D^{*\pm}}|/|\mathbf{p}_{D^{*0}}|)^3 = 0.4$; when combined with a branching ratio into photons or π^0's the $D^{*+}D^{*-}$ process enters with an amplitude $\lesssim 20\%$ of that of the neutral process and so will be omitted here.

Monte Carlo Simulation of D and D^* Processes

The charm meson event generator used in this work is a modified version of the constant-matrix-element model of Quigg and Rosner[60] which has had semi-leptonic decay modes[64] of the D^0 and $D^\pm$ included. Likewise, angular

† The changes were: BR($D^{*+} \to \pi^+ D^0$): $60 \pm 15\% \to 49 \pm 8\%$, BR($D^{*+} \to \pi^0 D^+$): $28 \pm 9\% \to 34 \pm 7\%$, and BR($D^{*+} \to \gamma D^0$): $8 \pm 7\% \to 17 \pm 11\%$.

matrix elements (in order to produce angular distributions and correlations for $D\overline{D}$, $D^*\overline{D} + D\overline{D}^*$, and $D^*\overline{D}^*$ production and decay) have been incorporated for this analysis. Kinematics fixes the production and decay angular distributions for $D\overline{D}$ and $D^*\overline{D} + D\overline{D}^*$ processes but not for $D^*\overline{D}^*$; this amplitude depends upon the ratio z of the spin-0 p-wave and spin-2 p-wave components: $z \equiv A_0/A_2$.* The value of z used in generating the Monte Carlo charm meson spectra was fixed at $z = -1/6$, the theoretically most-likely value.[14] The production amplitudes are:

$$\mathcal{M}_{D\overline{D}} \propto \hat{\eta} \cdot \hat{p} \qquad [5.16]$$

$$\mathcal{M}_{D^*\overline{D}+D\overline{D}^*} \propto \hat{\eta} \cdot \hat{p} \times \epsilon; \qquad [5.17]$$

$$\mathcal{M}_{D^*\overline{D}^*} \propto A_0\, \epsilon \cdot \bar{\epsilon} + A_2 \left(\frac{1}{2} \epsilon \cdot \hat{p}\, \epsilon \cdot \eta + \frac{1}{2} \epsilon \cdot \eta\, \bar{\epsilon} \cdot \hat{p} - \frac{1}{3} \epsilon \cdot \bar{\epsilon}\, \hat{p} \cdot \eta \right) \qquad [5.18]$$

where the following are three-vectors:†

$$\eta \equiv \text{virtual photon polarization;} \qquad [5.19]$$

$$\hat{p} \equiv \text{three-momentum of a primary } D \text{ or } D^*\text{; and} \qquad [5.20]$$

$$\epsilon\,(\bar{\epsilon}) \equiv D^*(\overline{D}^*) \text{ polarization vector.} \qquad [5.21]$$

These amplitudes are squared and the D^* polarization vectors summed to yield distributions for final state photons and π^0's from the D^* decay modes. After an initial meson pair has been produced and decayed into D's, π's, and photons, the D's are decayed via the constant-matrix-element Monte Carlo and phase space[67–68] considerations.

---

* The f-wave contribution is assumed to be small and is neglected. See Appendix B for a fuller discussion of angular matrix elements.

† Notation is essentially the same as in Ref. 14.

5.4 Corrections to Monte Carlo Photon Spectra at Low Energies

It has been observed during this analysis, and confirmed by others,[69] that the standard Crystal Ball detector simulation does not produce as many hadronic split-off showers as is seen in data. The detector simulation uses the HETC* routines[75] to simulate the energy deposition of interacting hadrons; however, this routine does not produce as many low-energy showers as are observed in the data. Other routines[76] are now available that could help eliminate this problem, such as FLUKA86 and GHEISHA;† however, because of time constraints, it was decided that a correction algorithm would be the best path to follow.

Determination of Shape Correction at the ψ''

The fitting technique outlined earlier was tested at the $\psi''(E_{\rm cm} = 3.772$ GeV) using only continuum, $D^0\overline{D}^0$, and D^+D^- components in the summation. In addition, the photon and π^0 energy spectra from Monte Carlo simulations of the D-related components were multiplied by energy-dependent polynomials before addition into the summation. The minimization algorithm adjusted the polynomial coefficients for the best fit, as well as the relative cross-sections of the physics processes. It was discovered that no correction was needed in the π^0 spectrum, presumably because the two-dimensional background subtraction technique discussed in Chapter 4 was able to remove the wrong combinatorics created by spurious "photons" during creation of these distributions. The correction polynomial for the photon spectra determined in this fashion is used in all summation fits at $E_{\rm cm} = 4.028$ GeV; indeed, without this split-off correction confidence levels for an entire summation fit are $\lesssim 0.1\%$, whereas the same fits with the correction applied have confidence levels $\gtrsim 18.6\%$. The "multiplicative shape correction polynomial" for photon spectra is displayed in Fig. 5.10.

---

* High Energy Transport Code.

† Actually the GHEISHA algorithm somewhat *overproduces* low-energy showers.

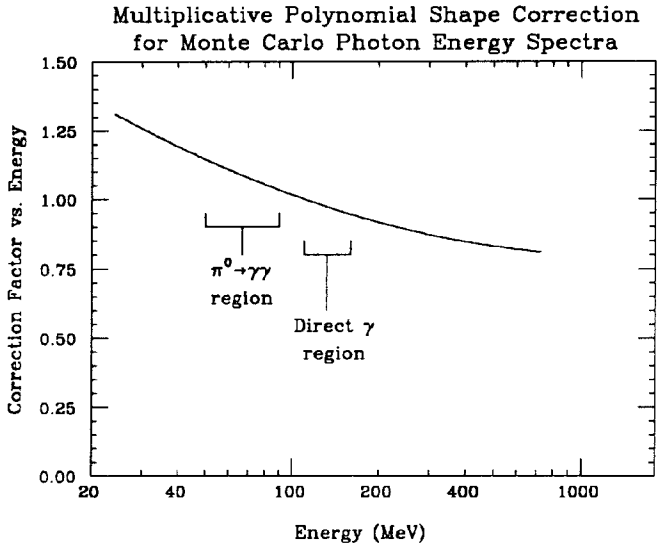

Fig. 5.10 The multiplicative shape correction polynomial (MPSC) used to correct missing split-off showers in Monte Carlo photon energy spectra. This boosts the counts in the low-energy bins of photon distributions.

Systematic Effects of the Shape Correction

The photon and pion peaks are sharp enough that no significant distortion is introduced from this correction. However, there may be a systematic effect resulting from the monotonic decrease of the correction factor with energy which slightly enhances the pion signal at the expense of the photon signal. The branching ratio measurement is particularly sensitive to this effect. The magnitude has been estimated using the polynomial shown in Fig. 5.10 to be $\lesssim 2.4\%$ for branching ratios in the range 50% to 80%.

5.5 Results of Measurements

5.5.1 *Introduction*

When performing the summation fits for each combination of D^0 mass and Δm, a "goodness-of-fit" value, distributed as a χ^2-variable, is obtained for each

Summation Fit Results at E_{cm} = 4.028 GeV					
		Δm			
		138.5 MeV	140.5 MeV	142.5 MeV	144.5 MeV
D^0 mass	1860.7 MeV	—	245.5	260.8	317.3
	1862.7 MeV	—	237.8	229.7	287.1
	1864.7 MeV	232.3	226.8	263.4	305.6
	1866.7 MeV	—	—	—	—
	1868.7 MeV	—	237.5	257.2	308.6

Table 5.2 The goodness-of-fit parameters from full summation fits at E_{cm} = 4.028 GeV as a function of D^0 mass and the Δm mass difference. The parameter values presented here are distributed at each mass combination as a χ^2-variable.

mass combination. These goodness-of-fit values are investigated as a function of the mass parameters to determine a measurement of the D^0 mass and Δm. Table 5.2 shows these resulting minima χ^2 for the full fitting process, for various steps in the D^0 mass *vs.* Δm matrix; some cells were not calculated because of time and cost constraints involved in running the source Monte Carlo simulations. Originally, a grid surrounding "standard values" of these two parameters was used, and it was expanded selectively when it became obvious that this high-precision measurement was converging to another matrix point. A global minimum is observed at the [$m(D^0)$ = 1864.7 MeV, Δm = 140.5 MeV] mass combination point. In the following sections, several fits to these local χ^2 minima near this point will be investigated. First, a fit to the values at constant Δm = 140.5 MeV will yield a D^0 mass measurement; second, a fit to the values at constant $m(D^0)$ = 1864.7 MeV will yield a measurement of Δm; third, a correlated fit using all the goodness-of-fit values will allow a correlated measurement of the two mass parameters. Following this, the branching ratio measurements at each mass combination are discussed. Lastly, the cross-section measurements

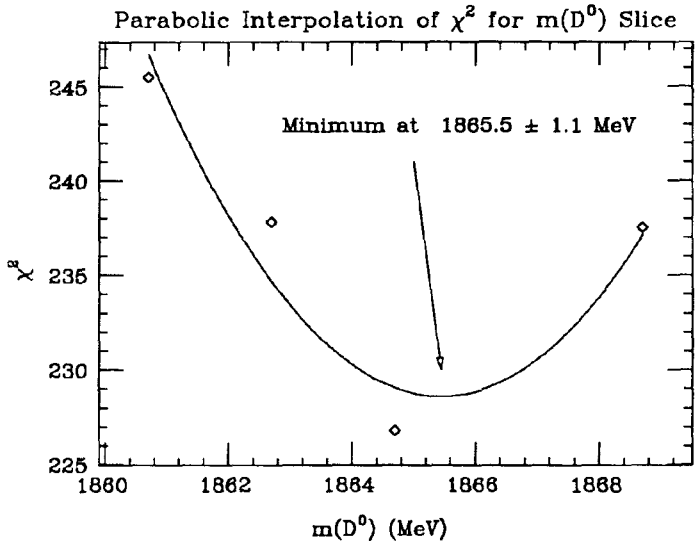

Fig. 5.11 A parabolic fit to the χ^2-distributed goodness-of-fit variable from Table 5.2 for constant Δm = 140.5 MeV. This fit, although instructive, must be interpreted as part of a two-dimensional fit with a strong negative correlation between the D^0 mass and the Δm mass difference. The minimum of the fitted function is at $m(D^0) = 1865.5 \pm 1.1 \pm 2.0$ MeV.

at the mass point closest to the correlated fit minimum are presented; however, it is to be stressed that these cross-section measurements are highly correlated and may have sizeable systematic errors.

5.5.2 D^0 and Δm Mass Measurements

The D^0 Mass and Δm Mass Difference—One-dimensional Fits

The simplest way of interpreting the χ^2 values in Table 5.2 is to perform one-dimensional fits of a parabolic function to the values along the row and column containing the minimum χ^2 value. These two fits are shown in Figs. 5.11 and 5.12. This of course neglects any possible correlation between the two mass

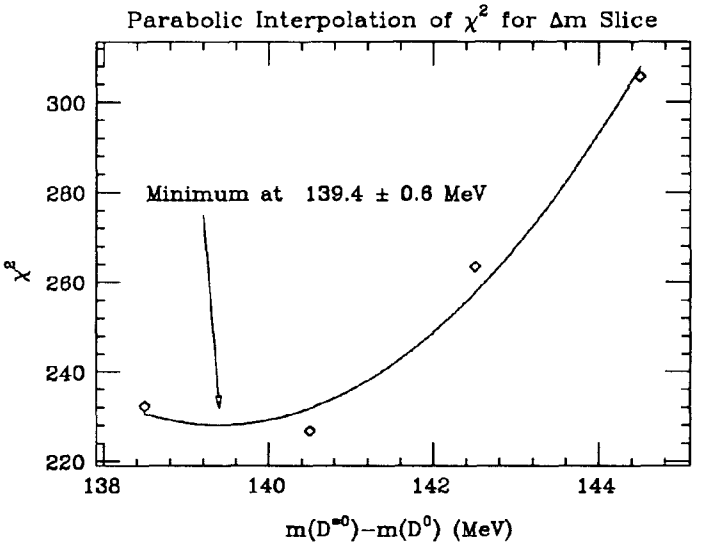

Fig. 5.12 A parabolic fit to the χ^2-distributed goodness-of-fit variable from Table 5.2 for constant $m(D^0) = 1864.7$ MeV. This fit, although instructive, must be interpreted as part of a two-dimensional fit with a strong negative correlation between the D^0 mass and the Δm mass difference. The minimum of the fitted function is at $\Delta m = 139.4 \pm 0.6 \pm 1.5$ MeV.

parameters. The values found this way are

$$m(D^0) = 1865.5 \ \pm 1.1 \pm 2.0 \text{ MeV} \qquad [5.22]$$

and

$$\Delta m = 139.4 \ \pm 0.6 \pm 1.5 \text{ MeV}, \qquad [5.23]$$

where the first error is statistical and the second is systematic.

The Correlation Between $m(D^0)$ and Δm.

The most general way of treating the χ^2 values obtained from the summation fits at the various mass combination points is to fit them using a two-dimensional binormal distribution function. The binormal distribution is the extension of the

parabolic fits of the preceding section to two dimensions. A fit of this nature will allow interpolation between the discrete mass points for determination of the minimum χ^2 point while accommodating a possible correlation between the two mass variables.

The binormal distribution function is[77]

$$B(x_1,x_2) = \frac{1}{1-\rho^2}\left[\left(\frac{x_1-\bar{x}_1}{\sigma_1}\right)^2 + \left(\frac{x_2-\bar{x}_2}{\sigma_2}\right)^2 - 2\rho\frac{(x_1-\bar{x}_1)(x_2-\bar{x}_2)}{\sigma_1\sigma_2}\right] \quad [5.24]$$

where x_1, x_2 are the independent variables, *e.g.*, masses, $\bar{x}_1$, $\bar{x}_2$ are the values where the minimum of B occurs, σ_1, σ_2 are "one-standard deviation" statistical errors determined by the curvature of B, and ρ is the correlation coefficient of x_1 and x_2.* A contour plot of the binormal surface is shown in Fig. 5.13. The coordinates of the minimum are at

$$m(D^0) = 1865.3 \pm 1.0 \pm 2.0 \text{ MeV} \quad [5.26]$$

and

$$\Delta m = 140.0 \pm 0.5 \pm 1.5 \text{ MeV}, \quad [5.27]$$

where the first error is statistical and the second is systematic. The correlation coefficient is $\rho = -0.30$. These values are seen to be quite consistent with those from the one-dimensional parabolic fits. The systematic error is considered to be a conservative estimate. Further studies may be able to reduce it.

In performing the fit to the binormal function, the two χ^2 values from the mass points $[\Delta m,\ m(D^0)] = [142.5 \text{ MeV}, 1868.7 \text{ MeV}]$ and [144.5 MeV,

---

* The correlation coefficient is related to the angle α that the major principle axis of a B = constant ellipse makes with one of the independent axes. It is given by

$$\tan 2\alpha = 2\rho\frac{\sigma_1\sigma_2}{\sigma_1^2-\sigma_2^2}. \quad [5.25]$$

For the fit in Fig. 5.13, $\alpha = 12.6°$.

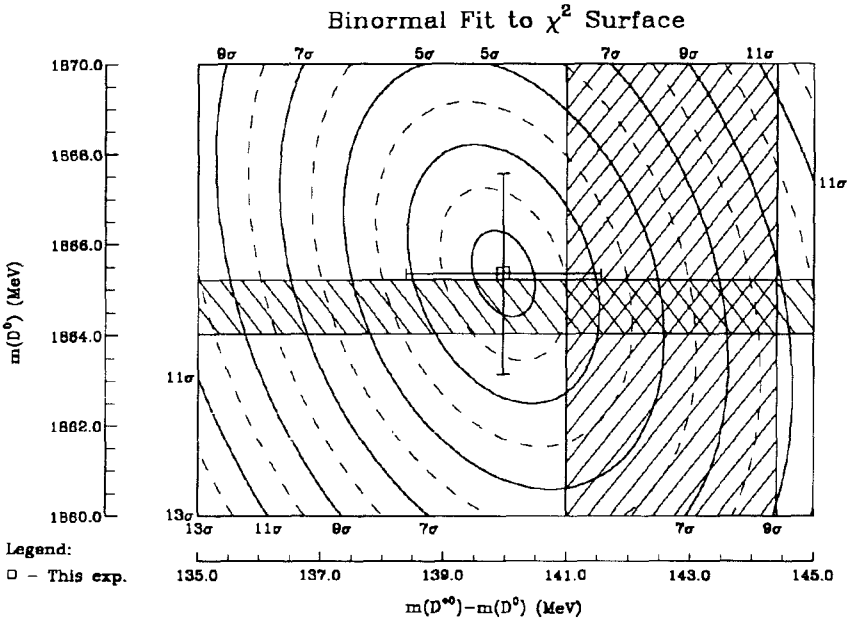

Fig. 5.13 Contour plot of a binormal surface fitted to the χ^2 local minima obtained in summation fits at each D^0 mass and Δm combination. The minimum, indicated by the '□', occurs at $m(D^0) = 1865.3 \pm 1.0 \pm 2.0$ MeV and $\Delta m = 140.0 \pm 0.5 \pm 1.5$ MeV (first error is statistical, second is systematic). The standard deviation contours reflect only statistical errors; the error bars represent $\pm 1\sigma$ statistical errors combined in quadrature with a 1.5 MeV systematic error in Δm and a 2.0 MeV systematic in $m(D^0)$. The correlation coefficient is $\rho = -0.30$. The horizontal band indicates the $\pm 1\sigma$ errors about the world average value for $m(D^0)$; the vertical band indicates the same for the world average for Δm.[57]

1868.7 MeV] were not included in the fit. These two points, at large extremes from the minimum, have cross-section values for $D^*\overline{D} + D\overline{D}^*$ and $D^*\overline{D}^*$ processes that are quite different from those found nearer the minimum. Physically, at these large mass values, the Doppler-widened signal from the initial π^0 decay has become so broad that no $D^*\overline{D} + D\overline{D}^*$ component is allowed in the fit; all the amplitude is attributed to $D^*\overline{D}^*$ production. This is inconsistent with the relatively constant cross-section values found nearer the minimum, and these points

Summation Fit Results for BR($D^{*0} \to \pi^0 D^0$) (%)					
		Δm			
		138.5 MeV	140.5 MeV	142.5 MeV	144.5 MeV
D^0 mass	1860.7 MeV	—	54.8 ± 3.0	58.3 ± 3.3	57.0 ± 3.4
	1862.7 MeV	—	54.8 ± 3.5	57.5 ± 3.2	53.2 ± 3.9
	1864.7 MeV	46.1 ± 3.3	53.1 ± 3.4	55.7 ± 3.6	48.1 ± 3.8
	1866.7 MeV	—	—	—	—
	1868.7 MeV	—	49.5 ± 3.4	53.0 ± 3.8	44.9 ± 4.9

Table 5.9 The values for BR($D^{*0} \to \pi^0 D^0$) found in the summation fits at E_{cm} = 4.028 GeV as a function of D^0 mass and the Δm mass difference. The values are stable near 50% even though there is considerable variation in the "goodness-of-fit" parameter over the range of mass combinations considered (see Table 5.2).

distort the shape of the binormal function if included.†

5.5.3 *The Branching Ratio BR($D^{*0} \to \pi^0 D^0$)*

The results of the branching ratio measurements as a function of mass combination are given in Table 5.3. The branching ratio values found at the different mass combinations are stable, varying from 45% to 59%; the value measured at the grid point having the lowest local minimum in χ^2 is

$$\mathrm{BR}(D^{*0} \to \pi^0 D^0) = 53.1 \pm 3.4 \pm 9.1\%, \qquad [5.28]$$

which yields

$$\mathrm{BR}(D^{*0} \to \gamma D^0) = 46.9 \pm 3.4 \pm 9.1\%, \qquad [5.29]$$

where the first error is statistical and the second is systematic. The statisti-

† When these two points are included, it is found that $\Delta m = 140.1 \pm 0.5$ MeV and $m(D^0) = 1865.3 \pm 1.1$ MeV (statistical errors only); the correlation coefficient becomes $\rho = -0.09$.

cal error is estimated by the minimization algorithm, including the possible occurence of non-parabolic errors. The systematic error is a conservative estimate calculated from several possible perturbations added in quadrature. First, the estimated effect of the omission of $D^{*+}D^{*-}$ in the fits is 5%; second, the variation of the branching ratio over the region where the χ^2 values are compatible with a binormal interpretation (this excludes the two mass points mentioned in the previous section) gives an estimate of 7.2% for the uncertainty from errors in spectrum shapes; and third, a systematic effect from the polynomial shape correction (discussed above) of 2.4% is included. This result may be compared with the world average of $51.5 \pm 7.6\%$.

5.5.4 *Combination with Other Experiments*

When this experiment's correlated Δm value of $140.0 \pm 0.5 \pm 1.5$ MeV is combined with the only other independent result, 142.7 ± 1.7 MeV,[18] the weighted average is

$$\Delta m|_{\substack{\text{world}\\\text{average}}} = 141.3 \pm 1.2 \text{ MeV}. \qquad [5.30]$$

The confidence level of the consistency of these two mass difference measurements is 51.1%.

When the pion branching ratio of this work, $53.1 \pm 3.4 \pm 9.1\%$, is combined with the current world average of $51.5 \pm 7.6\%$,[57] the combined result is

$$\text{BR}(D^{*0} \to \pi^0 D^0)\big|_{\substack{\text{world}\\\text{average}}} = 52.3 \pm 5.4\%, \qquad [5.31]$$

and

$$\text{BR}(D^{*0} \to \gamma D^0)\big|_{\substack{\text{world}\\\text{average}}} = 47.7 \pm 5.4\%. \qquad [5.32]$$

Cross-sections for Charm Meson Production at $E_{cm} = 4.028$ GeV.		
Process(es)	σ (nb)	Units of R
Sum of non-charm, $D^0\overline{D}^0$, and D^+D^-	23	4.4
$D^{*0}\overline{D}^0 + D^0\overline{D}^{*0}$	3.4	0.64
$D^{*+}D^- + D^+D^{*-}$	3.4	0.64
$D^{*0}\overline{D}^{*0}$	1.8	0.33
Total	31.6	6.01

Table 5.4 Cross-sections as measured in the summation fit nearest the correlated minimum in D^0 mass and Δm. These values are correlated and have large systematic errors. They are included here only to indicate typical values found in this analysis. No radiative corrections have been applied.

5.5.5 *Charm Meson Cross-Sections at* $E_{cm} = 4.028$ *GeV*

The cross-sections for charm meson production found at the mass combination closest to the correlated fit minimum are given in Table 5.4. They are included here for completeness only; no values indicating the precision of these measurements are quoted since there would be unknown systematic errors involved. The largest source of these systematics is the difference between multiplicities of each process contributing to the data, and its counterpart from Monte Carlo simulation. This is only a "second-order" effect in calculations of branching ratios or mass measurements, but is a "first-order" effect in direct calculations of the cross-sections. Also, the three processes (1) non-charm, (2) $D^0\overline{D}^0$, and (3) D^+D^- production are indicated as a single sum since the spectra representing the three processes are very similar and cannot be separated by the summation fit procedure. A comparison of these cross-section results and the coupled-channel model is given in Chapter 1.

Appendix A

Angular Distributions in D and D^* Decays

A.1 Introduction

This appendix discusses the calculation of the angular parts of cross-sections used in this analysis. The combined production-and-decay cross-sections calculated here are used in the event generator for charm meson production which, when used with the detector simulation algorithm, is the basis for the Monte Carlo spectra used to fit for charm meson masses and branching ratios. Throughout this appendix the terms "cross-section" and "matrix element" refer only to the angular parts of the complete expression. Most calculations are done non-relativistically following Ref. 14; since we are interested only in $D^*\overline{D}^*$ production very near threshold, this is sufficient. Relativistic effects are included when necessary (for instance in $D^*\overline{D} + D\overline{D}^*$ production).

Section 2 of this appendix defines notation and lists some useful relations for integrating over various quantities. Sections 3 and 4 discuss $D\overline{D}$ and $D^*\overline{D} + D\overline{D}^*$ production cross-sections respectively and their combination with D^* pion and photon decay matrix elements. Section 5 presents the cross-sections for $D^*\overline{D}^*$ production and decay. The more lengthy of the following cross-section calculations were performed with the aid of the symbolic manipulation program REDUCE.[78]

A.2 Definitions and Identities

The following are definitions for the momentum and polarization vectors encountered in charm meson production and decay (quantities marked with a '$\hat{}$' indicate unit vectors):

$\hat{p}$ = three-vector in the direction of the D^* momentum;

$\hat{q}$ = three-vector in the direction of the π three-momentum, where the π is produced in $D^* \rightarrow \pi D$;

$\hat{k}$ = three-vector in the direction of the γ three-momentum, where the γ is produced in $D^* \rightarrow \gamma D$;

$\hat{n}$ = three-vector in the direction of the e^+-beam;

η = polarization vector of the virtual photon, γ^*, in $e^+e^- \rightarrow \gamma^* \rightarrow c\bar{c}$; and

$\epsilon(\bar{\epsilon})$ = polarization vector of the $D^*(\overline{D}^*)$.

In some cases, more than one pion or photon may be present in the process; then the three-vectors will be distinguished by subscripts, *e.g.*, $\hat{k}_1$ and $\hat{k}_2$.

The identities below are used in summations over various quantities including virtual photon polarizations, D^* polarizations, and integrals over three-momenta angles (subscripts here refer to coordinate labels, *e.g.*, x, y, and z, not to particle labels—see above). First there are the summations over virtual photon polarizations in $e^+e^- \rightarrow \gamma^* \rightarrow$ charm meson pairs: polarization to the e^+-beam direction and transversality yield

$$\sum_{\gamma^* \text{ pol}} \eta_i \eta_j = \delta_{ij} - \hat{n}_i \hat{n}_j \qquad [A.1]$$

and

$$\sum_{\gamma^* \text{ pol}} A = 2A \qquad [A.2]$$

where A is any expression not involving the polarization vector η. For the D^*, a spin-1 massive object, we have the polarization sum

$$\sum_{D^* \text{ pol}} \epsilon_i \epsilon_j = \delta_{ij} \,, \qquad [A.3]$$

and the solid-angle integration relation

$$\sum_{\text{angles}} \hat{p}_i \hat{p}_j = \frac{1}{3} \delta_{ij} \,. \qquad [A.4]$$

which is equivalent to

$$\int d\Omega_p \, \hat{p}_i \hat{p}_j = \frac{1}{3} \delta_{ij} \,. \qquad [A.5]$$

If the beam direction is averaged over, we can use the relation

$$\sum_{\substack{\text{beam} \\ \text{directions}}} \hat{n}_i \hat{n}_j = \frac{1}{3} \delta_{ij} \,. \qquad [A.6]$$

In these relations we use the standard Krönecker δ-function

$$\delta_{ij} = \begin{cases} +1 & \text{for } i = j; \\ 0 & \text{for } i \neq j, \end{cases}$$

and the fully antisymmetric quantity

$$\varepsilon_{ijk} = \begin{cases} +1 & \text{for } ijk \text{ an even permutation of 123;} \\ -1 & \text{for } ijk \text{ an odd permutation of 123; and} \\ 0 & \text{for any two indices equal.} \end{cases}$$

Recall that the vector cross-product can be written as

$$(\mathbf{A} \times \mathbf{B})_i = \varepsilon_{ijk} \, A_j B_k \,, \qquad [A.7]$$

and the identity

$$\varepsilon_{ijk} \, \varepsilon_{ilm} = \delta_{jl} \delta_{km} - \delta_{jm} \delta_{kl} \,. \qquad [A.8]$$

A.3 $D\overline{D}$ Production

Let $\hat{p}$ denote the D three-momentum unit vector. The angular part of the matrix element is simply*

$$\mathcal{M}_{D\overline{D}} \propto \eta \cdot \hat{p}\,, \qquad [A.9]$$

where $\hat{p}$ is measured in the e^+e^- center-of-mass frame. From this we see that

$$\begin{aligned} \frac{d\sigma}{d\Omega_{(D\overline{D})}} &\propto |\mathcal{M}|^2 \\ &\propto \eta_i \hat{p}_i \, \eta_j \hat{p}_j\,, \end{aligned} \qquad [A.10]$$

and by Eq. [A.1],

$$\begin{aligned} \frac{d\sigma}{d\Omega_{(D\overline{D})}} &\propto (\delta_{ij} - \hat{n}_i \hat{n}_j)\, \hat{p}_i \hat{p}_j \\ &\propto \hat{p}_i \hat{p}_i - \hat{n}_i \hat{p}_i \, \hat{n}_j \hat{p}_j \\ &\propto 1 - (\hat{n} \cdot \hat{p})^2\,. \end{aligned} \qquad [A.11]$$

Defining the polar angle of the D to the beam axis to be θ, so that $\cos\theta = \hat{n} \cdot \hat{p}$, we see that the polar angular distribution is

$$\frac{d\sigma}{d\Omega_{(D\overline{D})}} \propto \sin^2\theta\,. \qquad [A.12]$$

This remains true in the relativistic calculation.

---

* All matrix elements are from Ref. 14.

A.4 $D^*\overline{D} + D\overline{D}^*$ Production and Decay

The production matrix element for $D^*\overline{D}$ production is[†]

$$\mathcal{M}_{D^*\overline{D}} \propto \eta \cdot \hat{p} \times \epsilon . \qquad [A.13]$$

Squaring this and summing over virtual photon polarizations using Eq. [A.1], and using Eq. [A.7] to express the cross-product, we get the $D^*\overline{D}$ production cross section:

$$\frac{d\sigma}{d\Omega_{(D^*\overline{D})}} \propto 1 - (\hat{p} \cdot \epsilon)^2 - (\hat{n} \cdot (\hat{p} \times \epsilon))^2 \qquad [A.14]$$

where ϵ is the D^* polarization vector. If the D^* polarization is not observed, we can eliminate ϵ using Eq. [A.3]:

$$\frac{d\sigma}{d\Omega_{(D^*\overline{D})}} \propto 1 + (\hat{p} \cdot \hat{n})^2 . \qquad [A.15]$$

If we again let θ be the polar angle of the D^* relative to the beam, so that $\cos\theta = \hat{n} \cdot \hat{p}$, we see that the angular distribution is (non-relativistically)

$$\frac{d\sigma}{d\Omega_{(D^*\overline{D})}} \propto 1 + \cos^2\theta . \qquad [A.16]$$

In order to calculate the combined production and decay cross-sections, we will need the D^* decay matrix elements for the photonic and pionic decays. These are:

$$\mathcal{M}_{D^* \to \pi D} \propto \epsilon \cdot \hat{q} , \text{ and} \qquad [A.17]$$

$$\mathcal{M}_{D^* \to \gamma D} \propto \epsilon \cdot (\hat{k} \times \hat{E}) = \epsilon \cdot \hat{B} \qquad [A.18]$$

---

† For the remainder of this discussion, the expression $D^*\overline{D}$ will be understood to represent $D^*\overline{D} + D\overline{D}^*$.

where $\hat{q}(\hat{k})$ is the pion(photon) three-momentum unit vector, and $\hat{B}$ is the magnetic polarization vector of the emitted photon. For this photon, a polarization sum similar to Eq. [A.1] can be written:

$$\sum_{\substack{\text{magnetic} \\ \text{polarizations}}} \hat{B}_i \hat{B}_j = \delta_{ij} - \hat{k}_i \hat{k}_j \,. \qquad \text{[A.19]}$$

The Pionic Decay $D^*\overline{D} \to \pi D\overline{D}$

Making use of Eqs. [A.14] and [A.17], and identity [A.3] to sum over the D^* polarization, we find for the pionic decay

$$\frac{d\sigma}{d\Omega_{(D^*\overline{D}\to\pi D\overline{D})}} \propto 1 - (\hat{p}\cdot\hat{q})^2 - (\hat{n}\cdot(\hat{p}\times\hat{q}))^2 \,. \qquad \text{[A.20]}$$

If the D^* direction is not observed (or equivalently the D direction), then using Eq. [A.4], we find

$$\frac{d\sigma}{d\Omega_{(D^*\overline{D}\to\pi D\overline{D})}} \propto 1 + (\hat{q}\cdot\hat{n})^2 \qquad \text{[A.21]}$$

which yields a $1+\cos^2\theta_\pi$ inclusive distribution for the pion if it alone is observed ($\theta_\pi \equiv \hat{q}\cdot\hat{n}$).

The Photonic Decay $D^*\overline{D} \to \gamma D\overline{D}$

Similarly for the photonic decay, using Eqs. [A.14], [A.18], and [A.19], we find that

$$\frac{d\sigma}{d\Omega_{(D^*\overline{D}\to\gamma D\overline{D})}} \propto (\hat{p}\cdot\hat{k})^2 + (\hat{p}\cdot\hat{n})^2 + (\hat{n}\cdot(\hat{p}\times\hat{k}))^2 \,. \qquad \text{[A.22]}$$

If the D^* direction is integrated over, using Eqs. [A.4] and [A.8], we find that the inclusive photon distribution is

$$\frac{d\sigma}{d\Omega_{(D^*\overline{D}\to\gamma D\overline{D})}} \propto 1 - \frac{1}{3}(\hat{k}\cdot\hat{n})^2 \,. \qquad \text{[A.23]}$$

A.5 $D^*\overline{D}^*$ Production and Decay

The production matrix element for $D^*\overline{D}^*$ production is

$$\mathcal{M}_{D^*\overline{D}^*} \propto A_0(\epsilon\cdot\bar{\epsilon})(\eta\cdot\hat{p}) + A_2\left(\frac{1}{2}(\epsilon\cdot\hat{p})(\bar{\epsilon}\cdot\eta) + \frac{1}{2}(\eta\cdot\epsilon)(\hat{p}\cdot\bar{\epsilon}) - \frac{1}{3}(\hat{p}\cdot\eta)(\epsilon\cdot\bar{\epsilon})\right). \quad [A.24]$$

As in the preceding section, various angular distributions could be calculated using this matrix element and the decay matrix elements above by integrating over the D^* or the $\overline{D}^*$ polarizations and directions, pion or photon directions, photon polarizations, and so forth. These are instructive but not necessary for our purpose here, so these expressions will not be discussed; instead, the final expressions for angular distributions for $D^*\overline{D}^*$ production and decay that were used in the Monte Carlo are given directly below.

The Double-Pion Decay $D^*\overline{D}^* \to \pi\pi D\overline{D}$

Starting from the matrix element in Eq. [A.24], and using Eq. [A.17] twice, we get the result

$$\begin{aligned}\frac{d\sigma}{d\Omega_{(D^*\overline{D}^*\to\pi\pi D\overline{D})}} \propto & A_0^2(\hat{q}_1\cdot\hat{q}_2)^2\left(1-(\hat{p}\cdot\hat{n})^2\right) \\ & + 2A_0A_2(\hat{q}_1\cdot\hat{q}_2)\left[(\hat{q}_1\cdot\hat{p})(\hat{q}_2\cdot\hat{p}) - \frac{1}{3}(\hat{q}_1\cdot\hat{q}_2) + (\hat{p}\cdot\hat{n})\right. \\ & \left.\times\left(\frac{1}{3}(\hat{q}_1\cdot\hat{q}_2)(\hat{p}\cdot\hat{n}) - \frac{1}{2}(\hat{q}_1\cdot\hat{p})(\hat{q}_2\cdot\hat{n}) - \frac{1}{2}(\hat{q}_2\cdot\hat{p})(\hat{q}_1\cdot\hat{n})\right)\right] \\ & + A_2^2\left(\frac{1}{4}(\hat{q}_1\cdot\hat{p})^2 + \frac{1}{4}(\hat{q}_2\cdot\hat{p})^2 + \frac{1}{9}(\hat{q}_1\cdot\hat{q}_2)^2 - \frac{1}{4}(\hat{q}_1\cdot\hat{p})^2(\hat{q}_2\cdot\hat{n})^2\right. \\ & \quad - \frac{1}{4}(\hat{q}_1\cdot\hat{n})^2(\hat{q}_2\cdot\hat{p})^2 - \frac{1}{9}(\hat{q}_1\cdot\hat{q}_2)^2(\hat{p}\cdot\hat{n})^2 \\ & \quad - \frac{1}{6}(\hat{q}_1\cdot\hat{p})(\hat{q}_2\cdot\hat{p})(\hat{q}_1\cdot\hat{q}_2) - \frac{1}{2}(\hat{q}_1\cdot\hat{p})(\hat{q}_2\cdot\hat{n})(\hat{q}_1\cdot\hat{n})(\hat{q}_2\cdot\hat{p}) \\ & \quad \left.+ \frac{1}{3}(\hat{q}_1\cdot\hat{p})(\hat{q}_2\cdot\hat{n})(\hat{q}_1\cdot\hat{q}_2)(\hat{p}\cdot\hat{n})\right)\end{aligned}$$

$$+\frac{1}{3}(\hat{q}_1\cdot\hat{n})(\hat{q}_2\cdot\hat{p})(\hat{q}_1\cdot\hat{q}_2)(\hat{p}\cdot\hat{n})\Big)\,. \qquad [A.25]$$

The Pion-Photon Decay $D^*\overline{D}^*\to\pi\gamma D\overline{D}$

Starting from the matrix element in Eq. [A.24], and using Eqs. [A.17] and [A.18], we find that

$$\begin{aligned}\frac{d\sigma}{d\Omega}_{(D^*\overline{D}^*\to\pi\gamma D\overline{D})} \propto A_0^2&\left(1-(\hat{q}\cdot\hat{k})^2-(\hat{p}\cdot\hat{n})^2+(\hat{q}\cdot\hat{k})^2(\hat{p}\cdot\hat{n})^2\right)\\
&+2A_0A_2\left[-\frac{1}{3}+(\hat{q}\cdot\hat{p})^2+\frac{1}{3}(\hat{q}\cdot\hat{k})^2+\frac{1}{3}(\hat{p}\cdot\hat{n})^2-\frac{1}{3}(\hat{q}\cdot\hat{k})^2(\hat{p}\cdot\hat{n})^2\right.\\
&\quad-(\hat{q}\cdot\hat{k})(\hat{k}\cdot\hat{p})(\hat{q}\cdot\hat{p})-(\hat{q}\cdot\hat{p})(\hat{q}\cdot\hat{n})(\hat{p}\cdot\hat{n})\\
&\quad\left.+\frac{1}{2}(\hat{q}\cdot\hat{k})(\hat{p}\cdot\hat{n})\left((\hat{k}\cdot\hat{p})(\hat{q}\cdot\hat{n})+(\hat{k}\cdot\hat{n})(\hat{q}\cdot\hat{p})\right)\right]\\
&+A_2^2\left(\frac{13}{36}-\frac{1}{4}(\hat{k}\cdot\hat{p})^2-\frac{1}{4}(\hat{q}\cdot\hat{n})^2+\frac{1}{12}(\hat{q}\cdot\hat{p})^2\right.\\
&\quad-\frac{1}{9}(\hat{q}\cdot\hat{k})^2-\frac{1}{9}(\hat{p}\cdot\hat{n})^2+\frac{1}{4}(\hat{k}\cdot\hat{p})^2(\hat{q}\cdot\hat{n})^2\\
&\quad+\frac{1}{4}(\hat{k}\cdot\hat{n})^2(\hat{q}\cdot\hat{p})^2+\frac{1}{9}(\hat{q}\cdot\hat{k})^2(\hat{p}\cdot\hat{n})^2+\frac{1}{6}(\hat{k}\cdot\hat{p})(\hat{q}\cdot\hat{k})(\hat{q}\cdot\hat{p})\\
&\quad+\frac{1}{6}(\hat{p}\cdot\hat{n})(\hat{q}\cdot\hat{n})(\hat{q}\cdot\hat{p})+\frac{1}{2}(\hat{k}\cdot\hat{p})(\hat{k}\cdot\hat{n})(\hat{q}\cdot\hat{n})(\hat{q}\cdot\hat{p})\\
&\quad-\frac{1}{3}(\hat{k}\cdot\hat{p})(\hat{q}\cdot\hat{k})(\hat{q}\cdot\hat{n})(\hat{p}\cdot\hat{n})\\
&\quad\left.-\frac{1}{3}(\hat{k}\cdot\hat{n})(\hat{q}\cdot\hat{k})(\hat{q}\cdot\hat{p})(\hat{p}\cdot\hat{n})\right) \qquad [A.26]\end{aligned}$$

The Double-Photon Decay $D^*\overline{D}^*\to\gamma\gamma D\overline{D}$

Again starting from the matrix element in Eq. [A.24], and using Eq. [A.18]

twice, we get the result

$$\begin{aligned}
\frac{d\sigma}{d\Omega_{(D^*\overline{D}^*\to\gamma\gamma D\overline{D})}} \propto & A_0^2\left(-(\hat{p}\cdot\hat{n})^2+(\hat{k}_1\cdot\hat{k}_2)^2-(\hat{k}_1\cdot\hat{k}_2)^2(\hat{p}\cdot\hat{n})^2\right)\\
& + A_0A_2\left[\frac{4}{3}\left(1-(\hat{p}\cdot\hat{n})^2\right)-\frac{2}{3}(\hat{k}_1\cdot\hat{k}_2)^2-2\left((\hat{k}_1\cdot\hat{p})^2+(\hat{k}_2\cdot\hat{p})^2\right)\right.\\
& \quad +\frac{2}{3}(\hat{k}_1\cdot\hat{k}_2)^2(\hat{p}\cdot\hat{n})^2+2(\hat{p}\cdot\hat{n})\left((\hat{k}_1\cdot\hat{n})(\hat{k}_1\cdot\hat{p})\right.\\
& \quad \left.+(\hat{k}_2\cdot\hat{n})(\hat{k}_2\cdot\hat{p})\right)+2(\hat{k}_1\cdot\hat{k}_2)(\hat{k}_1\cdot\hat{p})(\hat{k}_2\cdot\hat{p})\\
& \quad \left.-(\hat{k}_1\cdot\hat{k}_2)(\hat{p}\cdot\hat{n})\left((\hat{k}_1\cdot\hat{n})(\hat{k}_2\cdot\hat{p})+(\hat{k}_2\cdot\hat{n})(\hat{k}_1\cdot\hat{p})\right)\right]\\
& + A_2^2\left[\frac{4}{9}+\frac{1}{18}(\hat{p}\cdot\hat{n})^2+\frac{1}{9}(\hat{k}_1\cdot\hat{k}_2)^2\left(1-(\hat{p}\cdot\hat{n})^2\right)\right.\\
& \quad -\frac{1}{12}\left((\hat{k}_1\cdot\hat{p})^2+(\hat{k}_2\cdot\hat{p})^2\right)+\frac{1}{4}\left((\hat{k}_1\cdot\hat{n})^2+(\hat{k}_2\cdot\hat{n})^2\right)\\
& \quad -\frac{1}{6}(\hat{p}\cdot\hat{n})\left((\hat{k}_1\cdot\hat{n})(\hat{k}_1\cdot\hat{p})+(\hat{k}_2\cdot\hat{n})(\hat{k}_2\cdot\hat{p})\right)\\
& \quad -\frac{1}{6}(\hat{k}_1\cdot\hat{k}_2)(\hat{k}_1\cdot\hat{p})(\hat{k}_2\cdot\hat{p})\\
& \quad -\frac{1}{4}\left((\hat{k}_1\cdot\hat{n})^2(\hat{k}_2\cdot\hat{p})^2+(\hat{k}_1\cdot\hat{p})^2(\hat{k}_2\cdot\hat{n})^2\right)\\
& \quad +\frac{1}{3}(\hat{k}_1\cdot\hat{k}_2)(\hat{p}\cdot\hat{n})\left((\hat{k}_1\cdot\hat{n})(\hat{k}_2\cdot\hat{p})+(\hat{k}_1\cdot\hat{p})(\hat{k}_2\cdot\hat{n})\right)\\
& \quad \left.-\frac{1}{2}(\hat{k}_1\cdot\hat{n})(\hat{k}_1\cdot\hat{p})(\hat{k}_2\cdot\hat{n})(\hat{k}_2\cdot\hat{p})\right] \qquad \text{[A.27]}
\end{aligned}$$

A.5.1 *The Parameters A_0 and A_2*

The expression for the $D^*\overline{D}^*$ matrix element, Eq. [A.13], involves the amplitudes A_0 and A_2 (a possible F-wave component has been neglected). Only the ratio $z = A_0/A_2$ is observable. There is only limited experimental evidence for the value of z.* In place of an experimental determination, we have used

* Ref. 79 gives $|z|^2 < 0.51$.

$z = -1/6$ for all $D^*\overline{D}^*$ Monte Carlo events generated for this analysis. Cahn and Kayser, in Ref. 14, state that this value is predicted by theory if one assumes the resonance is a $3\,^3S_1$ state, and that the spin of the light quarks is not strongly correlated with the spin of the charm quarks.

A.6 Relativistic Corrections

The distributions for $D^*\overline{D}^*$ production and decay presented above are non-relativistic approximations. However, these are sufficient for our purposes because we are studying these processes only 10 MeV above threshold; the D^*'s are moving slowly. Also, the distribution for $D\overline{D}$ production is sufficient; it remains the same in a relativistic calculation. However, the distributions for $D^*\overline{D}$ must be corrected since we are working $\sim$ 150 MeV above threshold for this meson combination.

Cahn and Kayser have calculated these effects. In essence, the angular distributions now include terms involving the energies of the decay pion or photon. For the pionic decay, the distribution is

$$\frac{d\sigma}{d\Omega}^{\rm rel}_{(D^*\overline{D}\to\pi D\overline{D})} \propto \left(1-(\hat{q}\cdot\hat{n})^2\right)|\mathbf{q}|^2\left(1-(\hat{q}\cdot\hat{p})^2\right) \qquad \text{[A.28]}$$

This is the generalization of Eq. [A.20]. For the photon decay, the distribution is

$$\begin{aligned}\frac{d\sigma}{d\Omega}^{\rm rel}_{(D^*\overline{D}\to\gamma D\overline{D})} \propto |\mathbf{k}|^2 \Big\{ &\left[\left(1-(\hat{k}\cdot\hat{n})^2\right)+2(\hat{k}\cdot\hat{n})^2(\hat{k}\cdot\hat{p})^2\right] \\ &-\beta_{D^*}\hat{k}\cdot\hat{p}\left[\left(3-(\hat{k}\cdot\hat{n})^2\right)-\left(1-3(\hat{k}\cdot\hat{n})^2\right)(\hat{k}\cdot\hat{p})^2\right] \\ &+\frac{1}{2}\beta_{D^*}^2\Big[\left(1+(\hat{k}\cdot\hat{n})^2\right)+2\left(1-(\hat{k}\cdot\hat{n})^2\right)(\hat{k}\cdot\hat{p})^2 \\ &\qquad -\left(1-3(\hat{k}\cdot\hat{n})^2\right)(\hat{k}\cdot\hat{p})^4\Big]\Big\} \qquad \text{[A.29]}\end{aligned}$$

This is the corrected version of Eq. [A.22]. Eqs. [A.28] and [A.29] are used in the Monte Carlo event generator.

References

1) S. Glashow, J. Iliopoulos, and J. Maiani, *Weak Interactions with Lepton Hadron Symmetry*, *Phys. Rev.* **D2**, 1285 (1970).

2) T. Appelquist and H. Politzer, *Heavy Quarks and e^+e^- Annihilation*, *Phys. Rev. Lett.* **34**, 43 (1975).

3) M. K. Gaillard, B. W. Lee, and J.L. Rosner, *Search for Charm*, *Rev. of Mod. Phys.* **47**, 277 (1975).

4) T. Appelquist, R. M. Barnett, and K. Lane, *Charm and Beyond*, *Ann. Rev. Nucl. Part. Sci.* **28**, 387 (1978).

5) T. Appelquist, A. de Rujula, H. Politzer, and S. Glashow, *Charmonium Spectroscopy*, *Phys. Rev. Lett.* **34**, 365 (1975).

6) J. Aubert *et al.*, *Experimental Observation of a Heavy Particle J*, *Phys. Rev. Lett.* **33**, 1404 (1974).

7) J.-E. Augustin *et al.*, *Discovery of a Narrow Resonance in e^+e^- Annihilation*, *Phys. Rev. Lett.* **33**, 1406 (1974).

8) J.-E. Augustin *et al.*, *The Discovery of a Second Narrow Resonance in e^+e^- Annihilation*, *Phys. Rev. Lett.* **33**, 1453 (1974).

9) A. Osterheld, *Measurements of Total Hadronic and Inclusive D-star Cross Sections in Electron Positron Annihilation between 3.87 and 4.5 GeV*, Ph.D. thesis (unpublished), Stanford, SLAC-304 (June 1986).

10) R. Cester *et al.*, *Search for Production of D^{*-} by Pions near Threshold*, *Phys. Rev. Lett.* **40**, 139 (1978).

11) V. L. Fitch *et al.*, *Measurement of D^* Production in Pion-Nucleon Interactions at 200 GeV/c*, *Phys. Rev. Lett.* **46**, 761 (1981).

12) V. L. Fitch *et al.*, *Search for D^* Production in Pion Nucleon Interactions*, *Phys. Rev.* **D33**, 1486 (1986).

13) S. Ono, *Electromagnetic Mass Differences and Decay Rates of Charmed Mesons in the Charmed-Quark Model*, *Phys. Rev. Lett.* **37**, 655 (1976).

14) R. Cahn and B. Kayser, *Angular Distributions and the Physics of Charmed Meson Production at the 4.028-GeV Resonance*, *Phys. Rev.* **D22**, 2752 (1980).

15) M. Coles, *Inclusive D Meson Production with the Mark II Detector at SPEAR*, Ph.D. thesis (unpublished), University of California, Lawrence Berkeley Laboratory, LBL-11513 (September 1980).

16) M. Coles *et al.*, *D Meson Production in e^+e^- Annihilation at ECM between 3.8-GeV and 6.7-GeV*, *Phys. Rev.* **D26**, 2190 (1982).

17) G. Trilling, *The Properties of Charmed Particles*, *Phys. Rep.* **75**, 57 (1981).

18) G. Goldhaber *et al.*, *D and D^* Meson Production Near 4 GeV in e^+e^- Annihilation*, *Phys. Lett.* **69B**, 503 (1977).

19) H. Albrecht *et al.*, *Observation of a New Charmed Meson*, *Phys. Rev. Lett.* **56**, 549 (1986).

20) D. G. Coyne, private communication.

21) H.F.W. Sadrozinski, *Production and Decays of D^* Mesons*, SLAC-PUB-2589, invited talk at 20^{th} Int. Conf. on High-Energy Physics, Madison, Wisconsin, July 17–23, 1980, published in *Madison H.E.Physics* 681(1980).

22) R. L. Thews, *The D^{*0} Width*, *Phys. Rev.* **D17**, 255 (1978).

23) R. L. Thews, *Comparison of Symmetry and Duality Constraints for Radiative Transitions of Mesons*, *Phys. Rev.* **D17**, 3038 (1978).

24) R. L. Thews and A. N. Kamal, *Are D^*-Decays All Right?*, *Phys. Rev.* **D32**, 810 (1985).

25) J. L. Rosner, *P-Wave Mesons with One Heavy Quark*, Enrico Fermi Institute preprint EFI 85/91 (December 1985), to be submitted to *Comments on Nuclear and Particle Physics.*

26) E. Eichten *et al.*, *Charmonium: The Model*, *Phys. Rev.* **D17**, 3090 (1978).

27) E. Eichten *et al.*, *Charmonium: Comparison with Experiment*, *Phys. Rev.* **D21**, 203 (1980).

28) W. Bartel *et al.*, *Inclusive Neutral D^* Production and Limits on F^* Production in e^+e^- Annihilations at PETRA*, *Phys. Lett.* **161B**, 197 (1985).

29) E. D. Bloom *et al.*, *Report on Neutral Particle Detectors and QED*, Berkeley, *Proc., 1974 PEP Summer Study*, PEP-0154 (1975);

E. D. Bloom *et al.*, *Properties of Some Photon Detectors*, Berkeley, *Proc., 1974 PEP Summer Study*, PEP-0155 (1975); and

T. Mast and J. Nelson, *Some Design Considerations for a Large Solid-Angle Charged Plus Neutrals Detector for e^+e^- Storage Rings*, Berkeley, *Proc., 1974 PEP Summer Study*, PEP-0153 (1975).

30) D. W. Dupen, *SLAC: The Story of Stanford's 2-mile Long Accelerator* (unpublished), Stanford, SLAC-062 (May 1966).

31) E. D. Bloom and C. W. Peck, *Physics with the Crystal Ball Detector*, *Ann. Rev. Nucl. Part. Sci.* **33**, 143 (1983).

32) E. B. Hughes *et al.*, *IEEE Trans. Nucl. Sci.* **NS-19**, No. 3:126 (1972).

33) M. Sands, *The Physics of Electron Storage Rings: an Introduction*, University of California, Santa Cruz, SLAC-0121 (1970).

34) R. L. Ford *et al.*, *IEEE Trans. Nucl. Sci.* **NS-24**, 264 (1977).

35) Y. Chan *et al.*, *Design and Performance of a Modularized NaI(Tl) detector (the Crystal Ball Prototype)*, *IEEE Trans. Nucl. Sci.* **NS-25**, No. 1:333 (1978).

36) R. Chestnut *et al.*, *The Crystal Ball Data Acquisition System*, *IEEE Trans. Nucl. Sci.* **NS-26**, No. 4:4395 (1979).

37) M. Oreglia, *A Study of the Reactions $\psi' \to \gamma\gamma\psi$*, Ph.D. thesis (unpublished), Stanford, SLAC-0236 (1980).

38) J. Gaiser, *Charmonium Spectroscopy from Radiative Decays of the J/ψ and ψ'*, Ph.D. thesis (unpublished), Stanford, SLAC-0255 (1982).

39) H. Sadrozinski and J. O'Reilly, *Final Endcap Design*, Crystal Ball Note CB-239 (unpublished), Stanford (April 1978); and

J. Tompkins, *Endcap Spark Chamber Design: a Description and Progress Report*, Crystal Ball Note CB-232 (unpublished), Stanford (July 1977).

40) J. Gaiser *et al.*, *Compact Multiwire Proportional Chambers and Electronics for the Crystal Ball Detector*, *IEEE Trans.Nucl. Sci.* **NS-26**, No. 1:173 (1979).

41) C. Edwards, *A Study of Exclusive Final States in Radiative ψ Decays*, Ph.D. Thesis (unpublished), California Institute of Technology, Pasadena (1985).

42) H. Kolanoski, *The Luminosity Monitor for the Crystal Ball Experiment*, Crystal Ball Note CB-244 (unpublished), Stanford (September 1978).

43) J. D. Bjorken and S. D. Drell, *Relativistic Quantum Mechanics*, McGraw-Hill Book Company, New York (1964), pp. 138–140.

44) F. A. Berends, K. J. F. Gaemers, R. Gastman, *Hard Photon Corrections for Bhabha Scattering*, *Nucl. Phys.* **B68**, 541 (1974).

45) C. Edwards *et al.*, *Hadron Production in e^+e^- Annihilation as a test of QCD*, SLAC-PUB-3030, Stanford, submitted to *Phys. Rev. D*, (1984).

46) G. Godfrey, *Trigger Module*, Crystal Ball Note CB-131 (unpublished), Stanford (June 1978).

47) G. Godfrey, *Integrate and Hold Module*, Crystal Ball Note CB-121 (unpublished), Stanford (November 1976).

48) I. Kirkbride *et al.*, *IEEE Trans. Nucl. Sci.* **NS-25**, 1535 (1979).

49) R. A. Lee, *Radiative Decays of the Psi Prime to All-Photon Final States*, Ph.D. thesis (unpublished), Stanford, SLAC-282 (May 1985).

50) C. M. Lederer, J. M. Hollander, and I. Perlman, *Table of Isotopes*, Sixth Ed., John Wiley and Sons, Inc., New York (1967), pp. 158–161.

51) J. Tompkins, F. Porter, K. Kõnigsman, ed., *Notes from the Crystal Ball Offline Workshop*, Crystal Ball Offline Workshop, SLAC, Stanford, 29 August–2 September 1983.

52) D. J. Prindle, *Measurement of the Resonance Parameters of the Υ and Υ' Mesons*, Ph.D. thesis (unpublished), Carnegie-Mellon University, Pittsburgh (August 1985).

53) J. S. Leffler, *A Search for Primarily Non-Interacting Decay Modes of the Upsilon*, Ph.D. thesis (unpublished), Stanford, SLAC-293 (March 1986).

54) D. Prindle *et al.*, *Measurement of $B_{\mu\mu}$ and Γ_{ee} for the $\Upsilon(1S)$ and $\Upsilon(2S)$ Mesons*, SLAC-PUB-3833, submitted to *Phys. Rev. D*, (1985).

55) R. P. Horisberger, *Search for Charmed F Mesons in e^+e^- Collisions with the Crystal Ball*, Ph.D. thesis (unpublished), Stanford, SLAC-266 (January 1984).

56) C. G. Wohl, *Review of Particle Properties*, Berkeley, *Reviews of Modern Physics* **56** Number 2 Part II, S1 (1984) and *errata* sheet.

57) M. Aguilar-Benitez *et al.*, *Review of Particle Properties*, *Phys. Lett.* **170B**, 1 (1986).

58) R. L. Ford and W. R. Nelson, *The EGS Code System: Computer Programs for the Monte Carlo Simulation of Electromagnetic Cascade Showers (Version 3)*, SLAC-210 (unpublished), Stanford (June 1978).

59) W. R. Nelson, H. Hirayama, and D. W. O. Rogers, *The EGS4 Code System*, SLAC-265 (unpublished), Stanford (December 1985).

60) C. Quigg and J. L. Rosner, *Hadronic Decays of Charmed Mesons*, *Phys. Rev.* **D17**, 239 (1978).

61) J. Tompkins, private communication.

62) D. Coyne *et al.*, *A Proposal for the Use of the Crystal Ball Detector System at PEP*, Stanford Linear Accelerator Center proposal PEP-18 (1977) unpublished.

63) K. Jagannathan *et al.*, *A Rare Decay of the D^{*0} Meson as a Test of the Extension of the Line Shape in a Strongly Decaying System*, *Phys. Rev.* **D32**, 1835 (1985).

64) R. A. Partridge, *A Study of the $\psi''(3770)$ Using the Crystal Ball Detector*, Ph.D. thesis (unpublished), California Institute of Technology (1984).

65) T. Sjostrand, *The LUND Monte Carlo for e^+e^- Jet Physics*, *Comput. Phys. Commun.* **28**, 243 (1982).

66) G. Bonneau and F. Martin, *Hard-Photon Emission in e^+e^- Reactions*, *Nucl. Phys.* **B27**, 381 (1971); and

J. D. Jackson and D. L. Scharre, *Initial-State Radiation and Resolution Corrections and Resonance Parameters in e^+e^- Annihilation*, *Nucl. Instrum. Meth.* **128**, 13 (1975).

67) J. H. Friedman, *SAGE*[*], Stanford Linear Accelerator Center Computation Group Technical Memo 145 (unpublished) (1972).

68) R. B. Chaffee, *A User's Guide for SAGE*, Stanford Linear Accelerator Center Computation Group Technical Memo 195 (unpublished) (1979).

69) B. S. Renger, *A Comparison of GHEISHA and HETC for Phase Space $\pi^+\pi^-\pi^+\pi^-$ MC Generated Events at $\sqrt{s} = 9.46$ GeV*, Crystal Ball Note CB-502 (unpublished), Stanford (December 1985).

70) J. Bagger, *Phase Space Weighting with SAGE*, Crystal Ball Note CB-406 (unpublished) (1979).

71) M. Roos, *Review of Particle Properties*, Berkeley, *Phys. Lett.* **111B**, i (1982).

* The SAGE algorithm is a "general system for Monte Carlo event generation with preferred phase space density distributions" (see the next reference).

72) J. Orear, *Notes on Statistics for Physicists*, University of California Radiation Laboratory Note UCRL-8417 (unpublished) (1958).

73) A. G. Frodesen, O. Skjeggestad, and H. Tøfte, *Probability and Statistics in Particle Physics*, Universitetsforlaget, Bergen, 1979.

74) F. James and M. Roos, *'MINUIT' A System for Function Minimization and Analysis of the Parameter Errors and Correlations*, CERN-DD/75/20, *Comput. Phys. Commun.* **10**, 343(1975).

75) T. A. Gabriel, *The High-Energy Transport Code, HETC*, ORNL/TM-9727, Oak Ridge, in *Proc. of LEP Experimenters' Workshop on Shower Simulation*, Geneva (29–31 January 1985).

T. W. Armstrong, *The HETC Hadronic Cascade Code*, in *Erice 1978, Proc. Computer Techniques in Radiation Transport and Dosimetry* (1978).

76) J. Ranft *et al.*, *FLUKA82*, CERN-TIS-RP/156/CF (1985), presented at Workshop on Shower Simulation for LEP Experiments, Geneva, 29–31 January 1985;

J. Ranft *et al.*, *The Hadron Cascade Code, FLUKA82: Setup and Coupling with EGS4 at SLAC*, SLAC-TN-86-003 (1986) (unpublished);

H. C. Fesefeldt, *The Simulation of Hadronic Showers '—Physics and Applications—'*, III. Physikalisches Institut der RWTH, Aachen, report PITHA-85/02 (1985).

77) A. G. Frodesen *et al.*, *ibid.*, pp 239–241.

78) A. C. Hearn, ed., *REDUCE User's Manual*, version 3.1, The Rand Corporation, Santa Monica, California, Rand publication CP78 (Rev. 4/84), (April 1984), unpublished.

79) H. K. Nguyen *et al.*, *Spin Analysis of Charm Mesons Produced in e^+e^- Annihilation*, *Phys. Rev. Lett.* **39**, 262 (1977).